# A NEW TIME–FREQUENCY ANALYSIS TECHNIQUE FOR NEUROELECTRIC SIGNALS

A THESIS

SUBMITTED TO THE DEPARTMENT OF ELECTRICAL AND

ELECTRONICS ENGINEERING

AND THE INSTITUTE OF ENGINEERING AND SCIENCES

OF BILKENT UNIVERSITY

IN PARTIAL FULFILLMENT OF THE REQUIREMENTS

FOR THE DEGREE OF

MASTER OF SCIENCE

By

D. İlhan Tüfekçi

August 2002

I certify that I have read this thesis and that in my opinion it is fully adequate, in scope and in quality, as a thesis for the degree of Master of Science.

Assoc. Prof. Dr. Orhan Arıkan(Supervisor)

I certify that I have read this thesis and that in my opinion it is fully adequate, in scope and in quality, as a thesis for the degree of Master of Science.

Prof. Dr. A. Enis Çetin

I certify that I have read this thesis and that in my opinion it is fully adequate, in scope and in quality, as a thesis for the degree of Master of Science.

Assoc. Prof. Dr. Nevzat G. Gençer

Approved for the Institute of Engineering and Sciences:

Prof. Dr. Mehmet Baray
Director of Institute of Engineering and Sciences

# ABSTRACT

# A NEW TIME–FREQUENCY ANALYSIS TECHNIQUE FOR NEUROELECTRIC SIGNALS

D. İlhan Tüfekçi
M.S. in Electrical and Electronics Engineering
Supervisor: Assoc. Prof. Dr. Orhan Arıkan
August 2002

In the presence of external stimuli, the functioning brain emits neuroelectrical signals which can be recorded as the Event Related Potential (ERP) signals. To understand the brain cognitive functions, ERP signals have been the subject matter of many applications in the field of cognitive psychophysiology. Due to the non–stationary nature of the ERP signals, commonly used time or frequency analysis techniques fail to capture the time–frequency domain localized nature of the ERP signal components. In this study, the newly developed Time–Frequency Component Analyzer (TFCA) approach is adapted to the ERP signal analysis. The results obtained on the actual ERP signals show that the TFCA does not have a precedent in resolution and extraction of uncontaminated individual ERP signal components. Furthermore, unlike the existing ERP analysis techniques, the TFCA based analysis technique can reliably measures the subject dependent variations in the ERP signals, which

opens up new possibilities in the clinical studies. Thus, TFCA serves as an ideal tool for studying the intricate machinery of the human brain.

*Keywords*: Event Related Potentials, ERP, Oscillatory Brain Signals, EEG, Brain Signal Analysis, Time–Frequency Signal Analysis, Event Related Oscillations, ERO

# ÖZET

## NÖRO–ELEKTRİKSEL SİNYALLER İÇİN YENİ BİR ZAMAN–FREKANS ANALİZ TEKNİĞİ

D. İlhan Tüfekçi
Elektrik ve Elektronik Mühendisliği Bölümü Yüksek Lisans
Tez Yöneticisi: Doç. Dr. Orhan Arıkan
Ağustos 2002

Dış uyarıcıların varlığında, çalışan beyin Olay-İlişkili Potansiyel (OİP) sinyalleri olarak kaydedilebilen nöro-elektriksel sinyaller yayar. Beynin bilişsel fonksiyonlarını anlamak amacıyla, OİP sinyalleri bilişsel psikofizyoloji alanındaki birçok uygulamanın konusu olmuştur. Çokça kullanılan zaman veya frekans analiz teknikleri, OİP sinyallerinin durağan olmayan yapısı nedeniyle, OİP sinyal bileşenlerinin zaman-frekans doğasını ortaya çıkaramamaktadır. Bu çalışmada, yeni geliştirilen Zaman-Frekans Bileşen Çözümleyicisi (TFCA), OİP sinyal analizine uyarlanmıştır. Gerçek OİP sinyallerinden elde edilen sonuçlar, TFCA'ya dayalı OİP analizinin çözünürlük ve kirlenmemiş OİP sinyal bileşenlerinin çıkartılmasında emsalinin bulunmadığını göstermektedir. Ayrıca var olan OİP analiz tekniklerinden farklı olarak TFCA'ya dayalı analiz tekniği, klinik çalışmalarda yeni imkanlar yaratacak olan OİP sinyallerindeki deneğe dayalı değişimleri güvenilir şekilde ölçebilmektedir. Böylece, TFCA

insan beyninin karmakarışık mekanizmasının incelenmesinde, ideal bir araç olarak kullanılabilecektir.

*Anahtar Kelimeler*: Olay-İlişkili Potansiyel, OİP, Salınımlı Beyin Sinyalleri, EEG, Beyin Sinyal Analizi, Zaman-Frekans Sinyal Analizi, Olay İlişkili Salınımlar, ERP, ERO

# ACKNOWLEDGMENTS

I would like to express my deepest gratitude to my supervisor Assoc. Prof. Dr. Orhan Arıkan for his supervision, suggestions and invaluable encouragement throughout the development of this thesis.

I would also like to thank Prof. Dr. Sirel Karakaş, Mrs. Emine D. Çakmak, and all other members of the Cognitive Psychophysiology Research Unit of Hacettepe University for their invaluable help and co–operation.

I would like to thank Prof. Dr. A. Enis Çetin and Assoc. Prof. Dr. Nevzat G. Gençer for reading and commenting on the thesis.

My special thanks go to TÜBİTAK–UEKAE and my colleagues there for their support and encouragement during my graduate study.

Finally I express my special thanks to my family for their constant support, patience and sincere love.

# Contents

# List of Figures

# List of Tables

**To my family...**

# Chapter 1

# INTRODUCTION

The brain emits neuro–electric signals which can be recorded from the scalp of the intact organisms. These neuro-electric signals consist of the spontaneous activity of the brain, the electroencephalgoram (EEG), and its responses to external or internal stimuli, the event related potentials (ERP). The analysis of EEG-ERP signals have been the subject matter of many applications in the field of cognitive psychophysiology.

Brain is a biological, dynamic and non–linear system, where spontaneous electrical activity of the brain changes permanently, even without changes in external conditions [1, 2]. Various properties of the brain system shown in Fig. 1.1 are analyzed using the relationship between the input (i.e., controlled stimulus) and the output (i.e., recorded brain signal) signals of this system to explore the dynamics behind the cognitive brain functions. The recorded brain signals, EEG and ERP, consist of rhythmic activities (oscillations) in several

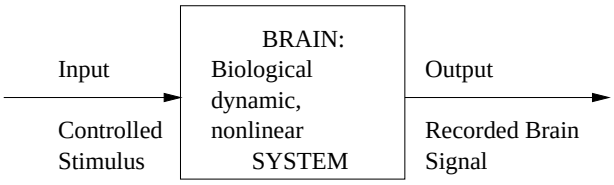


Figure 1.1: Conceptual block diagram of the brain.

frequency ranges [1,3–7]. These oscillations may be triggered by external stimuli or internal hidden sources such as cognitive loading. Current hypothesis states that EEG and ERP are the superposition of these oscillations which are related to different cognitive or behavioral processes of the brain [1, 3–9].

EEG-ERP components may depend on many factors such as the location of the recording electrode, the type of the stimulus, and behavioral or sleep–wake state of the subject.

## 1.1 Previous Work

ERP signals are recorded from various sites of the brain of a test subject for a number of sweeps where in each sweep an external stimulus is applied to the subject. To average out the noise and EEG signal, sweeps are time–domain averaged in most of the studies [1, 4, 5, 7, 9–11]. Depending on the subject, the type of the stimulus and the task that the subject should accomplish the morphology of the ERP signals change [5, 11].

One of the most commonly used ERP analysis technique is based on the identification of the peaks in the averaged ERP signal. This provides a crude temporal description of the ERP signals. The identified ERP peaks have been extensively explored in cognitive psychophysiology: ERP peak at a latency

around 200 millisecond (msec), $N200$, where $N$ denotes the negative amplitude, is related to attention [5,7,12–14]. The amplitude of the positive peak, $P300$, at around 300 msec represents the allocation of attentional resources and is thus closely related to updating of memory for stimulus recognition and working memory [12, 13, 15].

Pattern classification techniques are also used in the temporal analysis of ERP signals, where in unsupervised classifications [16–18], proximity of signal patterns are determined by various statistical distance metrics. On the other hand supervised classifications [19] are based on a learning procedure that uses a set of sample patterns. In a statistical pattern recognition approach developed by Utku and colleagues [20], stepwise multivariate analysis of variance is used to determine the real data points that discriminated between the brain responses to different stimuli. One of the disadvantages of these temporal statistical approaches is that they require a large group of test subjects for optimal efficiency, which is rarely the case in electrophysiological studies of the brain.

The temporal morphology of the time–domain ERP signal does not indicate characteristics of the underlying neural or cognitive functions of the brain, therefore frequency domain analysis techniques are also applied to the ERP signals. It is conjectured that the ERP is a compound signal with oscillatory components that do not overlap in frequency. These oscillatory components are called as event related oscillations (ERO) [1, 3–10]. In order to identify the frequency bands corresponding to each ERO component, amplitude frequency characteristic (AFC) of ERP is computed by using the one–sided Fourier transform. The ERP waveform is filtered with response–adaptive digital filters where the cut-off frequencies of the filters are determined from the

consecutive dips in the AFC [1]. In [5, 7], the effect of digital filtered ERP to the morphology of the ERP peaks, basically N200 and P300, is investigated under various cognitive paradigms.

Spectral properties of non–stationary signals such as ERPs are time-varying, therefore digital filtering is not adequate in analyzing them. Short time Fourier transform (STFT) is used to explore the non–stationary structure of the ERP signal, however the constant window size used in STFT limits the resolution. In [21], STFT with a Hamming window is used to explore the oscillatory components of EEG-ERP signal. Recently wavelet transform is used by neuroscientists [1, 22–27]. Since it uses longer windows at low frequencies and shorter windows at high frequencies, the wavelet transform is better suited to the ERP analysis than the digital filtering. Wavelet coefficients at different scales corresponding to different frequency intervals are used to reconstruct phase–locked ERP signals in time domain. Wavelet transform can be viewed as the decomposition of the signal into dilated, scaled and shifted wavelets, therefore the selected wavelet should have similar characteristics with the ERP signals. For the brain signals quadratic B-spline wavelets are widely used [1,22,26]. However, frequency resolution of the wavelet transform is poorer at lower scales, thus preventing an accurate analysis of components that are close in their frequency supports [28]. Moreover selected mother wavelet may not be the optimum one for all ERP signals under different paradigms and test subjects.

The analysis of the ERP signals by conventional methods reveals that they can be modelled as superposition of some oscillatory and non–stationary signal components, which are well localized in time and frequency. It is well known

that time–frequency signal processing is the natural tool for the analysis of this type of non–stationary signals with localized time–frequency supports. Since time–frequency representations provide the distribution of the signal energy as a joint function of both time and frequency, they present a more complete picture than the aforementioned approaches. In [21], STFT and Wigner distribution (WD) is used in the analysis of the EEG signals and the two are compared in terms of their resolution and level of undesired cross–term contamination. To provide a high resolution description of the time–frequency features of the recorded ERP signals by smoothing out the cross–term interference in the WD, smoothed Wigner distribution has been utilized in [29]. To emphasize the low–energy but high frequency features, a sub-band decomposition of the ERP signal into six levels is performed. Then, the time–frequency analysis on each sub-band signal is obtained. Finally, the obtained time-frequency distributions corresponding to each of the six sub-band signals are fused by using a frequency weighting to provide the overall time-frequency representation. The obtained results provided a picture of the ERP signal in time-frequency domain and has led to deeper understanding with respect to brain dynamics [29].

Recently, by utilizing a novel fractional domain warping concept, a very high resolution time–frequency representation, which is coined as the Time–Frequency Component Analyzer (TFCA), is developed [30]. By conducting Wigner analysis on adaptively chosen warped fractional Fourier domains, the TFCA provides the time–domain representation of the constituent components of the composite signal with unprecedented accuracy, which is of prime importance in the analysis of the ERP signals. The TFCA makes use of fast digital signal processing algorithms, and it provides not only an overall time-frequency representation of the ERP signals [31] but also the time-frequency

representations corresponding to the individual signal components for detailed post-processing. On the individual time-frequency representations; time center, frequency center, time spread, and frequency spread of each component can be estimated, moreover time–frequency support of each component can be computed. This unique feature of the TFCA based analysis provides a robust description of the individual ERP signal components. Another unique feature of the TFCA based time-frequency analysis is that, the identified signal components can be extracted from the recorded ERP signal very accurately.

## 1.2 Outline of the Thesis

In this thesis, recently developed TFCA algorithm is applied to the recorded brain signals. In Chapter 2, stimuli, test subjects and the paradigms used in the recording phase of the ERP signals are explained. Having observed that recorded brain signals are contaminated by the 50 Hz line signal, we developed a method for line signal removal also in Chapter 2.

The most widely used conventional analysis methods; digital filtering and wavelet based methods are discussed in Chapter 3. In the presentation of the results of these methods, averaged target and nontarget ERP signals of a test subject called 'FEBE' recorded by the Prof. Sirel Karakaş's cognitive psychophysiology research team under the Oddball–Easy paradigm are mainly used.

In Chapter 4, ERP signal analysis based on the TFCA technique is discussed. The TFCA provides high resolution time–frequency representation of multi–component signals as shown on a synthetic signal with 3 components.

After the introduction of the TFCA, the results of the TFCA on the real ERP signals recorded by the Cognitive Psychophysiology Research Unit of Hacettepe University are presented in Chapter 5. Then, the thesis is concluded in Chapter 6.

# Chapter 2

# Data Acquisition

Present study analyzes the neuroelectric responses of test subjects, which are recorded in the Cognitive Psychophysiology Research Unit of Hacettepe University (for the laboratory schema refer to Appendix A) from various sites of the 10-20 system (Fig. 2.1) using an electrode cap system. The signal is amplified, analog filtered, A/D converted and recorded by a Nihon Kohden EEG 4418K [32]. The recordings only from the *Fz* site of the 10-20 system is investigated in this study. In the 10–20 international system of electrode placement on the skull of the test subject given in Fig. 2.1 (a), percentages represent proportions of the measured distance basically from the nasion to the inion and between the preauricular points. Fz recording site is located in between F3 and F4 as shown in the dorsal view of the brain in Fig. 2.1 (b).

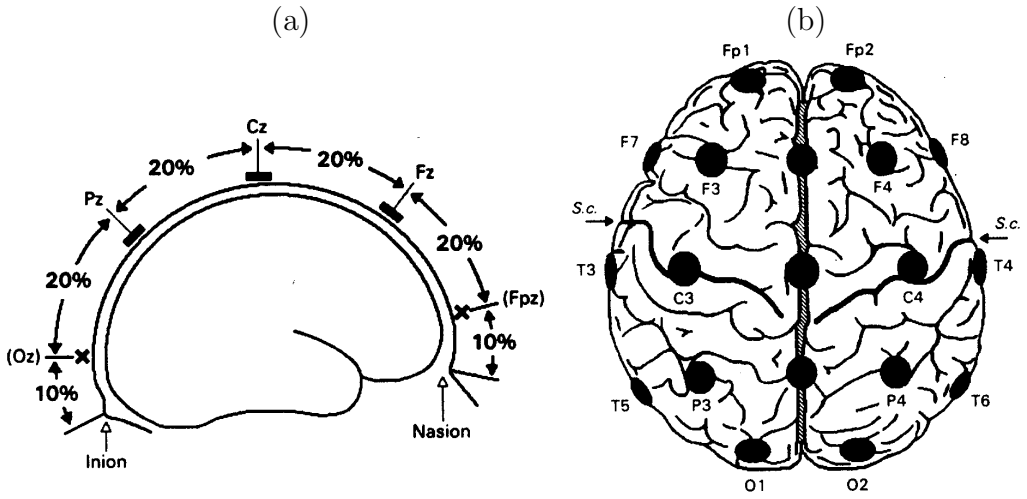


Figure 2.1: (a) 10–20 International System of electrode placement on the skull of the test subject. (b) Dorsal view of the brain. Fz recording site is located in between F3 and F4.

## 2.1 Stimuli

The auditory stimuli had 10 msec rise/fall time, 50 msec duration, and were presented over the headphones at 65 dB SPL (sound pressure level). Two types of auditory stimuli were used: the target stimulus is a short duration (50 msec) sinusoid with a frequency of 2 kHz, and the nontarget stimulus is again a short duration (50 msec) sinusoid with a frequency of either 1 or 1.9 kHz depending on the experimental paradigm. The target stimuli were embedded randomly within a series of nontarget stimuli in all the paradigms. The probability of the target stimuli was 0.2 and that of nontarget stimuli 0.8.

The recording of the EEG-ERP signals is illustrated in Fig. 2.2. A recording for a test subject consists of a number of sweeps with a duration of 2048 msec. The stimulus frequency, task and the number of target/nontarget sweeps used in the standard experimental paradigms of the cognitive psychophysiology are listed in Table 2.1.

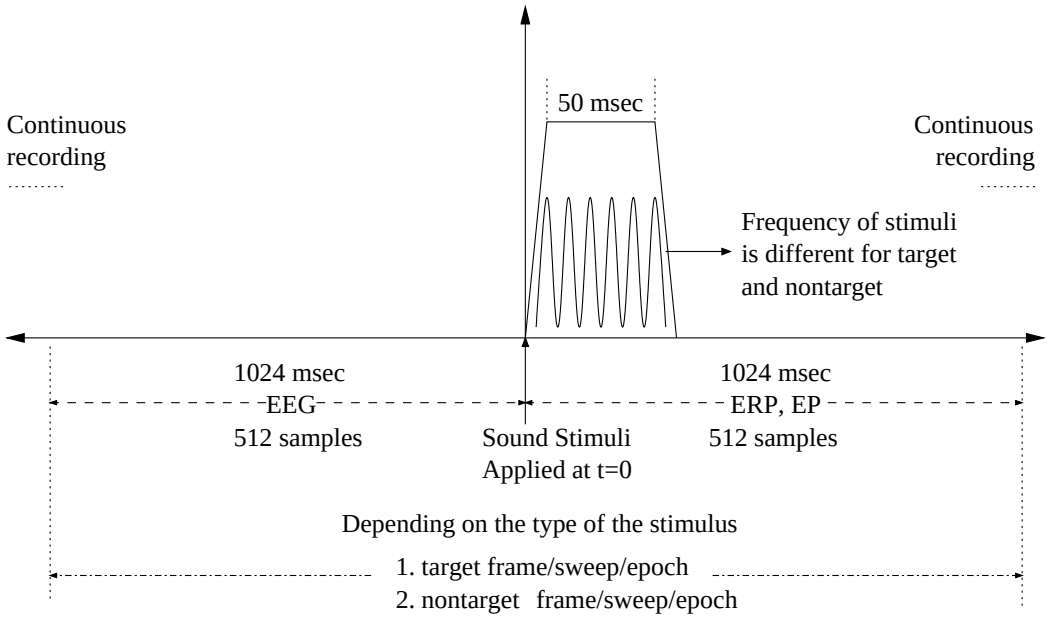


Figure 2.2: Data acquisition scheme of the EEG-ERP signals.

## 2.2 Paradigms

Cognitive psychophysiology has a number of standard experimental paradigms and studies make use of these paradigms to produce different cognitive states. The paradigms differ from each other by the stimulus frequencies and the

| Paradigm | Stimulus Frequency | | Task | Number of Sweeps | | |
|---|---|---|---|---|---|---|
| | Target (kHz) | Nontarget (kHz) | | Target | Nontarget | Total |
| Oddball–Easy | 2 | 1 | Count $N_t$ [a] | 30 | 125 | 155 |
| Oddball–Hard | 2 | 1.9 | Count $N_t$ | 33 | 132 | 165 |
| Mismatch Negativity | 2 | 1 | Unrelated | 42 | 213 | 255 |

[a] $N_t$ = Number of target stimuli

Table 2.1: Stimulus frequency, task and number of target/nontarget sweeps used in the standard experimental paradigms of the cognitive psychophysiology.

task the test subject should carry out as shown in Table 2.1. In this study, Oddball–Easy recordings are mainly analyzed, however Oddball–Hard and mismatch negativity results for the TFCA based analysis will also be presented in Chapter 5.

### 2.2.1 Oddball–Easy (OB-ES)

In this paradigm, the target stimulus frequency is 2 kHz while the nontarget one is 1 kHz. The task of the test subject is to discriminate the target stimuli amongst the nontargets and to report the total number of the target stimuli at the end of the experimental session.

### 2.2.2 Oddball–Hard (OB-HD)

In Oddball–Hard (OB-HD), there is a shorter frequency separation between the target and nontarget stimuli: targets are 2 kHz, however nontargets are 1.9 kHz. Before running the Oddball paradigms where the subject performed recognition tasks, a practice series of stimuli were presented that illustrated the task conditions. The subject was asked to perform the task during the practice session until his/her performance was perfect or nearly so. Subject was encouraged to perform the counting task accurately during the experimental tasks and she was given feedback on the accuracy of her performance at the completion of the session.

Cognitive state of the Oddball paradigms involves the allocation of attention and short–term memory processes and decision for response [5].

### 2.2.3 Mismatch Negativity (MMN)

Mismatch negativity has the same target and nontarget stimuli as the OB-ES. However in this case, the subject is supposed to do an unrelated task that is used to direct attention away from the auditory stimuli. The unrelated task is the digits of ascending or descending order printed on a paper. Every now and then, a digit would be skipped. The subject is requested to read the digits, count the number of the interruptions and at the end of the session report the total number.

MMN requires sensory memory for change detection and involves pre–attentional and pre–conscious processing [5].

## 2.3 Participants

The recorded data at Cognitive Psychophysiological Research Unit of Hacettepe University is obtained from 42 paid subjects (16 males, 26 females) who volunteered and gave written consent to participate in the study. The subjects reported themselves free of neurological or psychiatric problems and reported themselves as not taking medication at the time of testing or not having recently stopped taking such medication. Hearing levels of the test subjects were assessed through computerized audiometric testing before the experimental procedures. Individuals with hearing deficits were not employed in the study.

## 2.4 Recording and Artifact Removal

The neuroelectric responses were recorded from 15 recording sites of the 10-20 system. The present study reports the findings from only the midline Fz recording site. Recordings were made using a commercial electrode cap system (Electro-Cap) of appropriate size. Electrodes were referenced to linked earlobes with forehead as the ground. Bipolar recording were made of electro-ocular (EOG) and electromyographic (EMG) activity for artifact rejection. In the following sections, EEG (pre-stimulus activity) and ERP (post-stimulus response) that have been recorded for target and nontarget stimuli will collectively be called as a frame. The frames were amplified and filtered with a bandpass between 0.16 - 70 Hz (3 dB down, 12 dB /octave). The frames were recorded for a total of 2048 msec, 1024 msec of which served as the prestimulus baseline, the EEG, and the remaining post-stimulus signal is the ERP. The frames were digitized with a sampling rate of 500 Hz. EEG/ERP data acquisition, analysis, and storage were achieved by a commercial system (Brain Data 2.92).

The recorded frames that contained artifacts were rejected first by an on-line and later an off-line technique. The on-line rejection was accomplished by the EEG/ERP data acquisition software that rejected all frames where the recorded frame exceeded $\pm\ 50\mu V$. This occurred for the frames that contained muscle activity. In the off-line procedure, single sweep EOG recordings were visually studied and trials with eye-movement or blink artifacts were rejected. Hence the number of the target/nontarget sweeps used in the analysis of the ERP signals may be lower than those listed in Table 2.1.

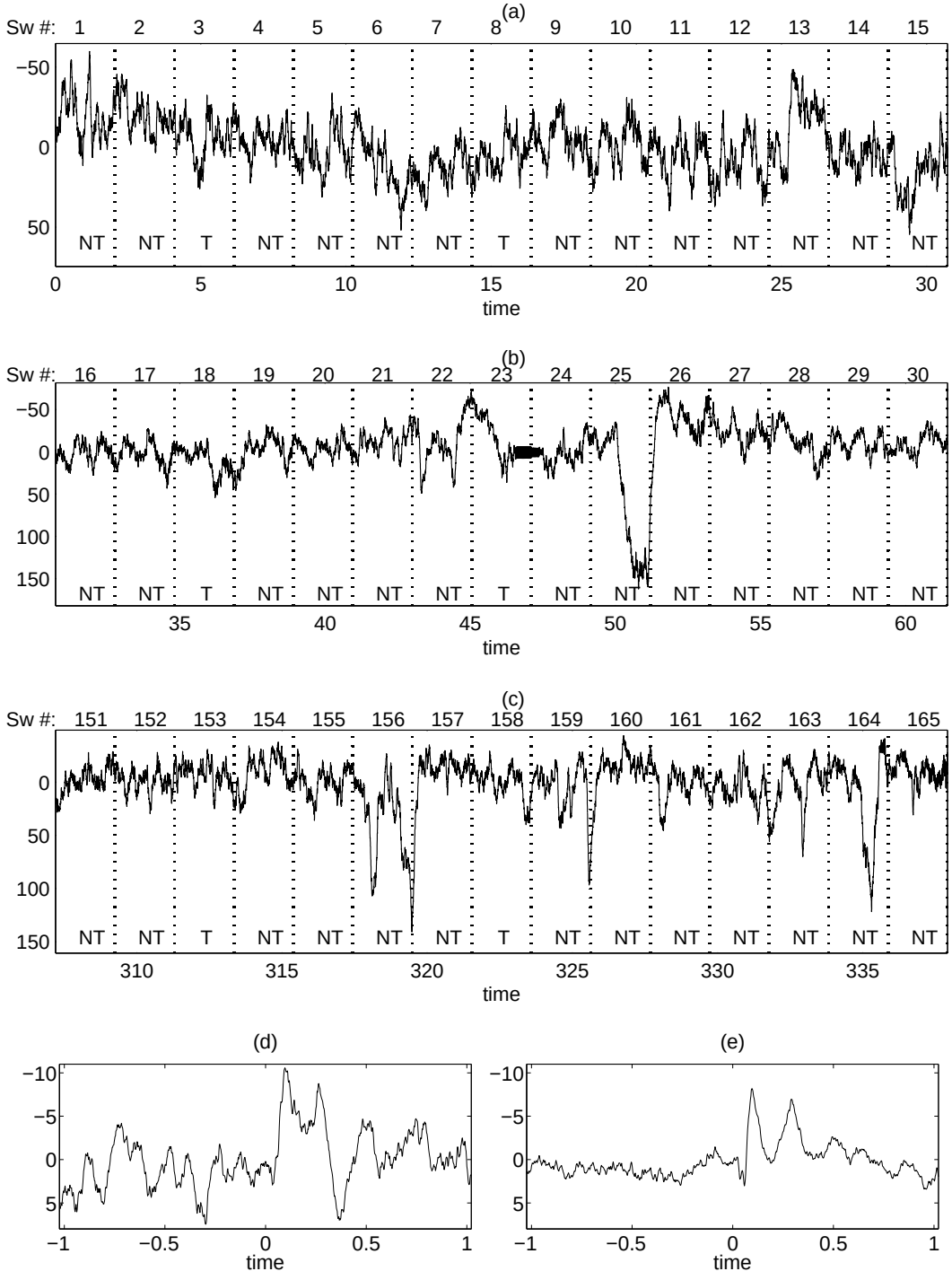


Figure 2.3: Illustration of the EEG/ERP recording. (a) contains the first 15 sweeps, (b) the sweeps numbered 16-30, and (c) the last 15 sweeps. Some sweeps containing artifacts such as sweeps numbered 25, 156, and 164 are not considered. The averaged target and nontarget artifact–free sweeps are shown in (d) and (e) respectively.

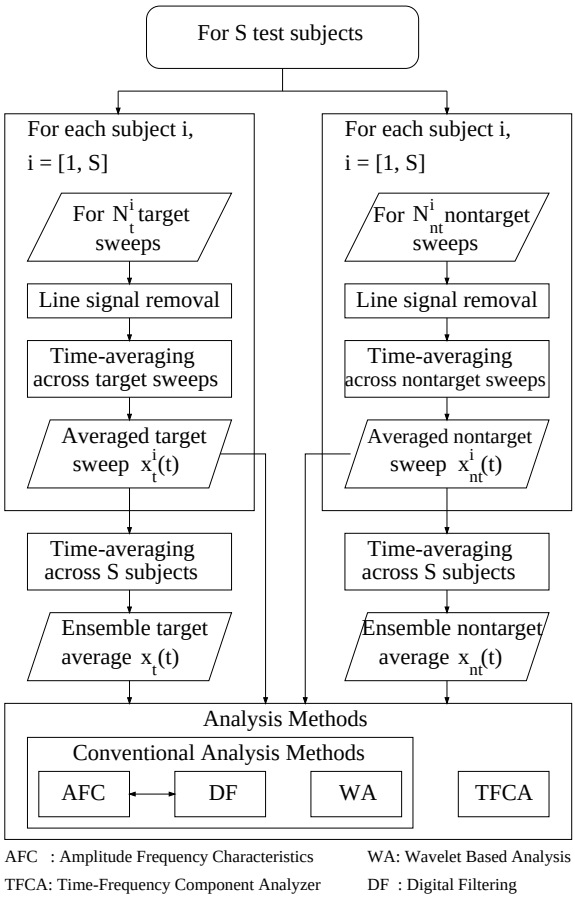


Figure 2.4: Analysis schemes for the target/nontarget ERP sweeps.

The recorded continuous ERP signal is divided into target and nontarget sweeps depending on the type of the stimuli applied during the sweep. Only the first 30 and the last 15 sweeps of the ERP signal recorded under the OB–HD paradigm are shown in Fig. 2.3 (a), (b) and (c) where the sweep numbers are given at the top of the figures. OB–HD paradigm contains 165 sweeps, therefore the total recording time of the ERP signal is $165 * 2.048 \cong 337$ seconds. *Note that to comply with the previous literature on the ERP analysis, the y–axis is plotted downwards.* Once the sweeps containing the artifacts such as the ones numbered 25, 156, and 164 are removed from the signal, the target average shown in Fig. 2.3 (d) is obtained by averaging the artifact–free target

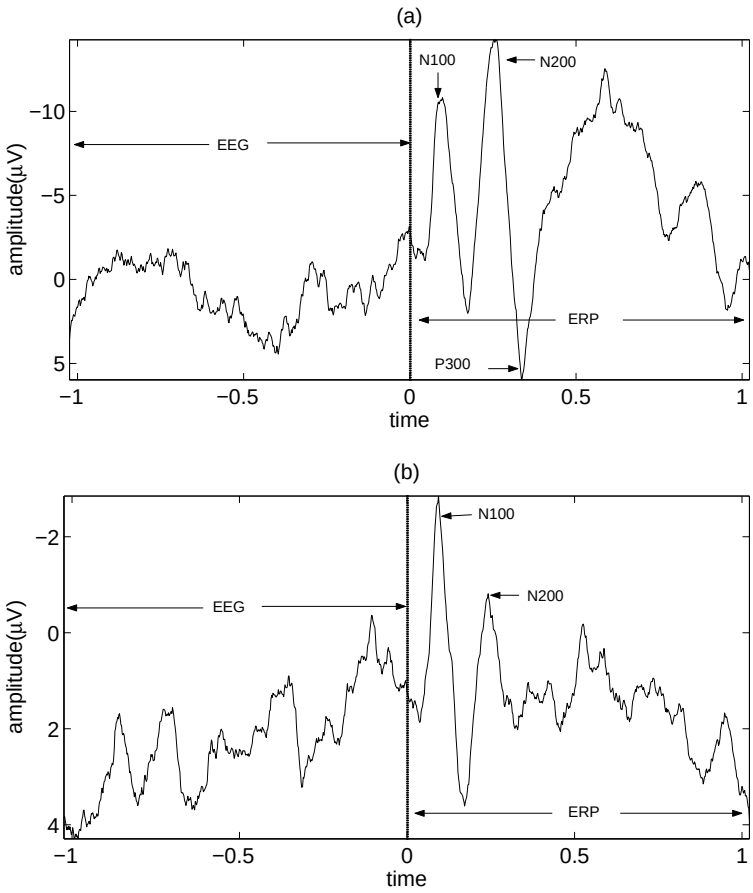


Figure 2.5: Averaged target (a) and nontarget (b) response for the test subject 'FEBE'.

sweeps and the nontarget average in (e) by averaging the artifact–free nontarget sweeps.

As shown in Fig. 2.4, the recorded target or nontarget sweeps can be analyzed in different ways. The artifact–free target or nontarget sweeps belonging only to a test subject can be averaged, or the ensemble average of all the test subjects can be used in the studies.

In this study, the target and nontarget average of a test subject named 'FEBE' under Oddball–Easy paradigm will be mainly studied. Examples of

other paradigms belonging to individual subjects or ensemble averages will also be given. For 'FEBE', there were 22 artifact–free frames for target stimuli; accordingly 22 artifact–free frames for nontarget stimuli were selected from the middle third portion of the nontarget sequence. The chosen artifact–free frames of the test subject were averaged to obtain an individual target/nontarget average frame which is shown in Fig. 2.5 (a) for the target frame and (b) for the nontarget one. The average target frame consists of a negative peak within the 70-120 msec latency window called the N100; a second negative peak within the 150-280 msec window, called the N200; and a positive peak at the 260-400 msec window, called the P300 as shown with arrows in Fig. 2.5 (a). The average nontarget frame given in Fig. 2.5 (b), has a negative peak within the 70-120 msec latency window, the N100. The activity in the range of 150-280 msec window (N200) is insignificant while that at the 260-400 msec window (P300) is nonexistent.

### 2.4.1 Line Signal Removal

Although the data acquisition system has a notch filter used for removing 50-Hz power-line signal, it is not activated during recording, because its activation may result in removing desired components around 50 Hz, i.e., gamma response (Refer to Table 3.1). This 50 Hz power-line contamination signal is removed from each sweep by estimating its phase and amplitude from the EEG (pre-stimulus response) of each sweep before any averaging is done. The assumption is that the phase and the amplitude of the line signal will not change significantly on the ERP phase taking place after the application of the stimulus. The Cognitive Psychophysiological Research Unit of Hacettepe University is

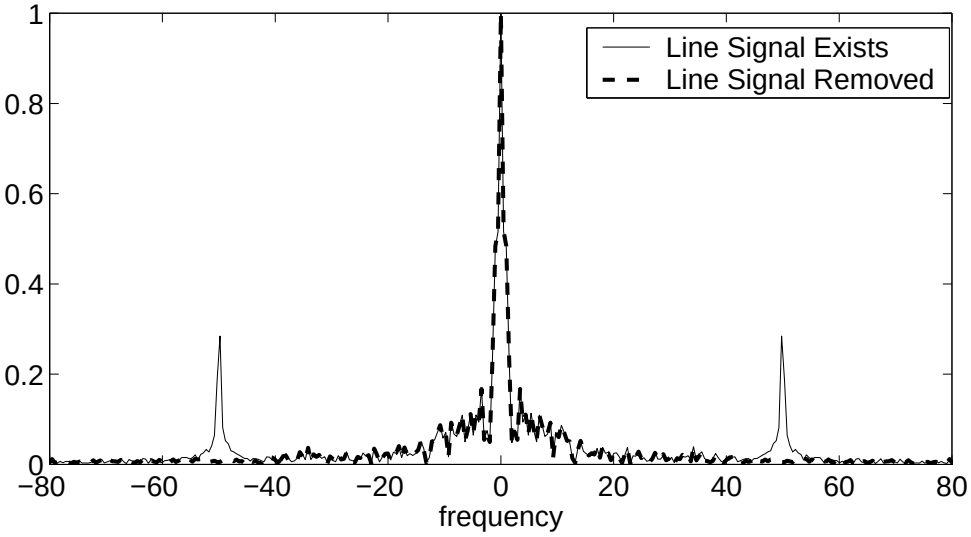


Figure 2.6: Frequency response of the frame before (solid line) and after (dashed line) the removal of the line signal contamination.

furnished with power–line regulators providing stable line frequency over time.

The estimate of the phase of the line signal, $\hat{\phi}$, is obtained from

$$\hat{\phi} = \arg\max_{\phi} \left| \sum_{n=0}^{N-1} w[n] \times EEG[n] \times l[n] \right| \quad , \tag{2.1}$$

where $l[n] = \cos(2\pi f_l n/f_s + \phi)$, EEG[n] is the pre-stimulus response containing $N = 512$ samples and $w[n]$ is an appropriately chosen window function. In this equation $f_l = 50$ Hz is the line and $f_s = 500$ Hz is the sampling frequency. Defining $\hat{l}[n] = \cos(2\pi f_l n/f_s + \hat{\phi})$; the estimate of the amplitude, $\hat{\alpha}$, is found by minimizing $J(\alpha, \hat{\phi})$

$$J(\alpha, \hat{\phi}) = \sum_{n=0}^{N-1} w[n] \times (EEG[n] - \ \alpha\ \hat{l}[n])^2 \quad , \tag{2.2}$$

with respect to $\alpha$. Estimated amplitude is found from

$$\left.\frac{\partial J}{\partial \alpha}\right|_{\hat{\alpha}} = 0 \ \Rightarrow \ \hat{\alpha} = \frac{\sum_{n=0}^{N-1} w[n] \times EEG[n] \times \hat{l}[n]}{\sum_{n=0}^{N-1} w[n] \times \hat{l}[n]^2} \quad . \tag{2.3}$$

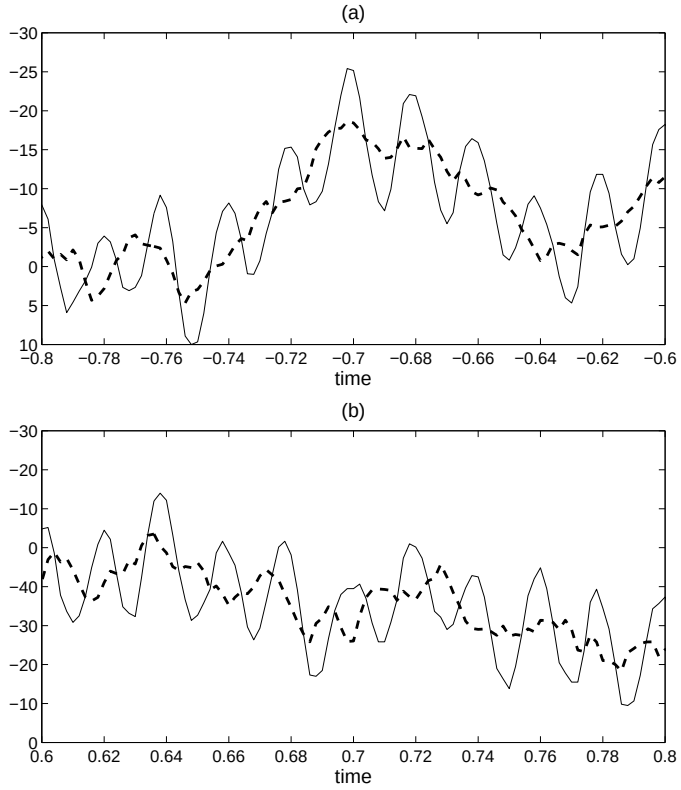


Figure 2.7: Pre–stimulus (a) and post–stimulus (b) time signals before (solid line) and after (dashed line) the removal of the line signal contamination.

Among a number of different windows, $w[n]$, such as rectangular, exponential and raised cosine, rectangular window has been used based on the obtained results. The resultant estimated line signal is re–constructed as

$$l_e[n] = \hat{\alpha} \ \cos\left(2\pi f_l n / f_s + \hat{\phi}\right) \ , \tag{2.4}$$

and subtracted from the whole sweep (frame). Frequency responses of the original and line signal removed brain responses of the selected sweep are shown in Fig. 2.6. The 50 Hz oscillatory activity obvious in the original ERP signal shown in Fig. 2.7 (a) and (b) as solid lines, does not exist in the line signal removed ERP signal (dashed lines) for not only the pre–stimulus response (a) but also the post-stimulus one (b).

# Chapter 3

# Conventional Analysis Techniques

In the analysis of EEG-ERP signals, digital filtering and wavelet based techniques are widely used by neuroscientists [1, 7, 8, 10, 13, 22, 33–36]. These techniques are explained in this chapter due to their wide usage in cognitive psychophysiology. Only the 'FEBE' results of these techniques will be presented.

## 3.1 The AFC and Digital Filtering Based Analysis

The amplitude frequency characteristics (AFC)[1] of the system is computed by the application of the one-sided Fourier transform to the derivative of the

[1] $G(f)$ is also called as transient frequency response characteristics (TRFC) since it is obtained from the transient response of the system [1].

| Name | Delta | Theta | Alpha | Beta | Gamma |
|---|---|---|---|---|---|
| Frequency(Hz) | [0.5-4] | [4-8] | [8-13] | [16-30] | [30-60] |

Table 3.1: General frequency supports of the Event Related Oscillations (EROs) [1].

transient response, c(t), the average target or nontarget ERP, as

$$|G(f)| = \left| \int_0^\infty \frac{d\{c(t)\}}{dt} e^{-j2\pi ft}\, dt \right| \quad . \tag{3.1}$$

The numerical evaluation of the AFC was accomplished by using the fast Fourier transform (FFT) algorithm. The oscillatory behavior of the AFC is smoothed out by taking its running average with a Hanning window. Denoting the samples of the AFC as $G[n]$, the smoothing is achieved by

$$\begin{aligned} G[0] &= 0.5G[0] + 0.5G[1] \quad , \\ G[n] &= 0.25G[n-1] + 0.5G[n] + 0.25G[n+1] \quad n = 1, 2, \ldots, N-1 \quad , \\ G[N] &= 0.5G[N-1] + 0.5G[N] \quad , \end{aligned} \tag{3.2}$$

where N is the number of samples in the AFC and is 512. The smoothing is done over the logarithmic frequency scale. AFC of the target and nontarget frames are shown in Fig. 3.1 (a) and (b) for the frequency range [1-100] Hz, respectively. The AFCs are normalized so that the amplitude at 1 Hz is equal to 0 dB. Note that the frequency scale is logarithmic.

In order to separate the signal components in the recorded frame, digital filtering (DF) techniques have been commonly used. The idea is that the individual signal components occupy different frequency bands, which are separated from each other in identifiable dips in the AFC (spectrum) of the recorded frame [1, 22]. Therefore, four or five individual frequency bands are

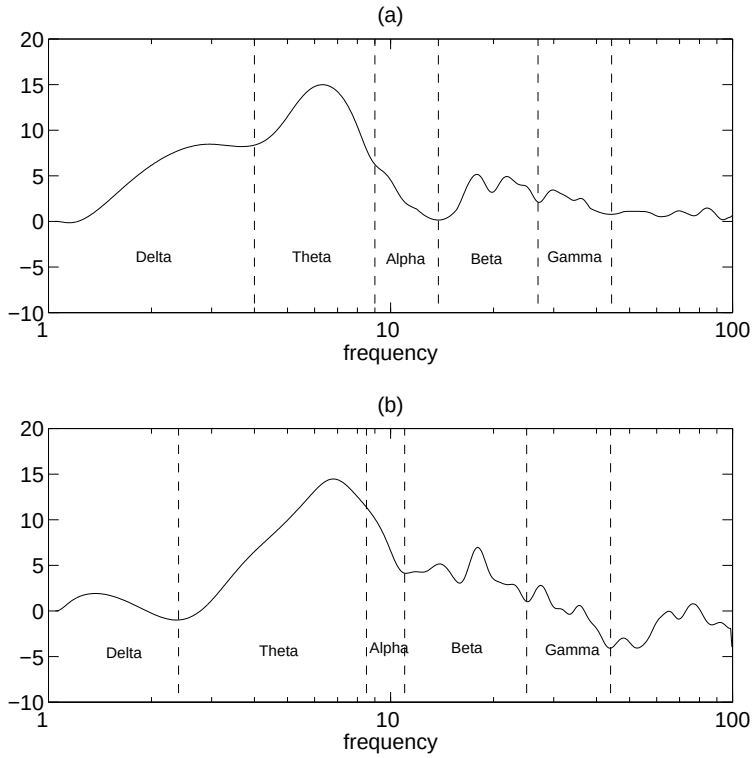


Figure 3.1: AFCs of the average target (a) and nontarget (b) frames of 'FEBE' with frequency ranges of EROs overlaid.

identified corresponding to the spectral dips of the consecutive dominant peaks of the AFC, as given in Table 3.1. Once, the spectral supports of the desired components are determined, finite impulse response (FIR) filters are accordingly designed to perform the required DF operation. For the 'FEBE' case, the frequency bands determined from the AFCs given in Fig. 3.1 are listed in Table 3.2. Filtered target frames (EROs) shown in Fig. 3.2 (a)-(e) demonstrated

| Oscillatory Component | Delta | Theta | Alpha | Beta | Gamma |
|---|---|---|---|---|---|
| Target Frequency Ranges (Hz) | [0.1-3.9] | [4-9] | [9.1-13] | [13.1-27] | [27.1-44] |
| Nontarget Frequency Ranges (Hz) | [0.1-2.4] | [2.5-8.5] | [8.6-11] | [11.1-25] | [25.1-44] |

Table 3.2: Frequency supports of the EROs of the target and nontarget frames of 'FEBE' obtained from the AFCs shown in Fig. 3.1.

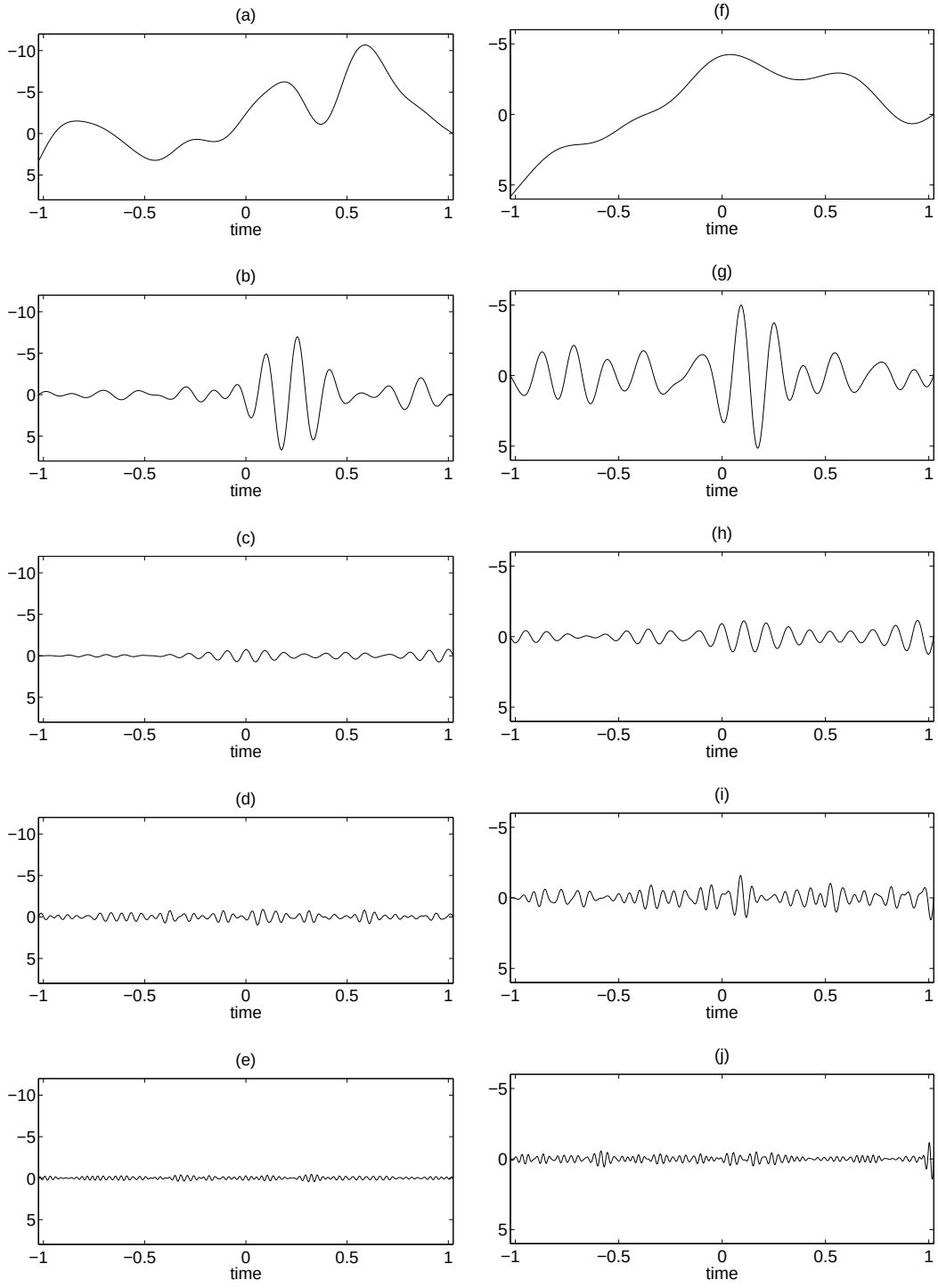


Figure 3.2: Delta, Theta, Alpha, Beta and Gamma signals (EROs) are given in (a)-(e) for the target frame and in (f)-(j) for the nontarget frame, respectively.

amplitude enhancement upon stimulation and ongoing pre–stimulus activity. In a similar manner, filtered nontarget frames are shown in Fig. 3.2 (f)-(j).

## 3.2 Wavelet Decomposition Based Analysis

Spectral properties of non-stationary signals such as recorded ERP frames are time–varying, therefore digital filtering alone is not adequate in analyzing them. Wavelet transform has recently been used by neuro-scientists, since it has better time-scale localization with respect to digital filtering for the purpose of either the extraction of individual ERP components [22–25, 37] or noise removal [38]. Wavelet transformation can be viewed as a signal decomposition into a set of basis functions, called wavelets, that are obtained from a single prototype wavelet by time shifts, dilation and scaling. Wavelet analysis can also be viewed as the correlation of the original signal with the dilated-scaled wavelets, therefore scaling function should have similar characteristics with the analyzed signal. For the ERP signals, quadratic B–spline wavelets are widely used [22, 26,38]. Quadratic B–spline wavelets form a base in $\mathcal{L}^2$, they are not orthogonal, but symmetric, smooth and have compact support.

The wavelet decomposition and reconstruction equations for a signal $x[n]$ are given as

$$C(j,k) = \sum_{n \in Z} x[n]\ \psi^d_{j,k}[n] \tag{3.3}$$

$$\tilde{x}[n] = \sum_{j \in Z} \sum_{k \in Z} C(j,k) \psi^r_{j,k}[n] \quad , \tag{3.4}$$

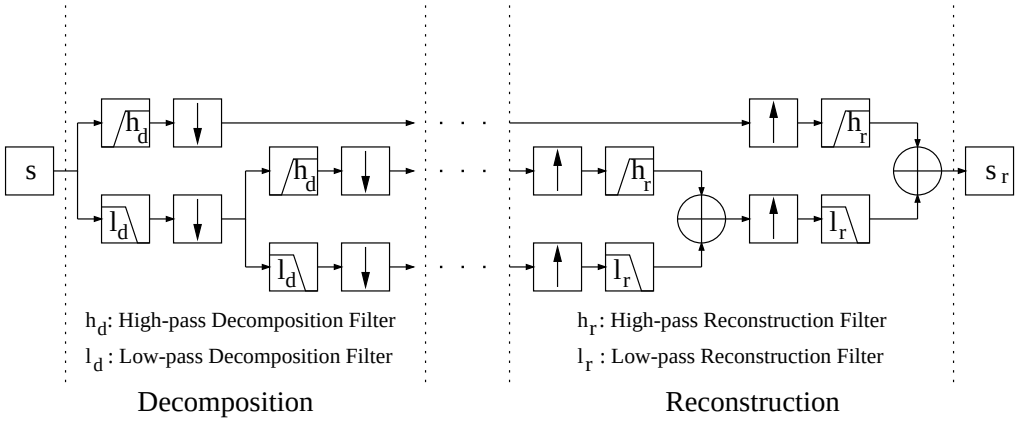


Figure 3.3: Wavelet decomposition (analysis) and reconstruction (synthesis) structure.

where $C(j,k)$s are the wavelet coefficients and $\tilde{x}[n]$ is the reconstructed signal. In Equations 3.3 and 3.4, $\psi^d_{j,k}$ is the decomposition and $\psi^r_{j,k}$ is the reconstruction wavelet satisfying the biorthogonality condition:

$$\sum_n \psi^d_{j,k}[n]\ \psi^r_{j',k'}[n] = \begin{cases} 1 & \text{if } j = j' \text{ or } k = k' \\ 0 & \text{otherwise} \end{cases} \quad . \tag{3.5}$$

$\psi^{r,d}_{j,k}$ is the dyadic scaled, dilated and shifted version of the mother wavelet $\psi^{r,d}$:

$$\psi^{r,d}_{j,k}[n] = 2^{-j/2}\psi^{r,d}(2^{-j}n - k), \quad j,\ k \in N,\ \ n \in Z \quad . \tag{3.6}$$

Wavelet decomposition and reconstruction structure is shown in Fig. 3.3.

The frequency response of the high–pass and low–pass filters used in the decomposition are given in Fig. 3.4 (a) and in the reconstruction in (b). Decomposition scaling and wavelet functions can be observed in Fig. 3.5 (a) and (b), respectively, and those for the reconstruction in (c) and (d). The low–pass and high–pass filter coefficients used in the decomposition and reconstruction of the EEG-ERP signals are shown in Table 3.3.

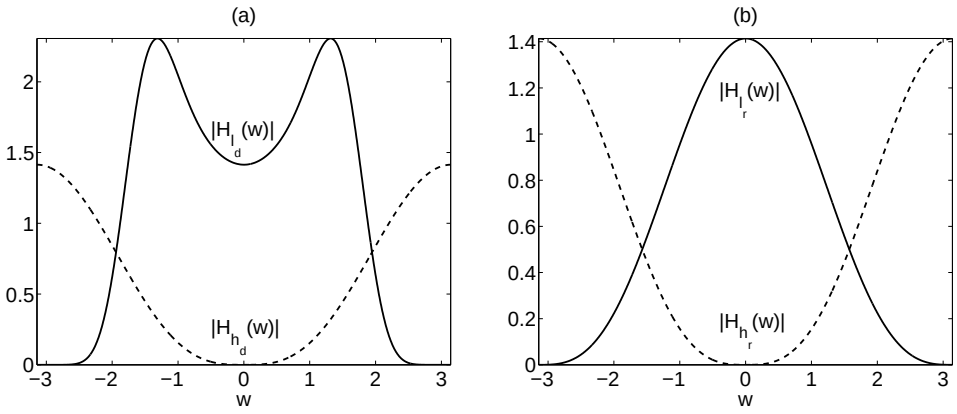


Figure 3.4: Frequency responses of the high–pass and low-pass filters used in decomposition $(H_{h_d}, H_{l_d})$ (a) and reconstruction $(H_{h_r}, H_{l_r})$ (b).

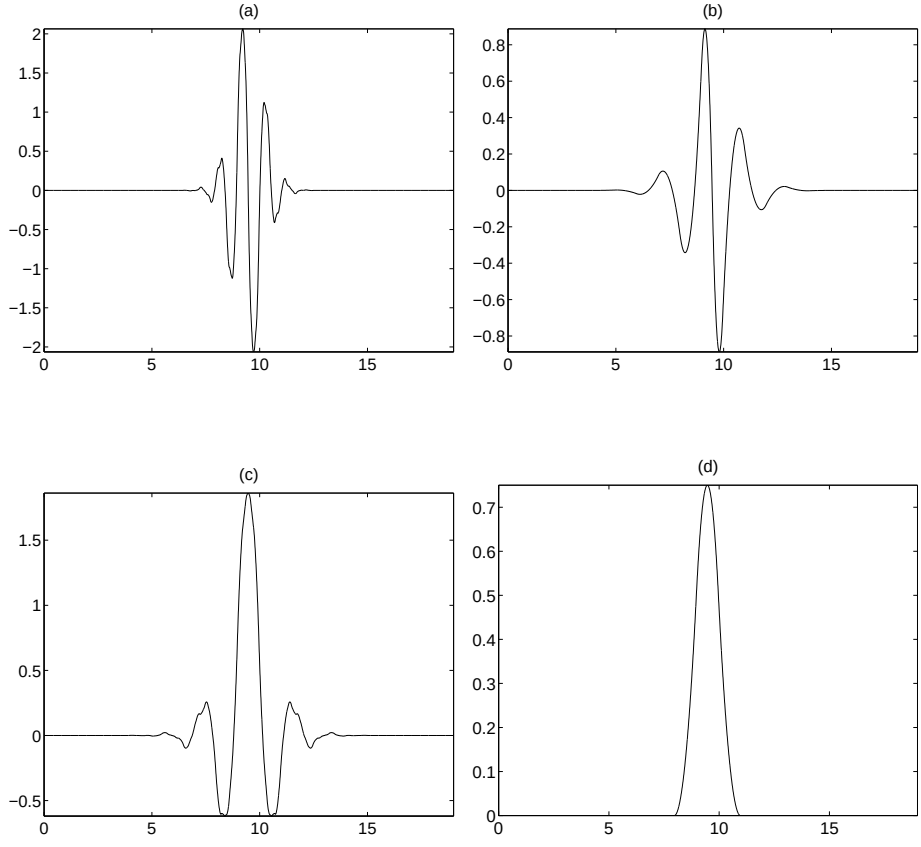


Figure 3.5: Scaling (a) and wavelet (b) functions used in the decomposition and those (c) and (d) used in the reconstruction.

| | $l_d$ | $h_d$ | $l_r$ | $h_r$ |
|---|---|---|---|---|
| -10 | -0.0007 | 0 | 0 | -0.0007 |
| -9 | 0.0020 | 0 | 0 | -0.0020 |
| -8 | 0.0051 | 0 | 0 | 0.0051 |
| -7 | -0.0206 | 0 | 0 | 0.0206 |
| -6 | -0.0141 | 0 | 0 | -0.0141 |
| -5 | 0.0991 | 0 | 0 | -0.0991 |
| -4 | 0.0123 | 0 | 0 | 0.0123 |
| -3 | -0.3202 | 0 | 0 | 0.3202 |
| -2 | 0.0021 | -0.1768 | 0.1768 | 0.0021 |
| -1 | 0.9421 | 0.5303 | 0.5303 | -0.9421 |
| 0 | 0.9421 | -0.5303 | 0.5303 | 0.9421 |
| 1 | 0.0021 | 0.1768 | 0.1768 | -0.0021 |
| 2 | -0.3202 | 0 | 0 | -0.3202 |
| 3 | 0.0123 | 0 | 0 | -0.0123 |
| 4 | 0.0991 | 0 | 0 | 0.0991 |
| 5 | -0.0141 | 0 | 0 | 0.0141 |
| 6 | -0.0206 | 0 | 0 | -0.0206 |
| 7 | 0.0051 | 0 | 0 | -0.0051 |
| 8 | 0.0020 | 0 | 0 | 0.0020 |
| 9 | -0.0007 | 0 | 0 | 0.0007 |

Table 3.3: Coefficients of the low–pass and high–pass decomposition $(l_d, h_d)$ and reconstruction $(l_r, h_r)$ filters.

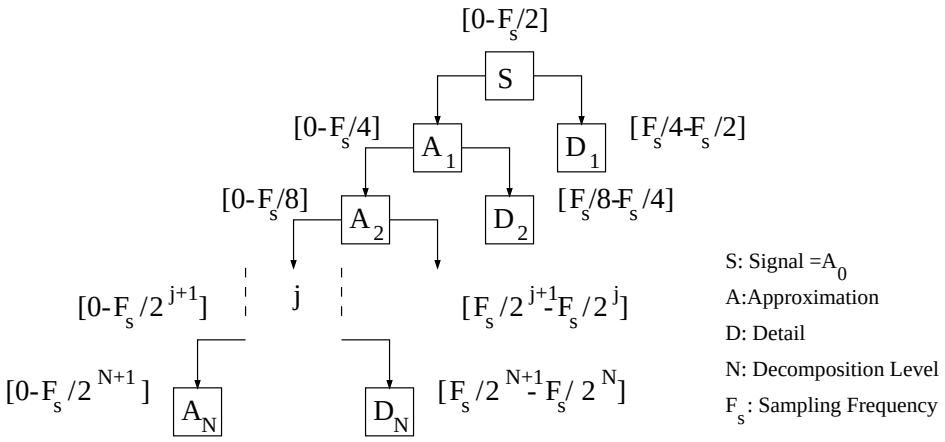


Figure 3.6: Successive decomposition of a signal into approximations and details.

| Name | Delta | Theta | Alpha | Beta | Gamma |
|---|---|---|---|---|---|
| Details | $D_9 + D_8 + D_7$ | $D_6$ | $D_5$ | $D_4$ | $D_3$ |
| Frequency(Hz) | [0.49-3.91] | [3.91-7.81] | [7.81-15.62] | [15.62-31.25] | [31.25-62.5] |

Table 3.4: Approximate frequency supports of the EROs obtained from the quadratic B–spline wavelet decomposition down to the $9^{th}$ level.

A signal $x[n] \equiv A_0[n]$, can be successively decomposed into approximations $A_j$ and details $D_j$ as shown in Fig. 3.6 where j is the level of the decomposition [39]:

$$A_{j-1}[n] = A_j[n] + D_j[n] \quad . \tag{3.7}$$

Approximations give a low frequency representation of the signal and details a high frequency representation:

$$A_j[n] = \sum_k A_{j-1}[k]\phi_{j,k}[n] \tag{3.8}$$

$$D_j[n] = \sum_k D_{j-1}[k]\psi_{j,k}[n] \quad . \tag{3.9}$$

The frequency content of the original signal occupies the band [0-$F_s/2$] where $F_s$ ($F_s$ = 500 Hz for the recorded frames) is the sampling frequency. The frequency band of the approximation at level j is [0-$F_s/2^{j+1}$], and that of the detail at level j is [$F_s/2^{j+1}$-$F_s/2^j$] as shown in Fig. 3.6. Therefore the details having the frequency bands listed in Table 3.4 are identified as the oscillatory components (EROs) of the ERP signals where wavelet decomposition down to the $9^{th}$ level is done.

The results of the wavelet analysis for the target frame are shown in Fig. 3.7 (a)-(d) where the EROs; delta, theta, alpha and beta signals (gamma not shown here) are plotted respectively. Similarly, reconstructed EROs for the nontarget frame are given in Fig. 3.7 (e)-(h).

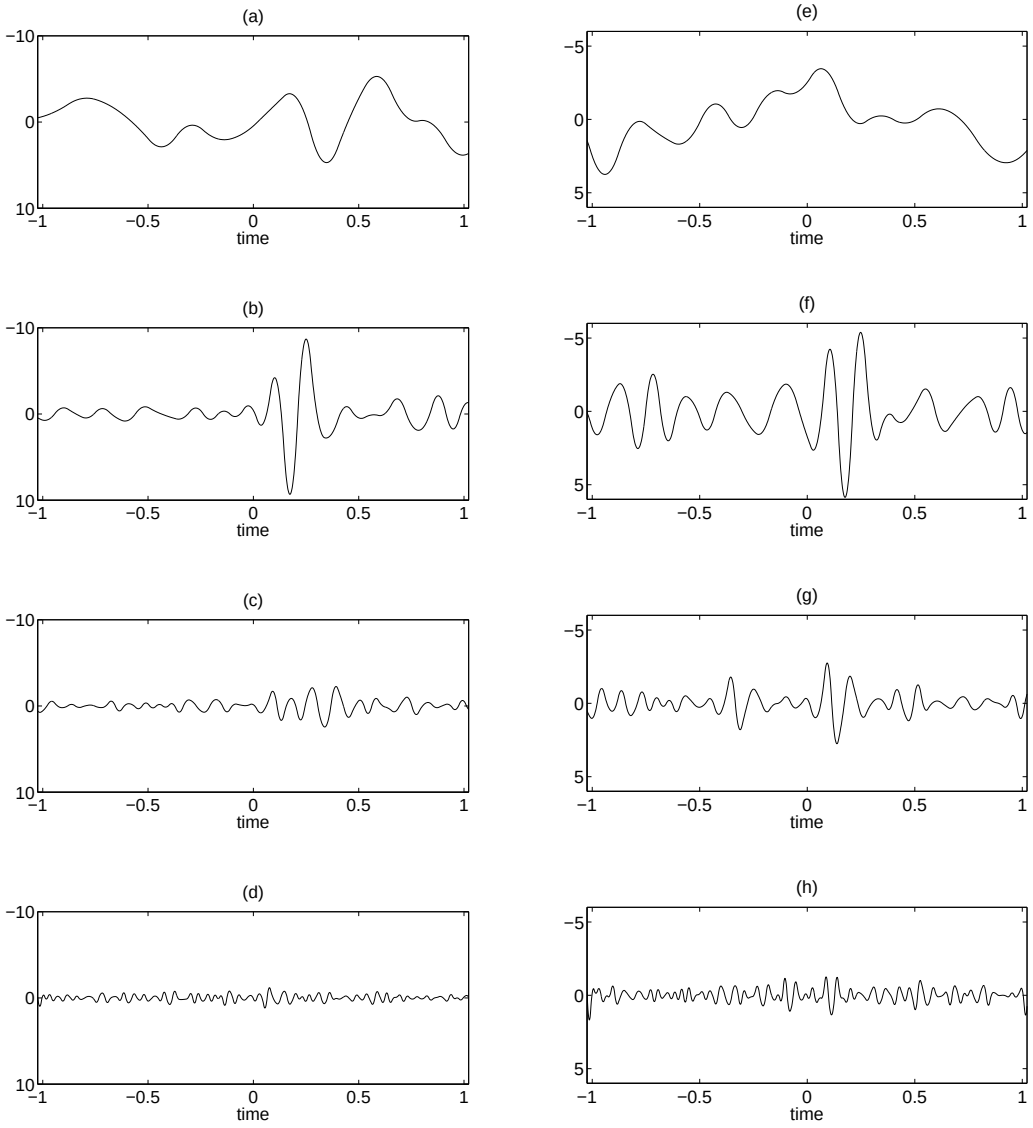


Figure 3.7: Quadratic B-spline wavelet based ERP signal analysis results for 'FEBE' target and nontarget frames. Delta, theta, alpha and beta signals in the approximate frequency bands given in Table 3.4 are reconstructed for both the target ( shown in (a), (b), (c), (d) ) and nontarget frames ( shown in (e), (f), (g), (h) ), respectively.

As it is detailed in Chapter 5, the wavelet based analysis does not provide an accurate time–frequency domain description of individual ERP signal components, and cannot extract the individual ERP signal components from the recorded ERP signals.

More powerful wavelet based analysis techniques such as nonuniform subband decomposition [40] can be used in the analysis of the ERP signals. Different decimation factors are used in nonuniform subband decomposition where the frequency ranges of the signal components are to be pre–determined. AFC can be used to identify the frequency supports of the individual signal components, however as shown in Chapter 5 TFCA provides the most accurate time–frequency support identification of the individual components of the ERP signals.

# Chapter 4

# ERP Analysis Based on the TFCA

Time–frequency signal processing is the natural tool for the analysis of non–stationary signals such as ERP signals. Since time–frequency representations provide the distribution of the signal energy as a joint function of both time and frequency, they present a more complete picture of the signal than the aforementioned approaches, namely digital filtering and wavelet based analysis techniques.

In this chapter, a recent algorithm developed by Özdemir and Arıkan [30], which makes use of a novel fractional domain warping concept [41] and obtains a very high resolution time–frequency representation, is described. This new algorithm, which is coined as *Time–Frequency Component Analyzer (TFCA)* [30], provides not only the time–domain representation of the components of the composite signal but also their individual time–frequency distributions with

unprecedented accuracy, which is of prime importance in the analysis of the ERP signals.

## 4.1 Overview of Time–Frequency Signal Analysis

Among the time–frequency representations developed so far, the Wigner distribution (WD) [42–45] is widely used because of its nice theoretical properties such as preservation of the marginals and high auto–term concentration especially for signals with linear time–frequency supports. The WD $W_x(t, f)$ of a signal $x(t)$ is defined by the following integral [1] [45]

$$W_x(t,f) \triangleq \int x(t+t'/2)x^*(t-t'/2)e^{-\jmath 2\pi f t'}\,\mathrm{d}t' \quad , \tag{4.1}$$

where $(t, f)$ denotes the time and frequency coordinate.

Because of the bilinearity of the WD evident from the definition given in Eq. 4.1, the interpretability of the WD is greatly diminished by the existence of cross–Wigner terms in the WD of multi–component signals and/or signals with non–linear time–frequency supports [45, 46]. Cross–terms limit the use of the WD on some important applications including the analysis of the ERP signals. In the WD of a multi–component signal, cross–terms might partially or completely overlap with the auto–components making the detection of the time–frequency supports of the auto–components very difficult or even impossible.

[1] All the integrals are from $-\infty$ to $\infty$ unless otherwise stated.

The Wigner distribution of a multi–component signal $x(t) = \sum_{i=1}^{M} s_i(t)$ with M components $s_i(t), 1 \leq i \leq M$ can be expressed as:

$$\begin{aligned} W_x(t,f) &= \int \sum_i s_i(t+t'/2) \sum_k s_k^*(t-t'/2) e^{-\jmath 2\pi f t'} \, \mathrm{d}t' \\ &= \sum_i \int s_i(t+t'/2) s_i^*(t-t'/2) e^{-\jmath 2\pi f t'} \, \mathrm{d}t' \\ &\quad + \sum_{i,k \;\; i \neq k} \int s_i(t+t'/2) s_k^*(t-t'/2) e^{-\jmath 2\pi f t'} \, \mathrm{d}t' \quad , \end{aligned} \tag{4.2}$$

which can be simplified into

$$W_x(t,f) = \sum_i W_{s_i}(t,f) + 2 \sum_{i,k \;\; i<k} \mathcal{R}e\{W_{s_i s_k}(t,f)\} \quad , \tag{4.3}$$

where $W_{s_i}(t,f),\ 1 \leq i \leq M$ are the auto–components of the WD and $W_{s_i s_k}(t,f),\ 1 \leq i,k \leq M,\ i < k$ are the cross–Wigner terms. The number of the auto–components in Eq. 4.3 is $M$, while the number of the cross–terms is $M(M-1)/2$.

For a 3 component signal $x(t) = \sum_{i=1}^{3} s_i(t)$ as illustrated in Fig. 4.1, there will be 3 cross–Wigner terms. Cross–Wigner terms arising from the interaction of the individual auto–components of the signal are called as *cross-cross* terms ($W_{s_1 s_2},\ W_{s_1 s_3}$, and $W_{s_2 s_3}$ in Fig. 4.1) and those arising due to the non-linear time–frequency support of the auto-component as *auto–cross* terms as can be seen inside the $W_{s_3}$ in Fig. 4.1. The cross–terms are highly oscillatory, might have a peak value as high as twice that of the auto–components [46, 47] and lie at mid–time and mid–frequency of the auto–components. For the WD illustrated in Fig. 4.1, the support of the cross–cross term $W_{s_1 s_2}(t,f)$ is confined to the following interval:

$$W_{s_1 s_2}(t,f) = 0 \;\; \text{for} \; \begin{cases} t & \text{outside} \;\; [\frac{t_1+t_3}{2}, \frac{t_2+t_4}{2}] \\ f & \text{outside} \;\; [\frac{f_1+f_3}{2}, \frac{f_2+f_4}{2}] \end{cases} \quad , \tag{4.4}$$

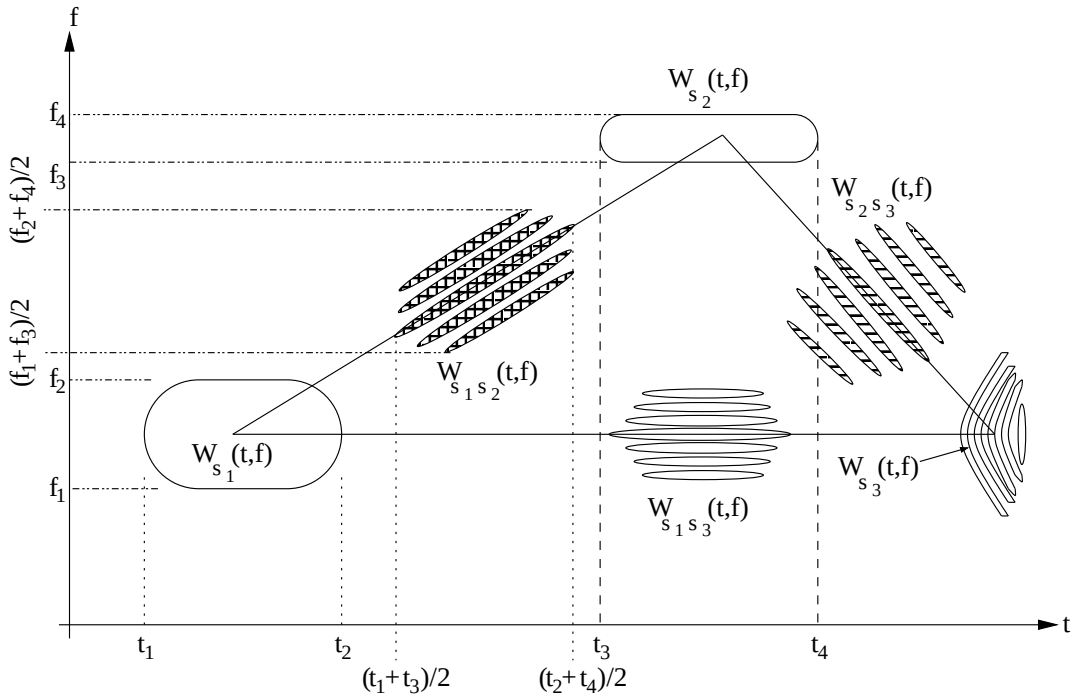


Figure 4.1: Illustration of the geometry of the cross–cross and auto–cross Wigner terms on the time–frequency plane. Cross-cross terms exist in between auto–components in the WD. As seen inside the $W_{s_3}$, auto–cross terms arise due to the nonlinear time–frequency support of the components.

where $[t_1, t_2]$, $[t_3, t_4]$ are the time–domain and $[f_1, f_2]$, $[f_3, f_4]$ are the frequency–domain supports of the components $s_1(t)$ and $s_2(t)$, respectively.

To have a practically useful time–frequency distribution, the cross–terms should be suppressed. Low–pass filtering of the WD will reduce the cross–term interference because of the oscillatory nature of the cross–terms, on the other hand will broaden the time–frequency support of the auto–term concentration, hence resulting in resolution degradation. The broadening of the auto–terms may cause closely spaced components to be identified as only one component. The time–frequency distributions obtained by 2-D low-pass filtering of the WD are known as Cohen's bilinear class of time–frequency representations [45, 46] and in this case the time–frequency distribution $TF_x(t, f)$ of a signal $x(t)$ is

given by

$$TF_x(t,f) \triangleq \int\int \kappa(\nu,\tau) A_x(\nu,\tau) e^{-j2\pi(\nu t+\tau f)}\, \mathrm{d}\nu\, \mathrm{d}\tau \quad , \tag{4.5}$$

where the smoothing function $\kappa(\nu,\tau)$ is usually called as the kernel of the distribution and the symmetric ambiguity function $A_x(\nu,\tau)$ is the inverse Fourier transform of the WD:

$$A_x(\nu,\tau) = \int\int W_x(t,f) e^{j2\pi(\nu t+\tau f)}\, dt\, df \quad . \tag{4.6}$$

A fixed kernel $\kappa(\nu,\tau)$ can provide the 2-D smoothing well only for a limited class of signals, therefore the kernel must be adapted to the characteristics of input signal to obtain a data–adaptive smoothing [48]. Relying on the fact that cross–terms lie away from the origin, and auto–terms lie around the origin in the ambiguity plane [46] data dependent kernels are designed by analyzing the geometry of the auto and cross terms in the ambiguity plane. Although computationally expensive, this approach provides better time–frequency representations.

Although not belonging to the Cohen's bilinear class of time–frequency distributions, a recently developed algorithm by Özdemir and Arıkan [30] named *Time–Frequency Component Analyzer (TFCA)*, provides the most desirable features of a useful distribution: very high auto–term concentration with negligible cross–term interference whether the individual signal components have linear or curved time–frequency supports. A distinct feature of the new algorithm is that, it provides the time–domain representation of the constituent components of the composite signal with unprecedented accuracy, which is of prime importance in the analysis of the ERP signals. Moreover, the TFCA provides the corresponding representations for the extracted signal components

for detailed post–processing which may include computation of statistical parameters from the individual time–frequency supports of the components such as the time center, frequency center, time–spread and the frequency spread. Another favorable feature of the TFCA is that, it has a fast and efficient digital implementation for discrete–time signals.

## 4.2 The TFCA Technique

The flow–chart of the TFCA technique is given in Fig. 4.2 and the steps of the algorithm are described in the following sections. The analytic signal is used in the TFCA to get rid of the cross–term interference arising from the interaction of the symmetric positive and negative frequency components of the real signals.

As seen from the flow chart of TFCA ( Fig. 4.2 ), the time–frequency support and spine of the auto–components of the multi–component signal $x(t)$ are identified from the Wigner distribution $W_x(t, f)$. Therefore digital computation of the WD whose definition is given in Eq. 4.1 is required. Although a number of different discrete–time/frequency Wigner distribution definitions [49,50] exists, TFCA technique uses an efficient one to compute the WD samples along arbitrary line segments on the time–frequency plane [51].

Prior to obtaining the samples of the WD, $x(t)$ is scaled so that its WD support is approximately confined into a circle with radius $\Delta_x/2$ centered at the origin. Assuming $x(t)$ has approximate time and bandwidth $\Delta_t$ and $\Delta_f$ respectively, the required scaling is $x(t/s)$ where $s = \sqrt{\Delta_f/\Delta_t}$. Scaling is done to obtain an equally valid approximation of the WD and to be able to use the

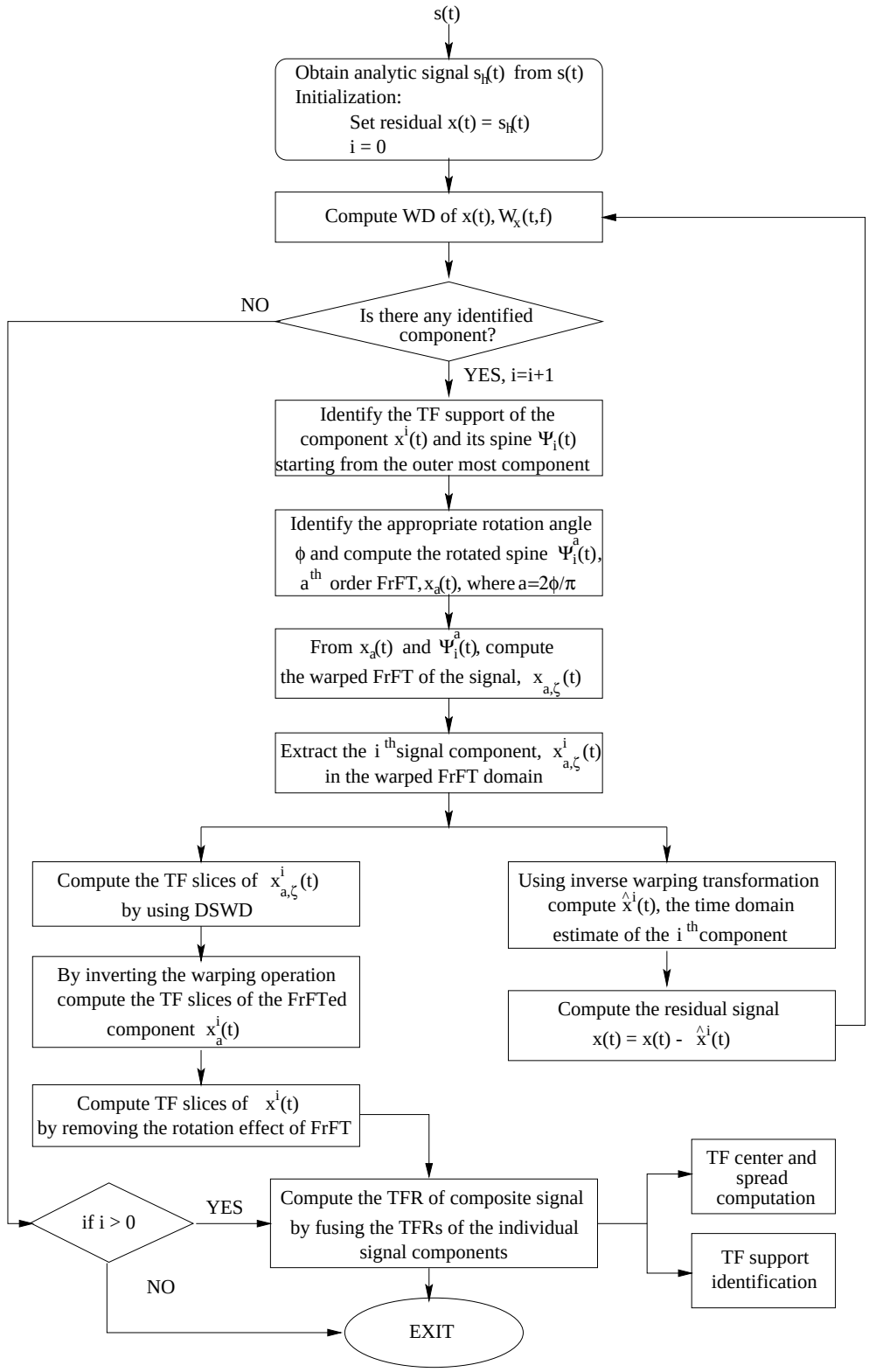


Figure 4.2: The flow–chart of the Time Frequency Component Analyzer (TFCA) technique.

fast fractional Fourier transform (FrFT) algorithm given in [52]. The relation between the WD and FrFT will be evident in the next section.

### 4.2.1 Computation of the WD Along Arbitraty Line Segments

The WD slices and the Radon transform of the ambiguity function are related to each other by the projection slice theorem [53]. As shown in Eq. 4.6, the ambiguity function $A_x(\nu,\tau)$ is the 2-D inverse Fourier transform of the WD and it can be written in terms of the signal $x(t)$ as

$$A_x(\nu,\tau) = \int x(t+\tau/2)x^*(t-\tau/2)e^{j2\pi\nu t}\ dt \quad . \tag{4.7}$$

From the projection slice theorem [53], $W_x(\lambda\cos\phi, \lambda\sin\phi)$, the radial slice of the Wigner distribution of a signal $x(t)$ which makes an angle $\phi$ with the time axis, can be expressed as:

$$W_x(\lambda\cos\phi, \lambda\sin\phi) = \int Q_x(r,\phi)e^{-j2\pi r\lambda}\ dr \quad , \tag{4.8}$$

where $Q_x(r,\phi)$, the Radon transform of the ambiguity function, is defined as

$$Q_x(r,\phi) = \int A_x(r\cos\phi - s\sin\phi, r\sin\phi + s\cos\phi)\ ds \quad . \tag{4.9}$$

From Eq. 4.8, it is obvious that the radial slice of the Wigner distribution is the FT of the Radon transform of the ambiguity function $Q_x(r,\phi)$ with respect to the radial variable $r$. An efficient computational algorithm that relates $Q_x(r,\phi)$ to the $(a-1)^{th}$ order fractional Fourier transform of the signal, $x_{(a-1)}(t)$, is described in Appendix B.1:

$$Q_x(r,\phi) = x_{(a-1)}(\frac{r}{2})x^*_{(a-1)}(-\frac{r}{2}) \quad , \tag{4.10}$$

where $a = \frac{2\phi}{\pi}$.

The $a^{th}$ order fractional Fourier transform (FrFT) is a linear operation defined by [52]

$$x_a(t) = \{\mathcal{F}^a x\}(t) \triangleq \int K_a(t,t')x(t')\ dt' \quad , \tag{4.11}$$

where $a \in \Re$, $0 < |a| < 2$ and $K_a(t,t')$, the kernel of the transformation, is given by the following set of equations:

$$\begin{aligned} K_a(t,t') &= A_\phi\ exp\left[j\pi(t^2\cot\phi - 2tt'\csc\phi + t'^2\cot\phi)\right] \quad , \\ A_\phi &= \frac{e^{-j\pi sgn(\sin\phi)/4 + j\phi/2}}{\sqrt{|\sin\phi|}} \quad , \\ \phi &= \frac{a\pi}{2} \quad . \end{aligned} \tag{4.12}$$

The transformation kernel of FrFT is $\delta(t)$ for $a = 0$, thus $0^{th}$ order FrFT is the function itself. For $a = 1$, kernel becomes the complex exponential $e^{-j2\pi tt'}$ and $1^{st}$ order FrFT is the ordinary Fourier transform. Various other properties of the FrFT can be found in [52, 54].

In a more general case, where the samples of the WD of $x(t)$ is to be computed along an arbitrary line segment $L_w$ (see Fig. 4.3) parameterized as

$$L_W = \{(t,f) | t = t_0 + \lambda\cos\phi, f = f_0 + \lambda\sin\phi, \lambda_i \le \lambda \le \lambda_f\} \quad , \tag{4.13}$$

where $(t_0, f_0)$ is an arbitrary point on $L_w$ and $\phi$ is the angle that $L_w$ makes with the time axis, we express the non–radial slice of the WD of $x(t)$ as a radial slice of the WD of another function $y(t)$.

Substitution of $(t,f)$ values given in the $L_w$ parametrization into the definition of the WD (Eq. 4.1)

$$\begin{aligned} W_x(t_0 + \lambda\cos\phi, f_0 + \lambda\sin\phi) &= \int x(t_0 + \lambda\cos\phi + t'/2)x^*(t_0 + \lambda\cos\phi - t'/2) \\ &\quad e^{-j2\pi(f_0 + \lambda\sin\phi)t'}\ dt' \quad , \end{aligned} \tag{4.14}$$

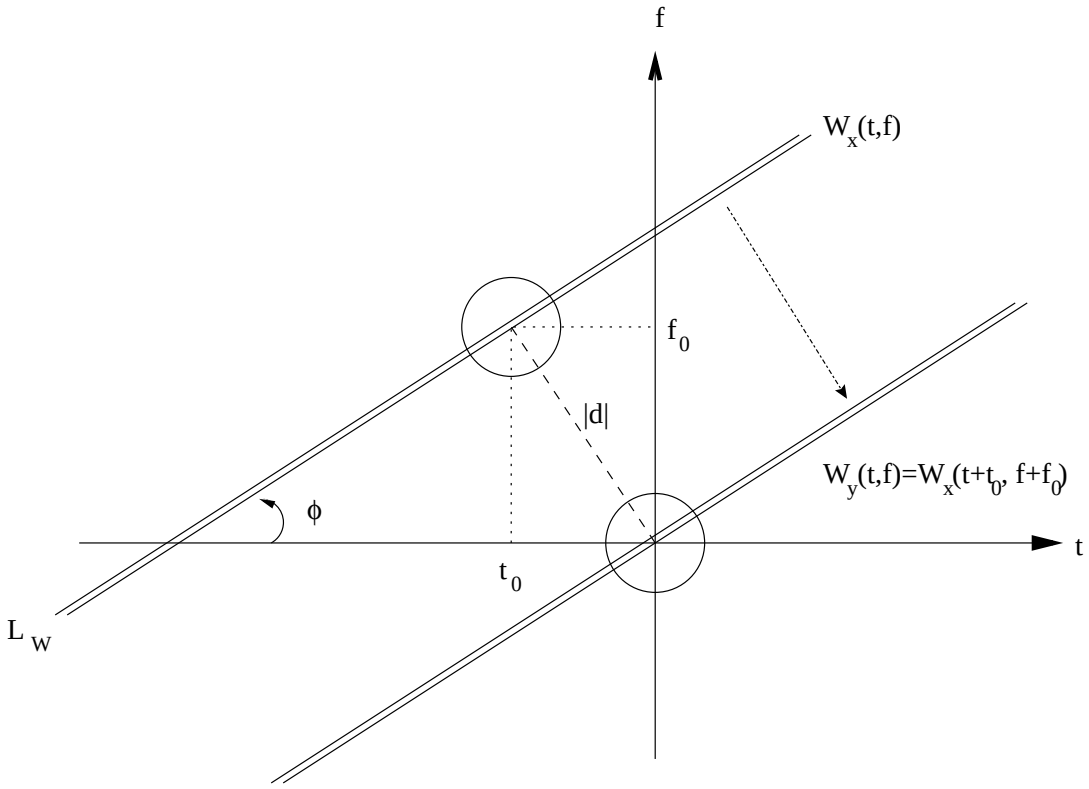


Figure 4.3: Illustration of the radial and non–radial slices in the computation of the Wigner distribution.

is obtained. From the time–frequency shift invariance of the WD distribution [47], stating that for $y(t) = x(t + t_0)e^{-j2\pi f_0 t}$

$$W_y(t, f) \;=\; W_x(t + t_0, f + f_0) \quad , \tag{4.15}$$

the non–radial slice of the WD in Eq. 4.14 is equivalent to the radial slice of the WD of the function $y(t) = x(t + t_0)e^{-j2\pi f_0 t}$:

$$W_x(t_0 + \lambda\cos\phi, f_0 + \lambda\sin\phi) \equiv W_y(\lambda\cos\phi, \lambda\sin\phi) \quad . \tag{4.16}$$

As seen from Fig. 4.3, radial and non-radial slices are in parallel. From the projection slice theorem, the non–radial slice of the WD of $x(t)$ can be obtained from $Q_y(r, \phi)$ as

$$W_x(t_0 + \lambda\cos\phi, f_0 + \lambda\sin\phi) = \int Q_y(r, \phi)e^{-j2\pi r\lambda}\, dr \quad . \tag{4.17}$$

The efficient computation of $Q_y(r,\phi)$ is possible through the following relationship (see Appendix B.1):

$$Q_y(r,\phi) = y_{(a-1)}(\frac{r}{2})y^*_{(a-1)}(-\frac{r}{2}) \quad , \tag{4.18}$$

where $a = \phi/(\pi/2)$. Appendix B.1 also contains the formulation that relates $Q_y(r,\phi)$ to the $(a-1)^{th}$ FrFT of the original signal $x(t)$:

$$Q_y(r,\phi) = x_{(a-1)}(\frac{r}{2}+d)x^*_{(a-1)}(-\frac{r}{2}+d) \quad , \tag{4.19}$$

where in polar format $(d, \phi+\pi/2)$ is the closest point on the non–radial slice of the WD to the origin as shown in Fig. 4.3.

The discrete approximation of the integral in Eq. 4.17 can be obtained by using its Riemann sum and discretizing the frequency variable $\lambda$. The chirp transform algorithm used in this discrete approximation is described in Appendix C.

In the special case when $\phi = \pi/2$, $a$ is 1, therefore the order of the FrFT in Eq. 4.19 becomes 0. The $0^{th}$ order FrFT of a function is the function itself. Since the non–radial slice is perpendicular to the time axis, $d = 0$, Eq. 4.19 becomes

$$Q_y(r,\frac{\pi}{2}) = x(\frac{r}{2})x^*(-\frac{r}{2}) \quad . \tag{4.20}$$

In this case $r$ is the time variable, and this function is used in the computation of the WD on rectangular grids.

### 4.2.2 Directional Smoothing of The WD

To eliminate the cross–terms that may exist in the Wigner distribution of a multi–component signal, low–pass filtering may be applied at the expense of

broadening of the auto–components. However auto–components may not have a low–pass characteristics along all orientations [48]. Özdemir and Arıkan proposed the directional smoothing algorithm of the Wigner distribution (DSWD) [48] by using low–pass filters with data-adaptive cut–off frequencies.

As detailed in the previous section, the non–radial slice of the WD of $x(t)$ is equivalent to the radial slice of the WD of $y(t)$, $W_y$. By denoting the radial slice of $W_y$ as $\mathcal{SLC}[W_y](\lambda,\phi) \equiv W_y(\lambda\cos\phi, \lambda\sin\phi)$, the slice of the filtered Wigner distribution $s(\lambda,\phi)$ is obtained from

$$s(\lambda,\phi) = h(\lambda) \overset{\lambda}{\star} \mathcal{SLC}[W_y](\lambda,\phi) \quad . \tag{4.21}$$

where $h(t)$ is the impulse response of the real smoothing filter. Equation 4.8 indicates that the inverse Fourier transform (FT) of $\mathcal{SLC}[W_y](\lambda,\phi)$ is $Q_y(r,\phi)$, therefore taking the inverse FT of Eq. 4.21 gives

$$S(r,\phi) = H(r)Q_y(r,\phi) \quad , \tag{4.22}$$

where $S(r,\phi)$ is the inverse FT of the slice $s(\lambda,\phi)$ with respect to the radial variable $\lambda$, and $H(r)$ is the inverse FT of the smoothing filter $h(t)$. This filtering process of $Q_y(r,\phi)$ can be applied to different slices where the cut–off frequencies of $H(r)$ are adaptively determined from the auto–component location on $Q_y(r,\phi)$.

### 4.2.3 Warped Time–Frequency Analysis

Time–frequency distribution of an auto–component with a curved time–frequency support will be cluttered with auto–cross terms [46]. To obtain clutter–free time–frequency representations of these components, the TFCA uses the fractional domain warping concept [30, 41].

Mathematically, warping is the operation of replacing the time dependence of a signal $x(t)$, with a warping function $\zeta(t)$. For the invertibility of the warping operation, $\zeta(t)$ should be chosen as a one–to–one function. To approximate the effect of warping on the samples of a continuous signal, the warping function is chosen as a differentiable one [41].

For a frequency modulated (FM) signal $x(t)$,

$$x(t) = A(t)e^{j2\pi\phi(t)} \quad , \tag{4.23}$$

where $A(t)$ is the nonnegative amplitude and $\phi(t)$ is the phase, by choosing the warping function as the inverse of the phase [41]:

$$\zeta(t) = \phi^{-1}(f_s t) \qquad f_s > 0 \quad , \tag{4.24}$$

where $f_s$ is an arbitrary scaling constant, the warped function $x_\zeta(t)$ takes the following form

$$x_\zeta(t) = A(\zeta(t))e^{j2\pi f_s t} \quad , \tag{4.25}$$

which is an amplitude modulated (AM) signal with carrier frequency $f_s$. Generalization of the time–domain warping to fractional domains produced the fractional domain warping concept [41], where, instead of warping the time signal $x(t)$, the $a^{th}$ ($a \in \Re$) order FrFT of the signal $x_a(t)$ is warped by the following set of equations:

$$x_a(t) = \{\mathcal{F}^a x\}(t) \triangleq \int K_a(t,t')x(t')\,dt' \tag{4.26}$$

$$x_{a,\zeta}(t) = x_a(\zeta(t)) \quad . \tag{4.27}$$

The fractional domain warping makes use of the rotation property of the FrFT which states that, the WD of the $a^{th}$ order FrFT of a signal is the same

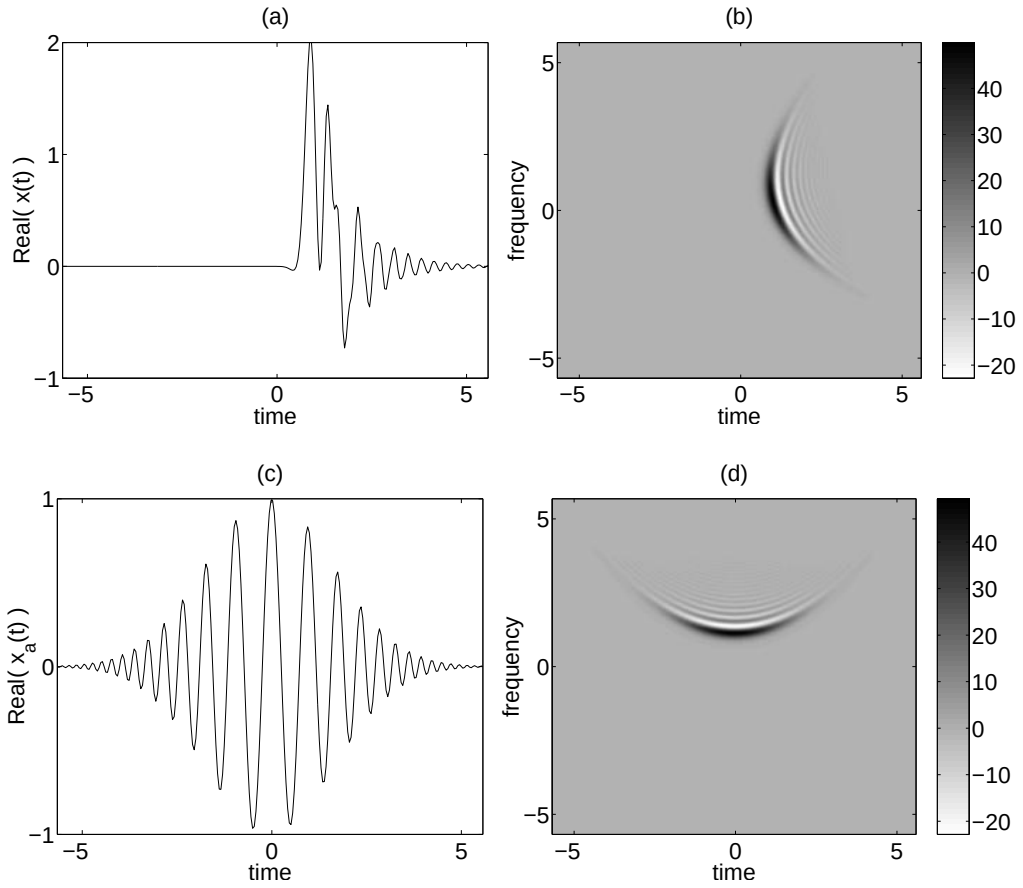


Figure 4.4: Time–domain signal $x(t)$ of the nonlinear-chirp given in (a) has the WD shown in (b). The WD (d) of the $a^{th}$ order FrFT of $x(t)$, $x_a(t)$ given in (c) is the $0.85 * \pi/2$ counter–clockwise rotated WD of (b).

as the WD of the original signal rotated by an angle of $a\pi/2$ radians in the clock–wise direction [52, 53]. Time–domain warping may not be useful for the processing of a signal that does not have a single–valued instantaneous frequency such as the non–linear chirp shown in Fig. 4.4 (a), on the other hand its $a^{th}$ order FrFT ($a = -0.85$ in this case) may be suitable for such a processing as shown in Fig. 4.4 (c) and (d). The order of the FrFT, $a$, is selected in such a way that the time–frequency support of $x_a(t)$, or equivalently that of $x(t)$ rotated by $a\pi/2$ radians in the clock–wise direction have a single–valued instantaneous frequency with respect to time. Hence, the invertibility of the warping operation is assured, because the rotated spine $\psi_a(t)$ is a single valued function of time as shown in Fig. 4.5.

For the non–linear chirp whose WD is shown in Fig. 4.4 (b), $a = -0.85$. Thus, the WD is rotated $a\pi/2 = -0.85 * \pi/2$ radians (-76.5 degrees) in the clock–wise direction which is equivalent to $0.85 * \pi/2$ radians (76.5 degrees) counter clock–wise rotation.

### 4.2.4 Warping Function

In TFCA, the warping function is found from a spine, $\psi_a(t)$, which is an approximation to the instantaneous frequency of $x_a(t)$. The spine can be obtained either from an instantaneous frequency estimation algorithm or by manually marking some of its coordinates $(t_i, f_i),\ 1 \leq i \leq N$ on the time–frequency plane. For the sake of simplicity, the points of the spine are manually specified by using a user–friendly GUI of the TFCA, and they are connected by using spline interpolation.

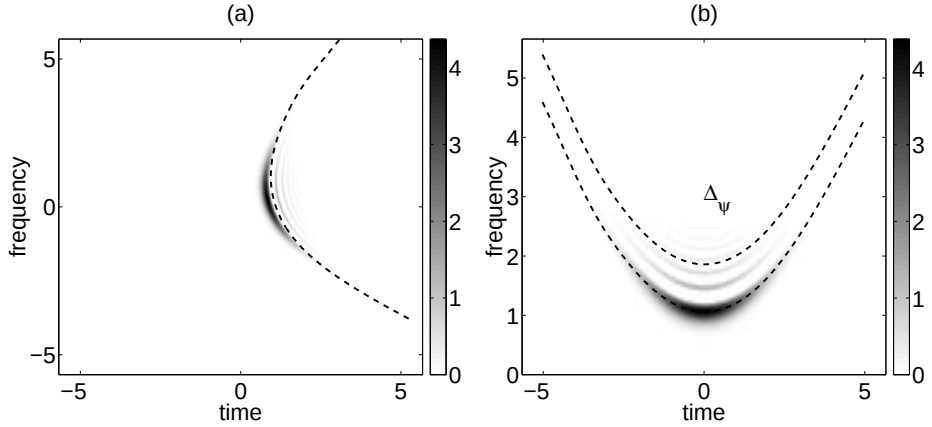


Figure 4.5: The original spine $\psi(t)$ shown in (a), which is an approximation to the instantaneous frequency, isn't a single–valued function of time where the rotated spine, $\psi_a(t)$, in (b) is, $a = -0.85$.

Equation 4.24 states the relationship between the warping function and the phase of the FM signal. The instantaneous frequency, $f_i(t)$ of a signal is the derivative of its phase $\phi(t)$: $f_i(t) = d\phi(t)/dt$. Thus, assuming that the time support of the signal is limited to $[t_1, t_N]$, the phase can be obtained from the instantaneous frequency by integration:

$$\phi(t) = \int_{t_1}^{t} f_i(t)\ dt, \qquad t \leq t_N \quad . \tag{4.28}$$

Since the spine is an approximation of the instantaneous frequency of $x_a(t)$, the inverse of the warping function, the phase is computed by

$$\Gamma(t) = \int_{t_1}^{t} [\psi_a(t') + \delta_f]\ dt' \ , \ t_1 \leq t \leq t_N \tag{4.29}$$

$$\zeta^{-1}(t) = \Gamma(t)/f_{\psi_a} + t_1 \ , \ t_1 \leq t \leq t_N \tag{4.30}$$

$$f_{\psi_a} = \Gamma(t_N)/(t_N - t_1) \quad , \tag{4.31}$$

where $f_{\psi_a}$ is the mean of the spine and $\delta_f$ is the required frequency shift on the spine to make it a strictly positive function of time. Since $\psi_a(t) + \delta_f$ is a strictly positive function of time, $\Gamma(t)$ defined in Eq. 4.29 is a monotonically

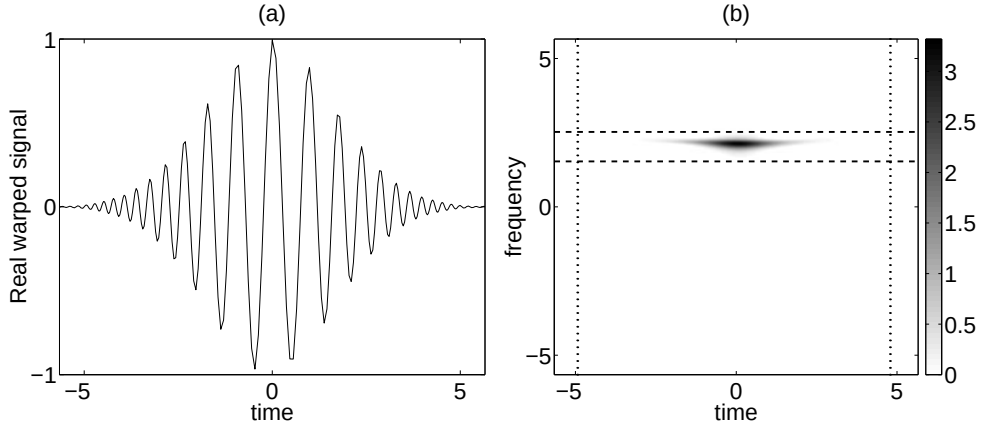


Figure 4.6: Warped signal $x_{a,\zeta}^{\delta_f}(t)$ ($\delta_f = 1$) given in (a) has an almost linear time–frequency support parallel to the time axis (b).

increasing function, therefore its inverse, the warping function

$$\zeta(t) = \Gamma^{-1}(f_{\psi_a}(t - t_1)) \ , \ t_1 \leq t \leq t_N \quad , \tag{4.32}$$

exists and it is unique.

In time–frequency analysis, when the frequency shift $\delta_f$ used in Eq. 4.29 is nonzero, instead of warping $x_a(t)$ it is more appropriate to warp the frequency modulated version of it $x_a^{\delta_f}(t) \triangleq e^{j2\pi\delta_f t} x_a(t)$ whose spine is $\psi_a(t) + \delta_f$. In this case, the warping operation defined in Eq. 4.26 becomes

$$x_a^{\delta_f}(t) \ = \ e^{j2\pi\delta_f t} \ \{\mathcal{F}^a x\}(t) \tag{4.33}$$

$$x_{a,\zeta}^{\delta_f}(t) \ = \ e^{-j2\pi\delta_f t} \ x_a^{\delta_f}(\zeta(t)) \quad . \tag{4.34}$$

The warped version, $x_{a,\zeta}^{\delta_f}(t)$ of the signal $x_a(t)$ shown in Fig. 4.4, is given in Fig. 4.6 (a).

### 4.2.5 DSWD of Warped Component

After the warping operation, the time–frequency support of the warped signal $x_{a,\zeta}^{\delta_f}(t)$ given in Fig. 4.6 (a) is localized around the line segment $(\lambda, f_{\psi_a}), t_1 \leq \lambda \leq t_N$, hence it becomes almost linear as shown in Fig. 4.6 (b). The WD of this mono–component signal with linear time–frequency support is a high–resolution time–frequency description with negligible auto–cross term interference. On the other hand, due to the cross–cross terms that may reside on the warped component for more general multi–component signals and additive noise on the WD plane, the performance of the WD may decrease. Therefore the time–frequency distribution, $\mathcal{TF}_{x_{a,\zeta}}(t,f)$ , of the warped signal $x_{a,\zeta}^{\delta_f}(t)$ is computed by directionally smoothing the slices of the WD as detailed in Section 4.2.2.

From the directionally smoothed WD slice of the warped signal on the line segment $(\lambda, f_{\psi_a}),\ t_1 \leq \lambda \leq t_N$, the slice of the time–frequency distribution $\mathcal{TF}_{x_a}(t,f)$ lying on the spine $\psi_a(t)$ is computed as

$$\mathcal{TF}_{x_a}(\zeta(\lambda), \psi(\zeta(\lambda))) = \mathcal{TF}_{x_{a,\zeta}}(\lambda, f_{\psi_a}),\ t_1 \leq \lambda \leq t_N \quad . \tag{4.35}$$

The other slices of $\mathcal{TF}_{x_a}(t,f)$ lying $\Delta_\psi$ away from the spine $\psi_a(t)$ as shown in Fig. 4.5 (b), are obtained by using the frequency shifting property of the time–frequency distribution obtained by the TFCA:

$$\mathcal{TF}_{x_a}(t, f+\Delta_\psi) = \mathcal{TF}_{y_a}(t,f) \quad , \tag{4.36}$$

where $y_a(t)$ is the linearly frequency modulated version of $x_a(t)$: $y_a(t) = x_a(t)e^{j2\pi\Delta_\psi t}$. In this case, instead of the signal $x_a(t)$, its frequency modulated version $y_a(t)$ should be warped. Combining Equations 4.35 and 4.36 gives

$$\mathcal{TF}_{x_a}(\zeta(\lambda), \Delta_\psi + \psi(\zeta(\lambda))) = \mathcal{TF}_{y_{a,\zeta}}(\lambda, f_{\psi_a}),\ t_1 \leq \lambda \leq t_N \quad . \tag{4.37}$$

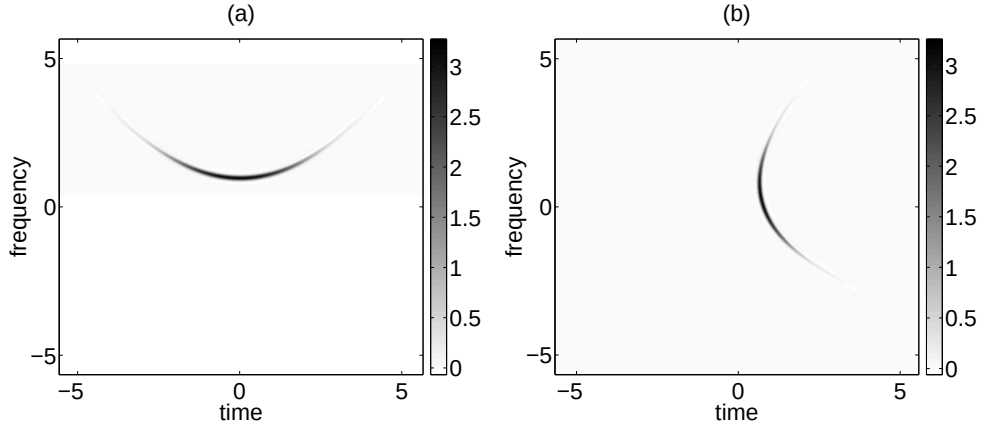


Figure 4.7: When the rotation effect of the FrFT is removed from the directionally smoothed WD given in (a) by rotating it $-a\pi/2$ (76.5 degrees) radians clock–wise, the high resolution time–frequency distribution of the original signal given in (b) is obtained.

Equation 4.37 is used to compute the slice of the distribution $\mathcal{TF}_{x_{a,\zeta}}(t,f)$ on a curve parameterized as $(t(\lambda), f(\lambda)) = (\zeta(\lambda), \psi(\zeta(\lambda)) + \Delta_\psi)$. By using different values of $\Delta_\psi$, the TFCA can provide different slices of the time–frequency distribution of $x_a(t)$, thus time–frequency representation of $x_a(t)$ on a region of time–frequency plane can be obtained. By using the GUI of the TFCA, the user selects this region manually. The high resolution time–frequency distribution obtained for $x_a(t)$ is shown in Fig. 4.7 (a).

To remove the rotation effect induced by the FrFT, each slice of $\mathcal{T}F_{x_a}(t,f)$ is rotated back by $a\pi/2$ radians counter clock–wise, and the slices of the time–frequency representation $\mathcal{T}F_x(t,f)$ of $x(t)$ are obtained from

$$\mathcal{T}F_x(t_r(\lambda), f_r(\lambda)) = \mathcal{T}F_{x_a}(\zeta(\lambda), \psi(\zeta(\lambda)) + \Delta_\psi) \quad , \tag{4.38}$$

where $(t_r(\lambda), f_r(\lambda))$ defines a new curve in the time–frequency plane parameterized with the variable $\lambda$:

$$t_r(\lambda) \;\; = \;\; \zeta(\lambda)\cos(a\pi/2) - (\psi(\zeta(\lambda)) + \Delta_\psi)\sin(a\pi/2)$$

$$f_r(\lambda) \;=\; \zeta(\lambda)\sin(a\pi/2) + (\psi(\zeta(\lambda)) + \Delta_\psi)\cos(a\pi/2) \quad . \tag{4.39}$$

The resultant time–frequency distribution of $x(t)$ obtained by rotating $\mathcal{TF}_{x_a}(t,f)$ given in Fig. 4.7 (a) $a\pi/2$ radians counter clock–wise is shown in Fig. 4.7 (b).

### 4.2.6 Time–Frequency Masking

After the warping and DSWD operations, the obtained time–frequency distribution $\mathcal{TF}_{x_{a,\zeta}}(t,f)$ has an almost linear time–frequency support which is free of cross–terms. To extract this component from the overall signal a time–frequency mask, whose parameters are defined by the time–frequency support of the component, is applied to the signal. Firstly, a frequency domain mask, $H_1(f)$ with a support equal to the frequency axis projection of the component is applied to the warped signal $x^{\delta_f}_{a,\zeta}(t)$ . Then to the resultant signal, a time–domain mask, $h_2(t)$ with a support equal to the projection of the component on the time–axis, is applied to obtain the estimate of the component:

$$\hat{x}^{\delta_f}_{a,\zeta}(t) = h_2(t)\;[h_1(t) * x^{\delta_f}_{a,\zeta}(t)] \quad , \tag{4.40}$$

where $h_1(t)$ is the inverse Fourier transform of the frequency–domain mask $H_1(f)$. After estimating the warped time–domain component an estimate of the original component can be obtained.

### 4.2.7 Estimation of the Time–Domain Components

Having obtained the time–domain estimate $\hat{x}_{a,\zeta}^{\delta_f}(t)$, the estimate of the original component, $\hat{x}(t)$ can be computed by the following set of equations:

$$\hat{x}_a^{\delta_f}(t) = e^{j2\pi\delta_f\zeta^{-1}(t)}\hat{x}_{a,\zeta}^{\delta_f}(\zeta^{-1}(t)) \quad (4.41)$$

$$\hat{x}_a(t) = e^{-j2\pi\delta_f t}\hat{x}_a^{\delta_f}(t) \quad (4.42)$$

$$\hat{x}(t) = \{\mathcal{F}^{-a}\hat{x}_a(t)\}(t) \ , \quad (4.43)$$

where Eq. 4.41 inverts the warping operation, Eq. 4.42 removes the frequency modulation $\delta_f$, and Eq. 4.43 takes the $(-a)^{th}$ order FrFT of $\hat{x}_a(t)$.

## 4.3 Multi–Component Signal Analysis in TFCA

Previous section described the TFCA technique for a mono–component signal. For a multi–component signal, TFCA starts with the identification of one of the components on the time–frequency plane as shown in the flowchart of the algorithm, Fig. 4.2. The identified component should be free of cross–terms. It was stated in Section 4.1 that cross–terms lie in mid–time and mid-frequency of the auto–components, therefore by selecting the outer–most component in the time–frequency plane we assure that it is cross–term free. After processing the selected auto–component, TFCA obtains its time–domain estimate and subtracts it from the original signal. The steps of the algorithm are iterated for each component on the residual signal. The time–frequency representations of each component are fused to obtain the composite time–frequency distribution of the multi–component signal at the end.

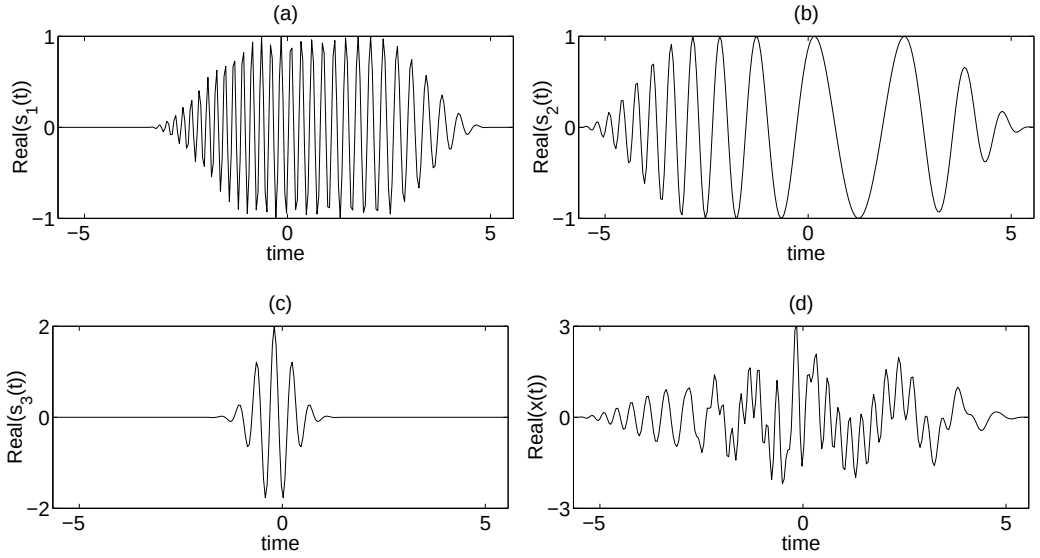


Figure 4.8: Synthetic signal $x(t) = \sum_{i=1}^{3} s_i(t)$ (d) used in the performance illustration of the TFCA is composed of a linear chirp (a), $s_1(t)$, a non–linear chirp (b), $s_2(t)$, and a constant frequency modulated signal (c), $s_3(t)$.

To illustrate the performance of the TFCA, a synthetic signal $x(t) = \sum_{i=1}^{3} s_i(t)$ with 3 components is analyzed. The components are chosen such that $s_1(t)$ is a linear, $s_2(t)$ is a hyperbolic and $s_3(t)$ is a constant frequency modulated signal and all have Gaussian modulated amplitudes. The individual components and the multi–component signal $x(t)$ are shown in Fig. 4.8. From the WD of $x(t)$ shown in Fig. 4.9 (a), it is evident that the third component $s_3(t)$ is completely immersed under cross–cross terms arising from the interaction of $s_1(t)$ and $s_2(t)$. Notice also the auto–cross terms of the hyperbolic frequency modulated component $s_2(t)$.

After the examination of the WD of $x(t)$ given in Fig. 4.9 (a), $s_1(t)$ is selected as the first component to be analyzed, it lies at the periphery of the Wigner plane, hence it is not contaminated by the existence of cross–cross terms. After the extraction of the estimate of the first component $\hat{s_1}(t)$, the

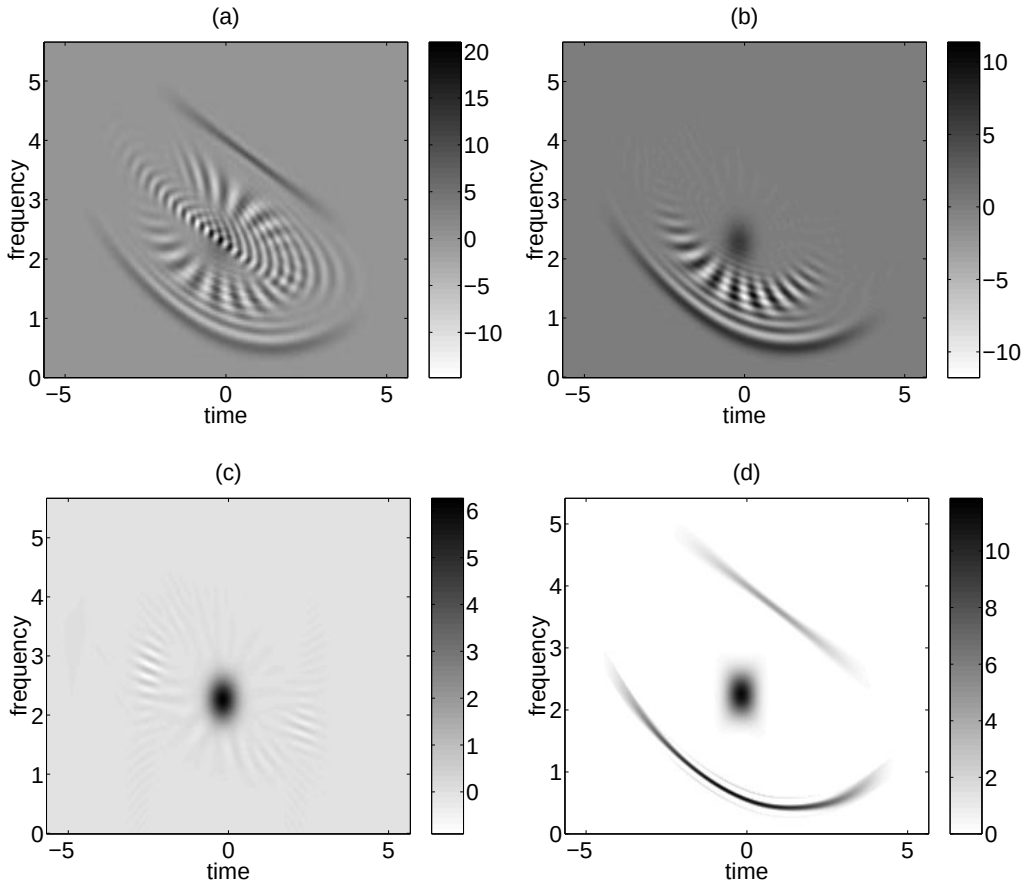


Figure 4.9: In the WD of the synthetic signal given in Fig. 4.8 (d), $s_3(t)$ is immersed under cross–cross term interference. WD of the residual signals after the extraction of $\hat{s_1}(t)$ and $\hat{s_2}(t)$ are given in (b) and (c), respectively. TFCA provides high–resolution time–frequency distribution of the synthetic multi–component signal as shown in (d).

residual signal $r(t) = x(t) - \hat{s_1}(t)$ has the WD shown in Fig. 4.9 (b). Now the time–frequency support of $s_3(t)$ can be identified easily. In the second iteration, the component that has the hyperbolic frequency modulation is extracted leaving the WD in Fig. 4.9 (c). Third and the last component is easily extracted. Thus, TFCA provided the composite time–frequency distribution for the synthetic multi–component signal $x(t)$ as shown in Fig. 4.9 (d). The time–domain estimates of the extracted components $\hat{s_1}(t)$, $\hat{s_2}(t)$ and $\hat{s_3}(t)$ with the estimation errors are plotted in Fig. 4.10. Notice that the estimation errors are very small. As illustrated in this simulation, the TFCA provides very accurate time–domain representation of the components.

## 4.4 Estimation of Time–Frequency Center and Spread of Extracted Components

The time–frequency representations of the individual components of a multi–component signal obtained by the TFCA may be visually suspected or statistical descriptors that distinguishes components from each other are obtained. For this purpose time–frequency center, time spread, and frequency spread of each component are computed. Here the idea is that the center and spread values of different components can be used for comparison in clinical studies.

For a component image, $W$, with a size of $[M, N]$, time–center $t_m$ of the component is found from

$$t_m = \frac{\sum_{n=0}^{N-1} \sum_{m=0}^{M-1} t[n] \ |W[m,n]|}{\sum_{n=0}^{N-1} \sum_{m=0}^{M-1} |W[m,n]|} \quad , \tag{4.44}$$

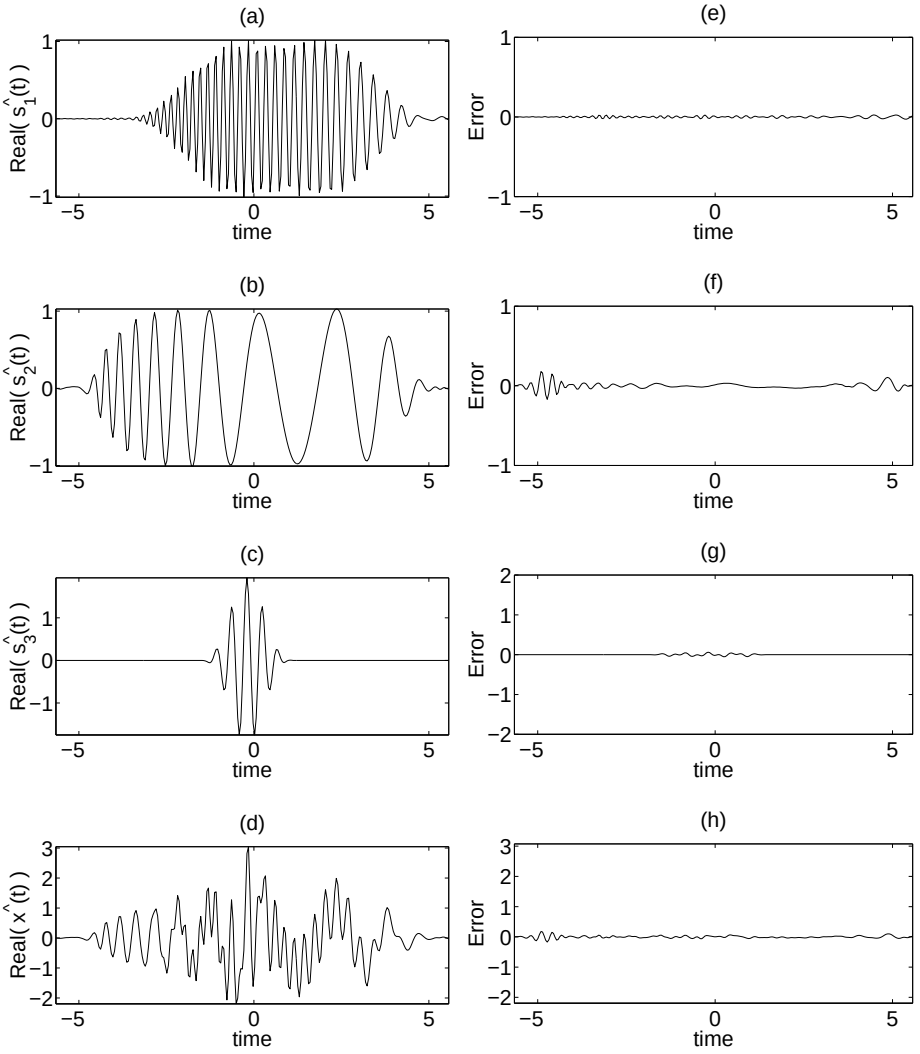


Figure 4.10: Time–domain components extracted by TFCA from the multi–component synthetic signal $x(t)$: $\hat{s_1}(t)$, $\hat{s_2}(t)$, $\hat{s_3}(t)$, and $\hat{x}(t)$ are given in (a)-(d) and the errors in (e)-(h), respectively.

| | Comp #1 | | | Comp #2 | | | Comp #3 | | |
|---|---|---|---|---|---|---|---|---|---|
| | $s_1(t)$ | $\hat{s}_1(t)$ | error | $s_2(t)$ | $\hat{s}_2(t)$ | error | $s_3(t)$ | $\hat{s}_3(t)$ | error |
| $t_m$ (msec) | 798 | 779 | 19 | 0 | -40.7 | 40.7 | -156 | -176.2 | 20.2 |
| $t_v$ (msec) | 1740 | 1436 | 304 | 2523 | 2195 | 328 | 442 | 319.4 | 122.6 |
| $f_m$ (Hz) | 3.75 | 3.7 | 0.05 | 1.35 | 0.9 | 0.45 | 2.32 | 2.3 | 0.02 |
| $f_v$ (Hz) | 0.53 | 0.58 | 0.05 | 0.57 | 0.54 | 0.03 | 0.26 | 0.25 | 0.01 |
| $area$ | 1.22 | | | 1.31 | | | 0.90 | | |

Table 4.1: Estimated time center ($t_m$), frequency center ($f_m$), time spread ($t_v$) and frequency spread ($f_v$) of the extracted components compared to those of the individual original components of the synthetic signal.

where $t[n],\ 0 \leq n \leq N-1$ denotes the time samples. Time spread $t_v$ of the component is computed from

$$t_v^2 = \frac{\sum_{n=0}^{N-1} \sum_{m=0}^{M-1} (t[n] - t_m)^2 \ |W[m,n]|}{\sum_{n=0}^{N-1} \sum_{m=0}^{M-1} |W[m,n]|} \quad . \tag{4.45}$$

In a similar manner, frequency center $f_m$ of the component is found from

$$f_m = \frac{\sum_{n=0}^{N-1} \sum_{m=0}^{M-1} f[m] \ |W[m,n]|}{\sum_{n=0}^{N-1} \sum_{m=0}^{M-1} |W[m,n]|} \quad , \tag{4.46}$$

where $f[m],\ 0 \leq m \leq M-1$ denotes the frequency samples and spread $f_v$ of the component from

$$f_v^2 = \frac{\sum_{n=0}^{N-1} \sum_{m=0}^{M-1} (f[m] - f_m)^2 \ |W[m,n]|}{\sum_{n=0}^{N-1} \sum_{m=0}^{M-1} |W[m,n]|} \quad . \tag{4.47}$$

As shown in Table 4.1, the obtained estimates of the statistical descriptors for the synthetic test signal are highly accurate.

## 4.5 Time–Frequency Support Identification

Similar to the statistical information obtained in the previous section, time–frequency support of the components can also be used in the classification of the

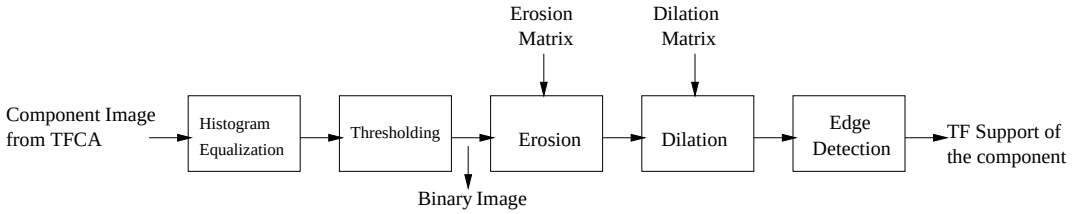


Figure 4.11: Morphological edge detection based time–frequency support identification algorithm.

morphology of the ERP signals under different paradigms. Although visual inspection is always an alternative, numerical computation of the time–frequency supports of the components provides a robust and objective information. In the proposed TFCA based ERP analysis the support is automatically identified by using a well known morphological edge detection algorithm [55] whose block diagram is shown in Fig. 4.11.

The TFCA provides time–frequency representations of the individual components which are almost free of cross–terms. There may exist some residing cross–term interference especially for the components having nonlinear time–frequency supports. To alleviate the destructive effect of these terms on our contour extraction algorithm, image is eroded with a $3 \times 3$ structuring matrix $E$ which determines the neighborhood of the erosion operation. The rule of the erosion is:

- If every pixel in the input pixel's neighborhood is 1, the output pixel = 1. Otherwise, the output pixel is 0.

Images that TFCA produces does not contain much noise, therefore erosion works well. On the eroded image, dilation is done with a $3 \times 3$ structuring matrix $D$. The rule of the dilation is:

- If any pixel in the input pixel's neighborhood is 1, the output pixel = 1. Otherwise, the output pixel is 0.

Hence, some pixels belonging to the component on the image, but turned to 0 by erosion is recovered. Erosion and dilation structuring matrices are

$$E = \begin{bmatrix} 0 & 0 & 1 \\ 1 & \textcircled{1} & 1 \\ 1 & 1 & 1 \end{bmatrix} \quad , \quad D = \begin{bmatrix} 0 & 0 & 1 \\ 0 & \textcircled{1} & 1 \\ 0 & 1 & 1 \end{bmatrix} \quad . \tag{4.48}$$

where the circled entries are the center pixels. The state (i.e., 1 or 0) of any pixel in the output image is determined by applying the erosion or dilation rule to the neighborhood of the selected pixel by overlaying the structuring matrix in the input image so that the center pixel of the matrix is the selected one. This analysis is carried out for all of the pixels in the input image to obtain the output dilated or eroded image. Notice that only the neighborhood pixels corresponding to the nonzero entries in the structuring matrices, $D$, and $E$ are considered.

The required edge detection is performed by finding the discontinuities in the eroded and dilated binary image. The resultant contours of the components of the synthetic signal are shown in Fig. 4.12 (a)-(c) superimposed on their time–frequency representations provided by TFCA. In Fig. 4.12 (d), the supports of the components are shown together.

Alternatively, the TF supports of the extracted signal components could be identified by using active contour models (snake algorithm) [56–58]. The snake algorithm requires the determination of an initial closed contour which is dynamically adapted to minimize an energy term. The energy depends on

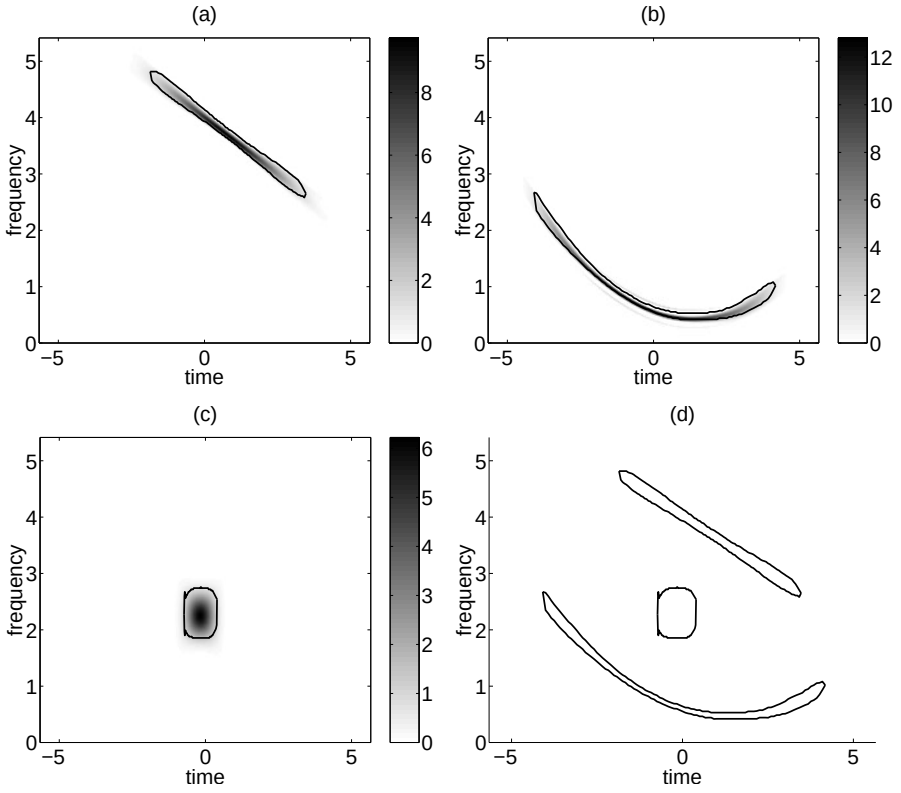


Figure 4.12: TFCA time–frequency representations of the components of the synthetic signal $x(t)$: $\hat{s_1}(t)$, $\hat{s_2}(t)$, $\hat{s_3}(t)$ are given in (a), (b) and (c), respectively, with their time–frequency supports overlaid. In (d), time–frequency supports are shown together.

the snake and the image pixels, the snake lies on. The convergence of the algorithm depends on the initial contour and energy coefficients. In general, energy coefficients can be experimentally determined.

The area of the time–frequency support of the individual components can also be used as a statistical descriptor. Areas obtained for the estimated components of the synthetic signal are available in Table 4.1.

Other statistical descriptors that distinguishes components from each other such as instantaneous frequency can be obtained from the extracted TFCA components as well.

# Chapter 5

# Results Obtained on Real ERP Signals

A Matlab graphical user interface (GUI) is designed to perform the proposed TFCA based ERP signal analysis technique on real ERP signals recorded by the Cognitive Psychophysiology Research Unit of Hacettepe University. In this section, following the introduction of the GUI, the results of the TFCA based ERP analysis are presented. Some of the obtained results are compared with those provided by the classical ERP analysis techniques (Chapter 3) as well.

## 5.1 Graphical User Interface

To be able to apply the TFCA technique on the real ERP signals, a user friendly graphical user interface is designed using Matlab. Screen shot of this

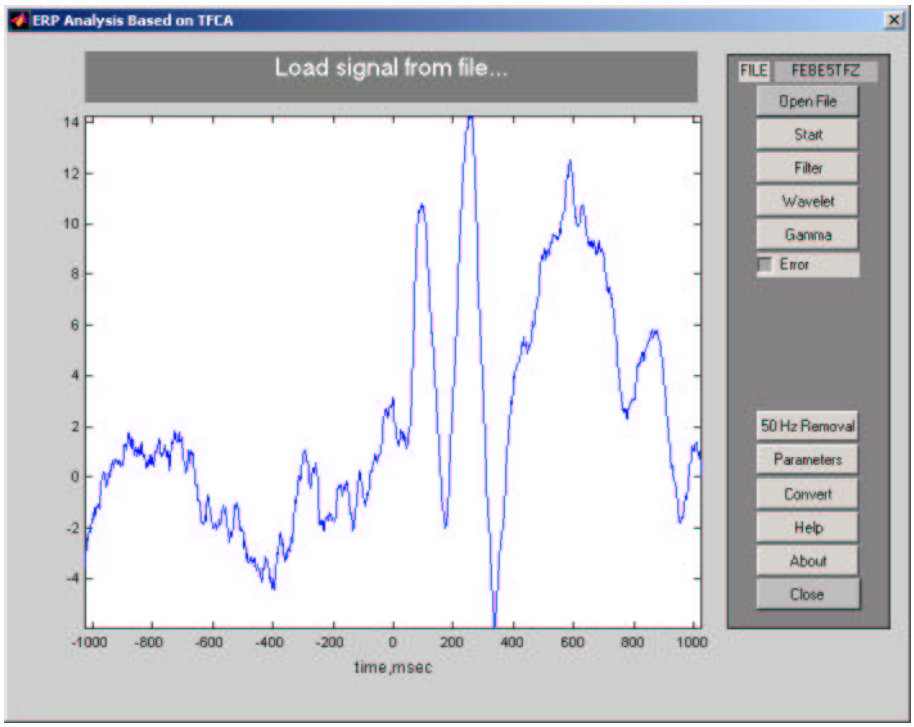


Figure 5.1: Main screen of the user friendly GUI designed for the TFCA based ERP signal analysis.

GUI, which is currently used in the Cognitive Psychophysiology Research Unit of Hacettepe University, is available in Fig. 5.1.

By means of the developed GUI, the ERP analysis based on the TFCA has gained the following functionalities:

- ERP signals to be analyzed can be selected interactively.
- Conventional analysis techniques such as digital filtering and wavelet based analysis can be conducted on the selected ERP signals. The frequency supports of the EROs are determined from the AFC interactively as shown in Fig. 5.2.

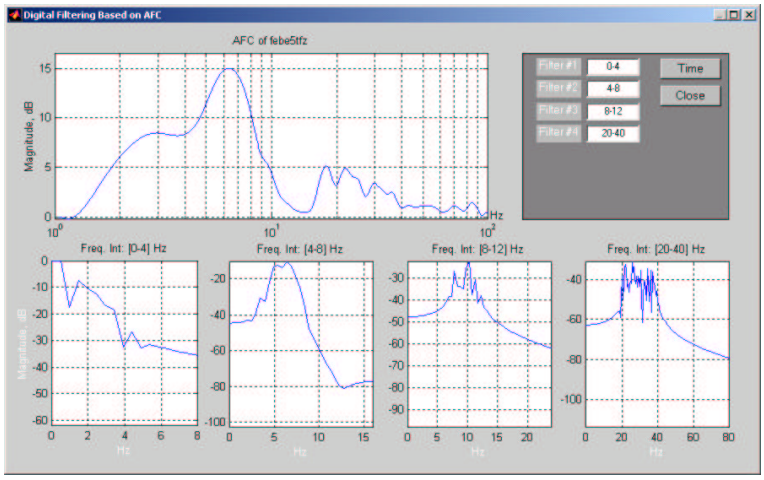


Figure 5.2: Frequency support determination of the EROs from the GUI by using the AFC.

- Time–frequency support and the spine of the components are determined on the WD plane by the user.
- In case of any error, the program returns to the beginning of the analysis of the component.
- 50 Hz line signal contamination is removed interactively where the contamination free averaged signals are produced as well as shown in Fig. 5.3 (a).
- Signal specific parameters such as length and sampling frequency can be changed as shown in Fig. 5.3 (b).
- Display parameters can be determined by the user as shown in Fig. 5.3 (b).
- Any signal whose time–frequency support is determined interactively by the user can be extracted from the ERP signal.

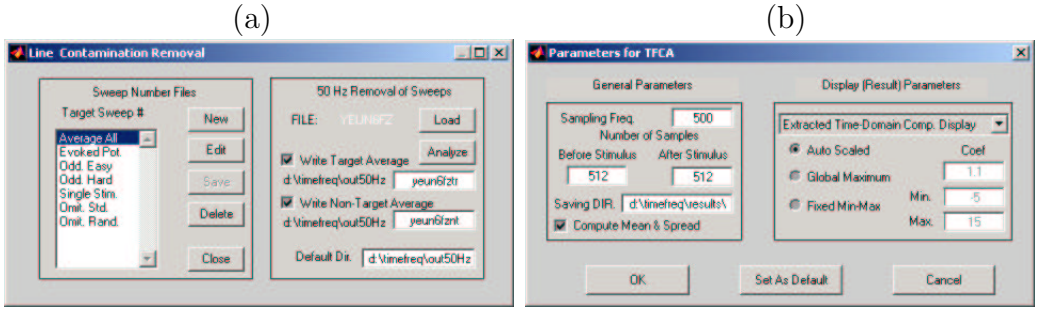


Figure 5.3: Line signal contamination removal window (a) and parameter window (b).

- The time–domain extracted components of the TFCA and conventional analysis based techniques are written to text files for possible further usage.

The developed GUI has made possible the application of the TFCA to the ERP signals.

## 5.2 OB-ES Paradigm Results

The results of the conventional analysis techniques of the target and nontarget average frames for 'FEBE' signals under OB-ES paradigm were given in Section 3.1 and Section 3.2. In this section, the detailed TFCA based analysis of these ERP signals are presented. The results are compared to those of the conventional analysis techniques as well.

The WD of the averaged target frame of 'FEBE' is shown in Fig. 5.4 (a) where the cross terms significantly cluttered the actual components resulting in a low quality description. The time–frequency representations of the components obtained from the TFCA based analysis of the averaged target frame

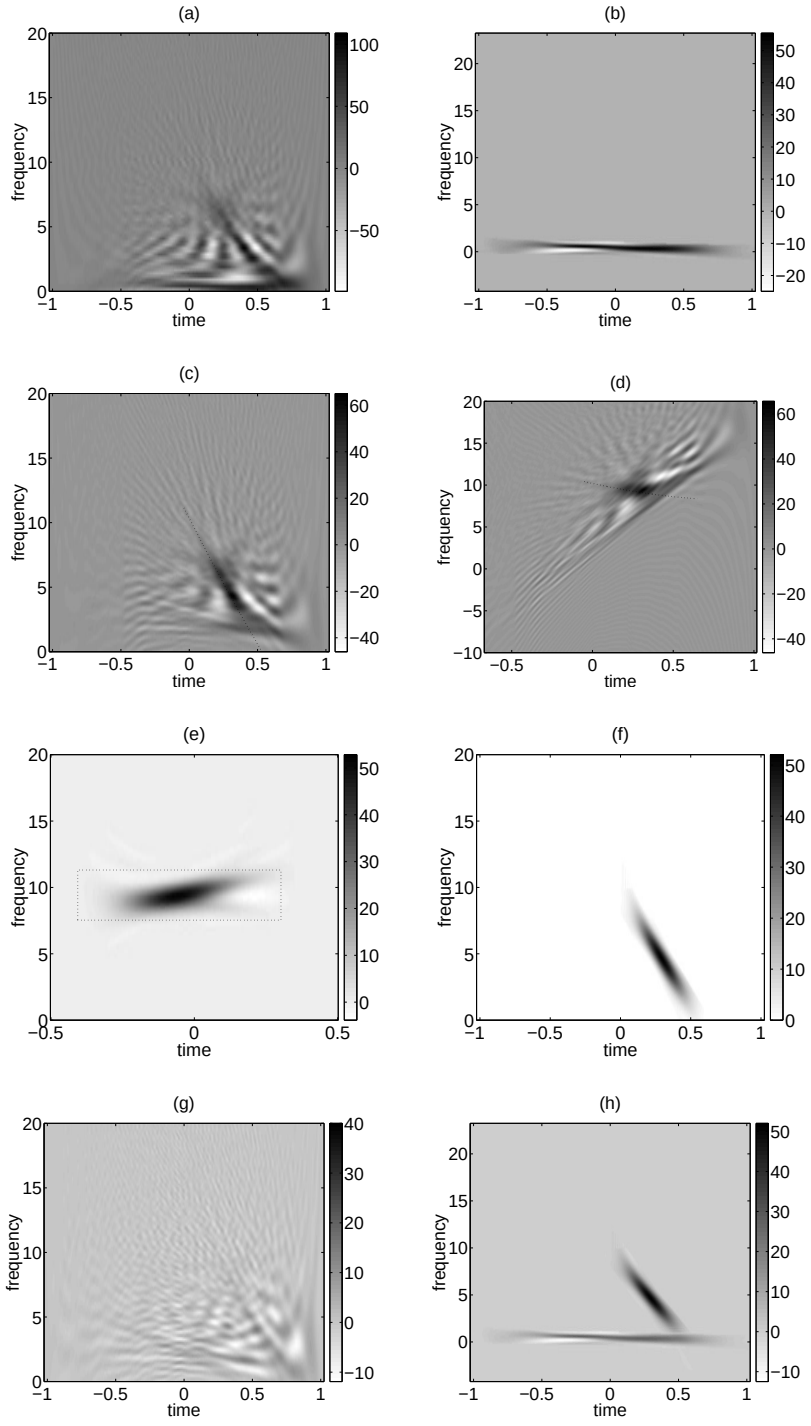


Figure 5.4: The WD of the averaged target frame shown in (a) is contaminated by the existence of cross terms. After the extraction of the first component (b), the steps of the extraction of the second component are shown in (c)-(f). (g) is the residual WD and (h) is the time–frequency representation obtained by TFCA.

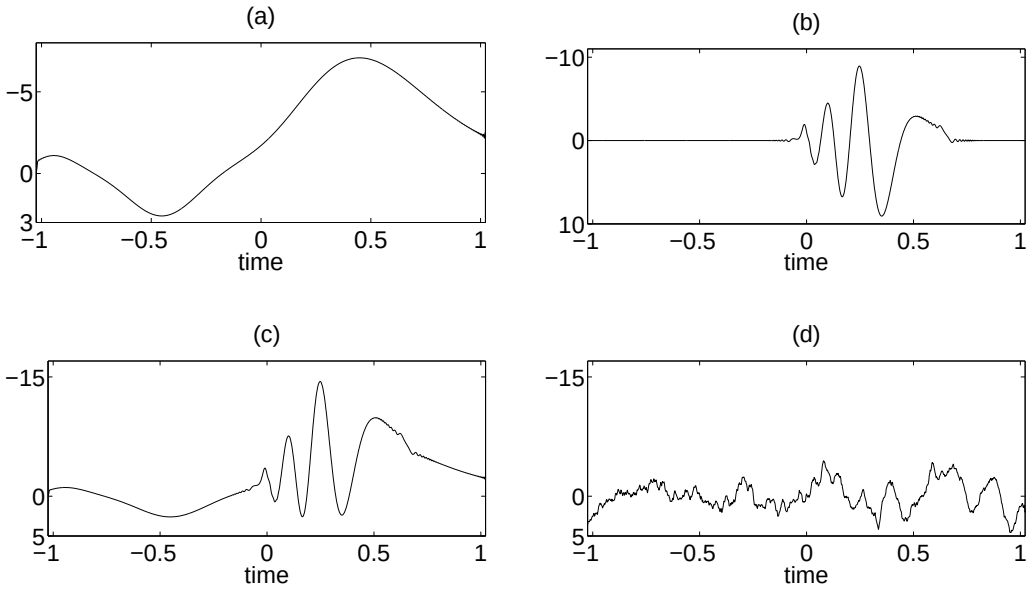


Figure 5.5: TFCA extracted time–domain components of the averaged target frame of 'FEBE' are given in (a) and (b) respectively, with their sum in (c). The residual signal in (d) is noise like.

are shown in Fig. 5.4 (b) and (f). Fig. 5.4 (c) contains the WD of the residual signal after the first component is extracted with the spine drawn as an overlay. Warping operation is performed on the rotated WD with the rotated spine given in Fig. 5.4 (d). Time–frequency mask for the resultant warped second component is shown in (e). After the extraction of the two components, the WD of the residual signal is noise like (g). For the target frame, the intermediate steps of the TFCA algorithm are shown only for the second component. For the sake of brevity, these intermediate steps of the TFCA based ERP analysis will not be presented in the analysis of the remaining data.

The TFCA algorithm provides not only very clean and sharp time-frequency characterization of the two ERP signal components as shown in Fig. 5.4 (b) and Fig. 5.4 (f) respectively, but also it extracts these components from the averaged target frame as shown in Fig. 5.5 (a) and Fig. 5.5 (b). Furthermore,

the TFCA provides the clean and sharp composite time-frequency distribution shown in Fig. 5.4 (h). The residual time–domain signal of the TFCA based analysis of the target ERP signal can be observed in Fig. 5.5 (d).

The results of the TFCA based ERP analysis on the averaged nontarget frame for the test subject 'FEBE' are shown in Fig. 5.6. The original WD shown in Fig. 5.6 (a) contains cross–term interference. The time–frequency representations of the two components provided by TFCA are given in Fig. 5.6 (b) and (d), respectively. Extracted time–domain components for the nontarget averaged frame are shown in Fig. 5.7 (a) and (b). As seen in Fig. 5.5 (d) and Fig. 5.7 (d), once the components obtained from the TFCA are subtracted from the averaged target and nontarget frames, the resultant residual signals become noise like as they should be. This observation is also supported by the computed WDs of the residual signals shown in Fig. 5.4 (g) and 5.6 (e).

Comparison of the target and nontarget results shown in Fig. 5.4 and Fig. 5.6 respectively, clearly demonstrates the differences of the ERP responses under these two different cases. Although both frames consist of two individual signal components, both the time–frequency representations and the configuration of the components are significantly different. These findings can be clearly seen by comparing the composite time–frequency representations shown in Fig. 5.4(h) and Fig. 5.6(f) respectively and the time–frequency supports of the components shown in Fig. 5.8. Especially the difference in the time–frequency representations of the stimulus related second components for the target (Fig. 5.4 (f)) and nontarget (Fig. 5.6 (d)) cases is obvious.

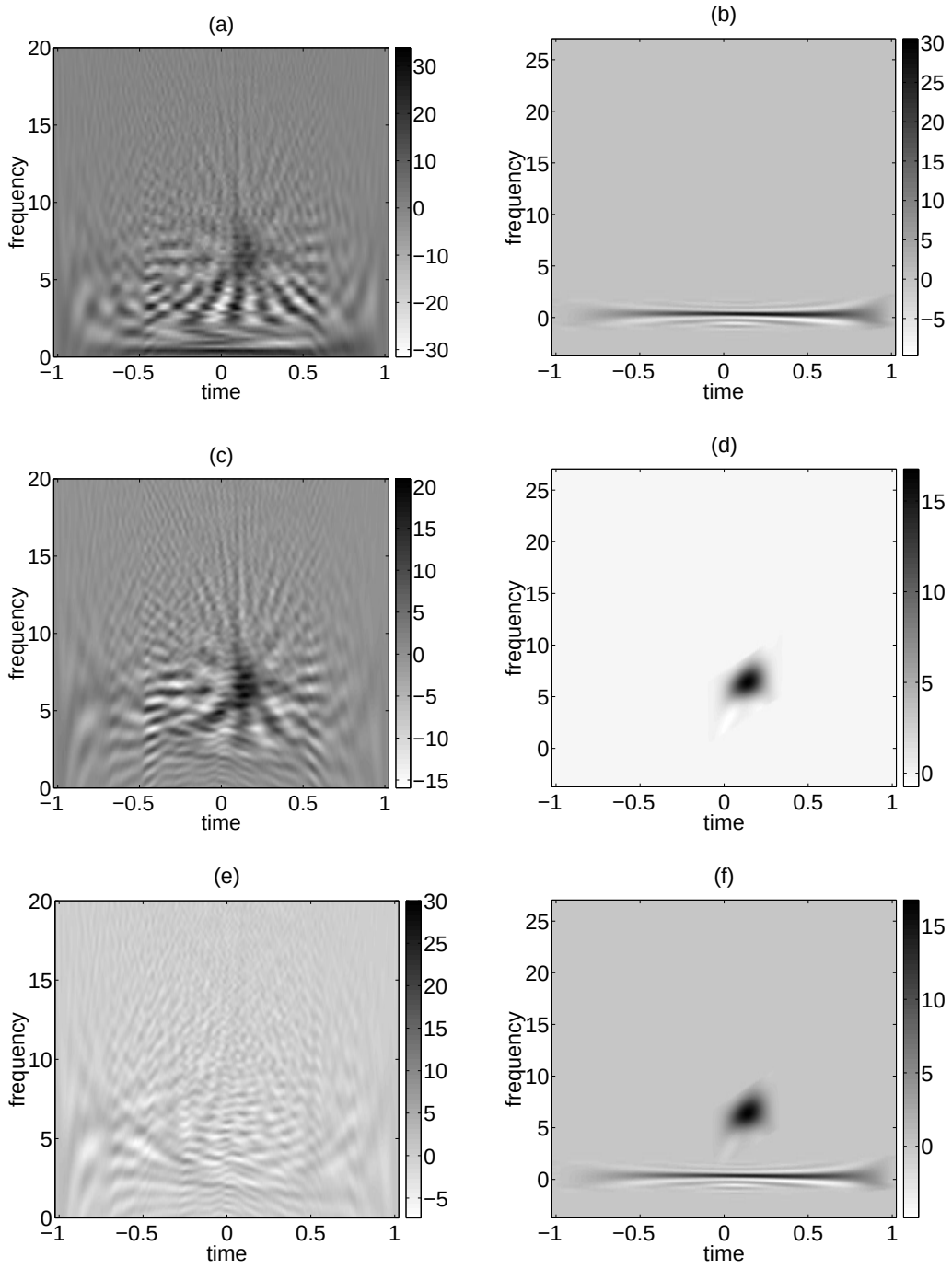


Figure 5.6: The WD of the averaged nontarget frame shown in (a) is contaminated by the existence of cross–terms. After the extraction of the first component (b), the residual WD becomes (c). Once the second component shown in (d) is also extracted by TFCA, final residual WD becomes noise like as shown in (e). The composite time–frequency representation of the averaged nontarget frame (f) is a high resolution one.

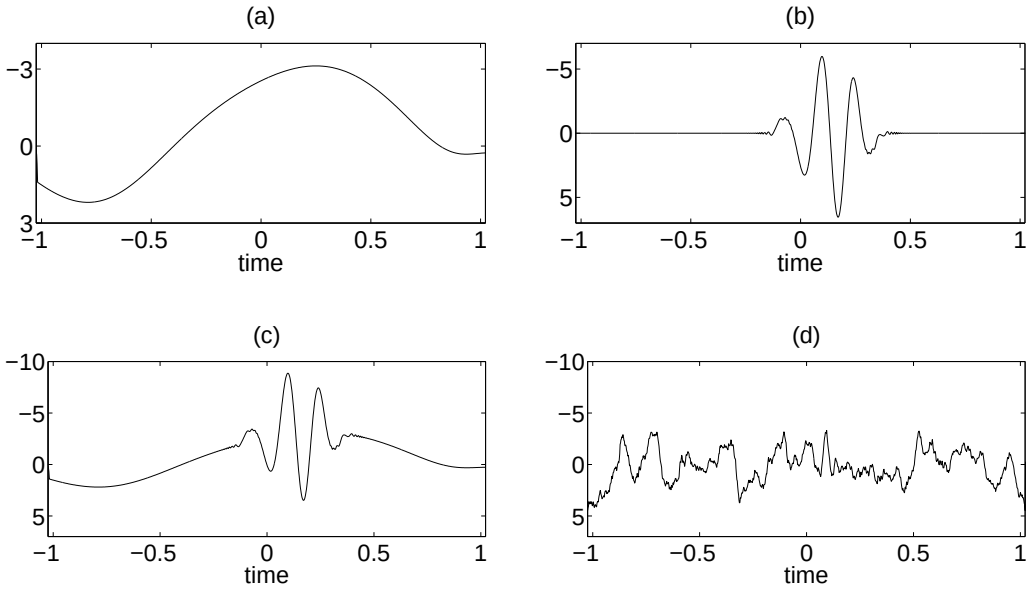


Figure 5.7: TFCA extracted time–domain components of the averaged nontarget frame of 'FEBE' are given in (a) and (b) respectively, with their sum in (c) and the residual signal in (d).

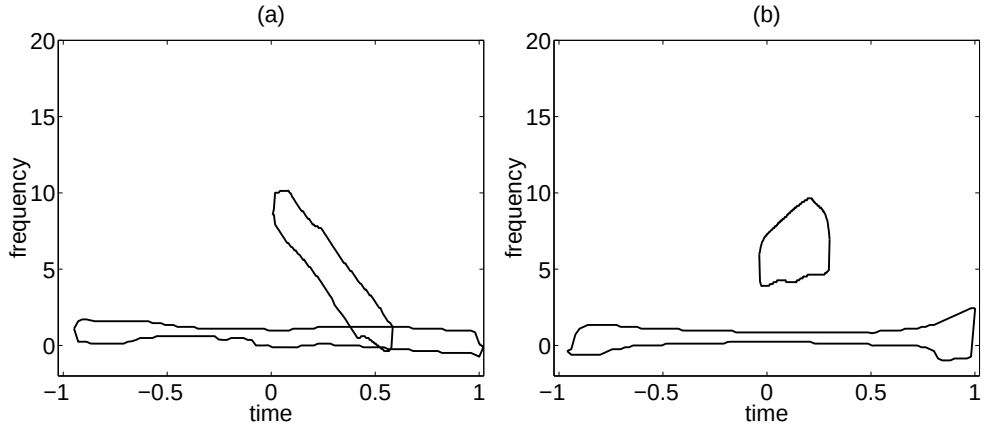


Figure 5.8: Time-frequency supports of the extracted target (a) and nontarget (b) components for 'FEBE'.

| | Target | | Nontarget | |
|---|---|---|---|---|
| Comp # | 1 | 2 | 1 | 2 |
| $t_m$ (msec) | 261 | 286 | 181 | 138 |
| $t_v$ (msec) | 383 | 104 | 504 | 75 |
| $f_m$ (Hz) | .41 | 4.8 | .22 | 6.3 |
| $f_v$ (Hz) | .22 | 2 | .52 | 1.2 |
| $area$ | 2.225 | 1.776 | 2.24 | 1.395 |

Table 5.1: Time center ($t_m$), frequency center ($f_m$), time spread ($t_v$), frequency spread ($f_v$) and area of the time–frequency support of the extracted components of the target and nontarget 'FEBE' frames.

Estimated time–frequency center and spread of the components for the target and nontarget frames are given in Table 5.1 with the area of their time–frequency supports. These estimated statistical descriptors differ for target and nontarget frames. The ability to clearly differentiate the responses corresponding to the target and nontarget cases is a very important property of the TFCA based ERP signal analysis.

Wigner distributions of the wavelet reconstructed target frame for the approximate frequency bands [4-8] Hz and [0.5-4] Hz are shown in Fig. 5.9 (a) and (b), respectively. When compared with the TFCA result for the second ERP component given in Fig. 5.4 (f), it can be seen that the wavelet based analysis could not isolate the second ERP component as a single entity. In the wavelet based analysis the higher frequency part of the second ERP component is captured as part of the theta signal, and the lower frequency part of the second ERP component is captured as part of the delta signal. Similarly, for the digital filtering based analysis shown in Fig. 5.9 (c) and (d), the lower frequency part of the second ERP component in the frequency band [0.1-3.9] Hz is captured as part of the delta signal, and the higher frequency part of the second ERP

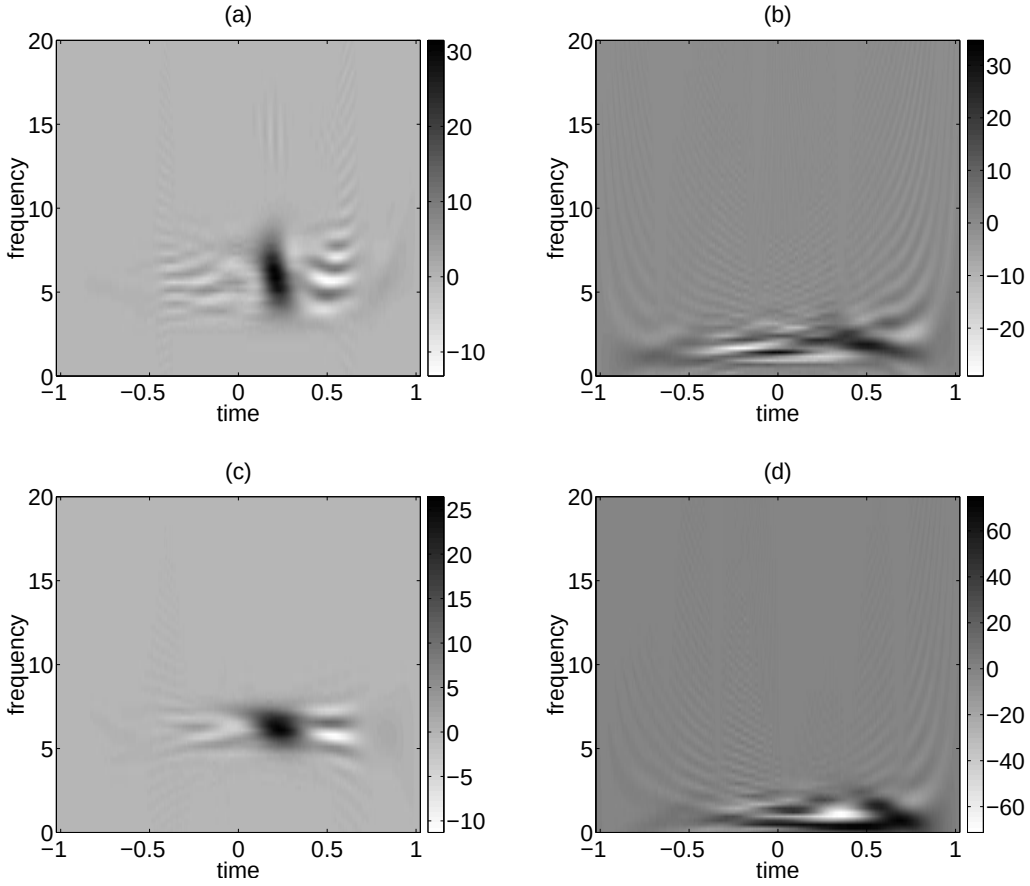


Figure 5.9: As shown in the WDs of the wavelet reconstructed signals of the target frame for the [4-8] Hz band (a) and for the [0.5-4] Hz band (b), the wavelet based analysis splits the second ERP component obtained by the TFCA ( shown in Fig. 5.4(f) ) into the delta and theta signals, respectively. The WDs of the digital filtered target frame for the frequency bands of [4-9] and [0.1-3.9] Hz shown in (c) and (d), similarly reveal that part of the second ERP component is captured by the theta signal and part of it by the delta signal.

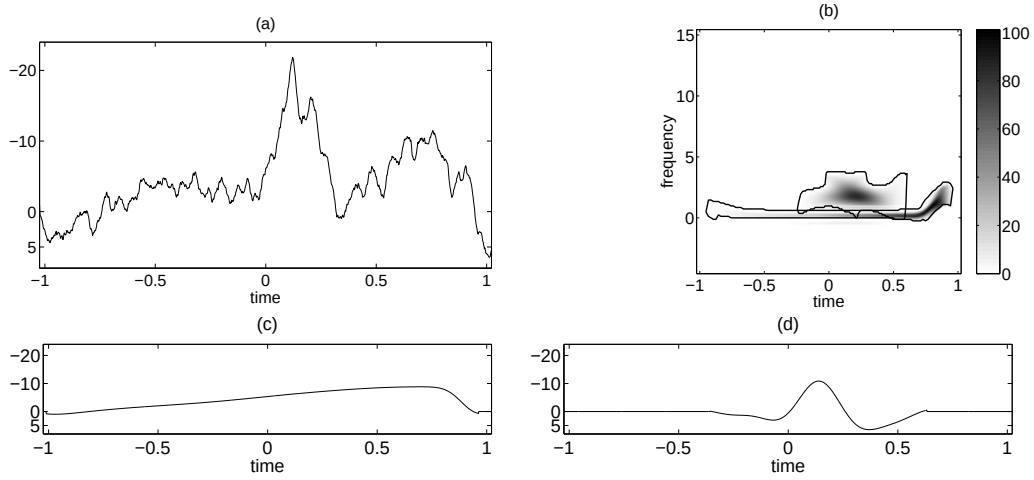


Figure 5.10: Original average target ERP signal (a), composite time–frequency representation obtained by TFCA (b) and estimated individual time–domain components (c) and (d) for the test subject 'EMYI'.

component in the frequency band [4-9] Hz is captured as part of the theta signal. Moreover in both methods, the theta and delta signals are contaminated by the existence of noise at all times. The provided results demonstrate clearly that the wavelet and digital filtering (DF) based ERP analysis fails to isolate the existing ERP components, and fails to extract them from the averaged target and nontarget frames. Furthermore, the obtained time–frequency representations of the wavelet and DF based analysis are not as clean and sharp as the ones provided by the TFCA.

### 5.2.1 Results for Different Test Subjects

Cognitive psychophysiology studies the test subject and paradigm specific morphology of the ERP signals [5, 13, 34]. To investigate the variability of the obtained results with respect to test subjects, the ERP signals of test subjects

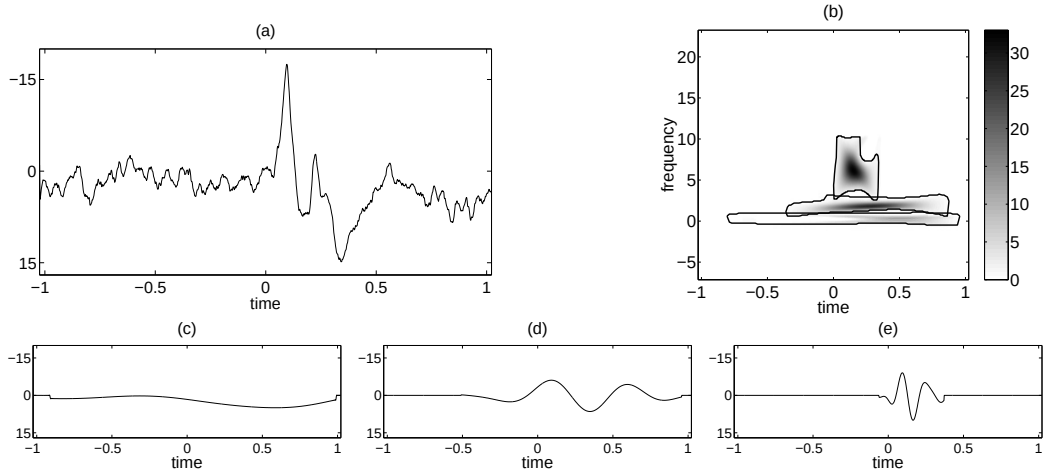


Figure 5.11: Original average target ERP signal (a), composite time–frequency representation obtained by TFCA (b) and extracted individual time–domain components (c), (d) and (e) for the test subject 'ORGU'.

'EMYI', 'ORGU', 'OZBE' and 'TATA' recorded under the OB-ES paradigm are analyzed by the TFCA based ERP analysis technique.

The original averaged target ERP signals for the mentioned test subjects are shown in Figures 5.10-5.13 (a). The time–frequency representations of these averaged target signals obtained from TFCA are given in Figures 5.10-5.13 (b) with their time–frequency supports overlaid. The time–frequency representations of each test subject are different from each other. Figure 5.10 (c) and (d) contains the estimated time–domain components for 'TATA'. In the Figures 5.11 to 5.13 (c), (d) and (e), estimated three time–domain components for 'ORGU', 'OZBE' and 'TATA' are shown respectively.

The second component for 'EMYI' and the third components for the other test subjects are related to the stimuli, therefore they have no pre–stimulus response. On the other hand the EROs obtained from conventional analysis techniques contains not only post–stimulus but also pre–stimulus activation.

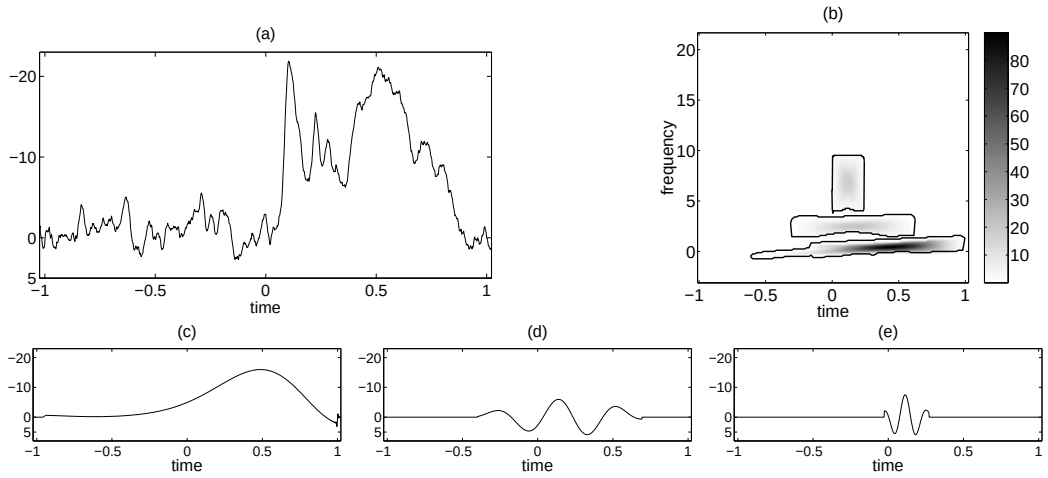


Figure 5.12: Original average target ERP signal (a), time–frequency representation obtained by TFCA (b) and estimated individual time–domain components (c), (d) and (e) for the test subject 'OZBE'.

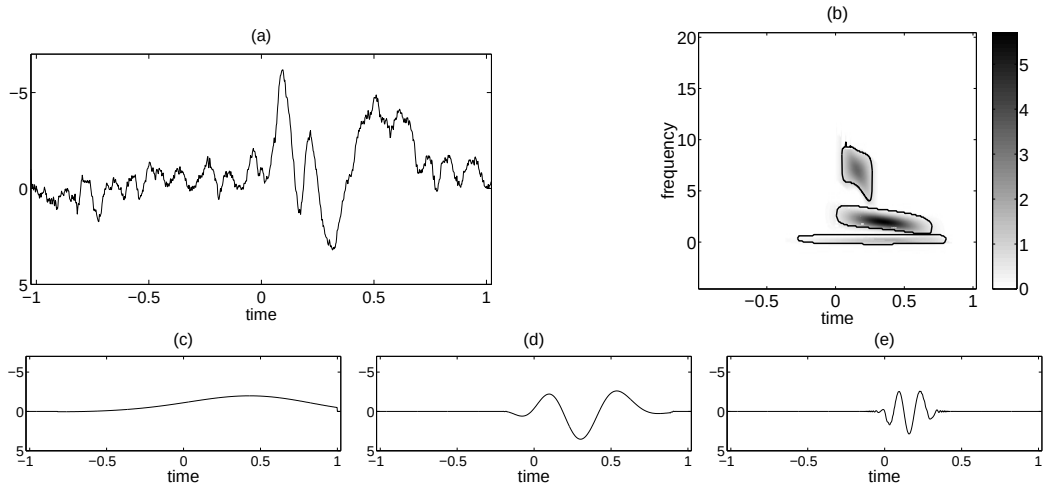


Figure 5.13: Original average target ERP signal (a), time–frequency representation obtained by TFCA (b) and estimated individual time–domain components (c), (d) and (e) for the test subject 'TATA'.

| | 'EMYI' | | 'ORGU' | | | 'OZBE' | | | 'TATA' | | |
|---|---|---|---|---|---|---|---|---|---|---|---|
| Comp # | 1 | 2 | 1 | 2 | 3 | 1 | 2 | 3 | 1 | 2 | 3 |
| $t_m$ (msec) | 468 | 204 | 351 | 275 | 156 | 416 | 178 | 118 | 303 | 347 | 160 |
| $t_v$ (msec) | 415 | 152 | 350 | 249 | 70 | 271 | 200 | 55 | 265 | 170 | 65 |
| $f_m$ (Hz) | .56 | 1.8 | .17 | 1.8 | 6.2 | .36 | 2.4 | 6.8 | .13 | 2 | 6.8 |
| $f_v$ (Hz) | .68 | .67 | .32 | .41 | 1.5 | .32 | .42 | 1.3 | .2 | .57 | 1.3 |
| $area$ | 1.64 | 2.21 | 2.30 | 2.13 | 1.90 | 1.94 | 1.74 | 1.29 | 0.91 | 1.24 | 0.80 |

Table 5.2: Time–frequency center, time spread and frequency spread of the components obtained from the ERP signals of the test subjects under OB-ES paradigm.

Instead of analyzing the amplitudes and latencies of the peaks to the stimulus as done in conventional analysis techniques, computed statistical descriptors given in Table 5.2 can be used in clinical studies. The statistical descriptors for each estimated component differs with respect to test subjects.

## 5.3 Results for Ensemble Averages

The time–frequency representations of the ensemble averages of the test subjects under MMN and OB-HD paradigms obtained by the TFCA are studied in this thesis as well. Ensemble averages are obtained by averaging the responses of the individual test subjects.

Ensemble target average signal under MMN is shown in Fig. 5.14 (a) while that of the nontarget signal in Fig. 5.15 (a). The ensemble target average under OB-HD is also available in Fig. 5.16 (a). The time–frequency representations obtained by TFCA are shown in Figures 5.14-5.16 (b) with the time–frequency supports overlaid. The estimated time–domain components are also given in the figures.

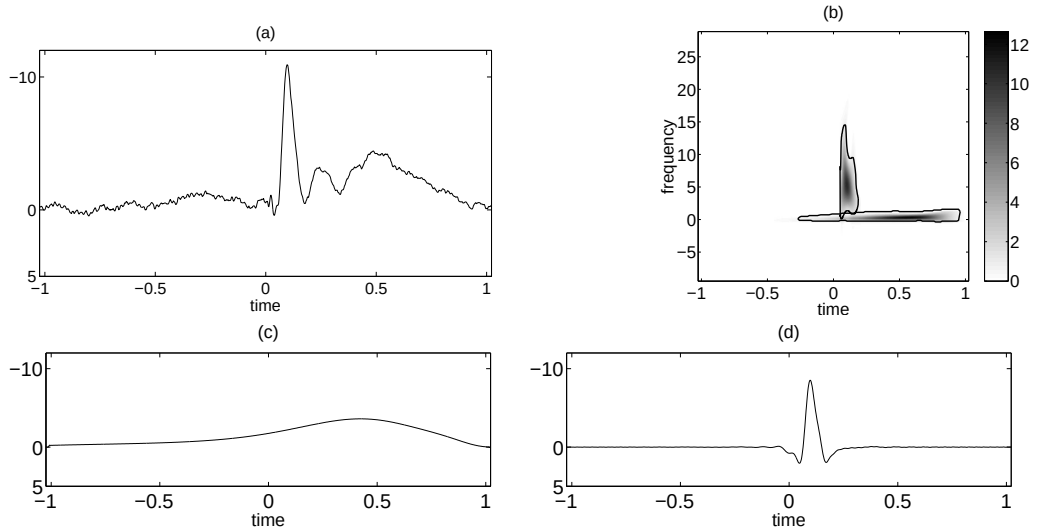


Figure 5.14: Original ERP signal (a), time–frequency representation obtained by TFCA (b) and estimated individual time–domain components (c) and (d) for the ensemble target average under MMN paradigm.

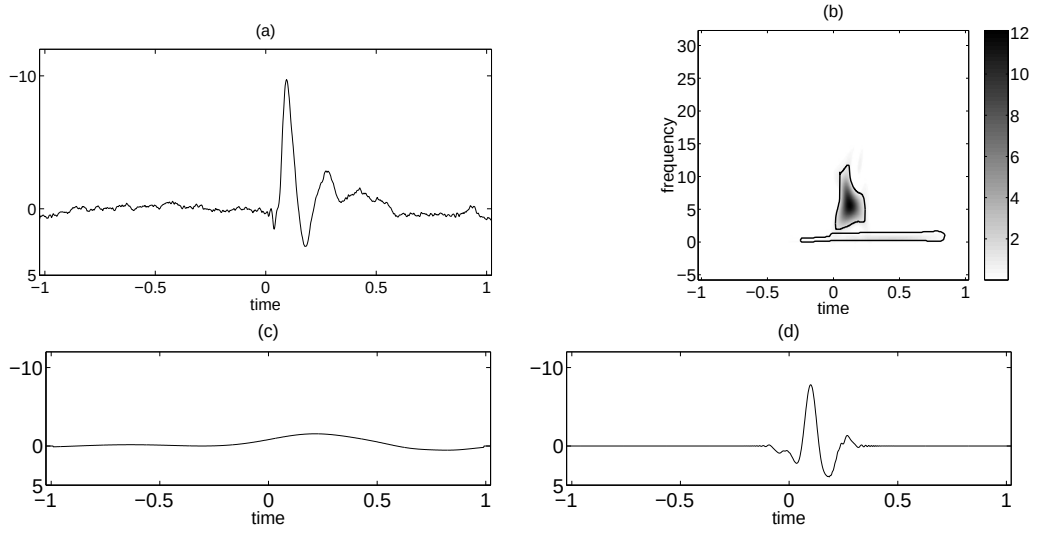


Figure 5.15: Original ERP signal (a), time–frequency representation obtained by TFCA (b) and estimated individual time–domain components (c) and (d) for the ensemble nontarget average under MMN paradigm.

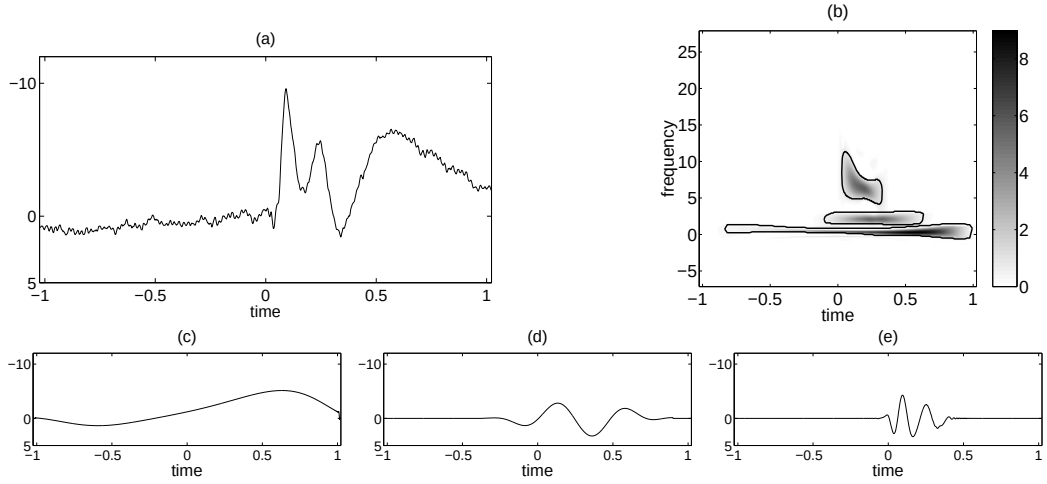


Figure 5.16: Original ERP signal (a), time–frequency representation obtained by TFCA (b) and estimated time–domain components (c), (d) and (e) for the ensemble target average under OB-HD paradigm.

The estimated statistical descriptors of the TFCA components obtained for the ensemble averaged ERP signals are given in Table 5.3.

Time–frequency distributions provided by the TFCA differ from each other for different test subjects and paradigms. Especially the stimulus related second component can be easily distinguished. Time–frequency supports and the estimated statistical descriptors for the OB-ES given in Section 5.2.1, and those for the ensemble averaged OB-HD and MMN cases support our observations.

| | MMN Target | | MMN Nontarget | | OB-HD Nontarget | | |
|---|---|---|---|---|---|---|---|
| Comp # | 1 | 2 | 1 | 2 | 1 | 2 | 3 |
| $t_m$ (msec) | 485 | 105 | 330 | 120 | 392 | 278 | 165 |
| $t_v$ (msec) | 272 | 31 | 306 | 54 | 404 | 178 | 84 |
| $f_m$ (Hz) | .31 | 5.8 | .53 | 5.9 | .34 | 2.1 | 6.8 |
| $f_v$ (Hz) | .35 | 3.4 | .36 | 2.5 | .36 | .4 | 1.9 |
| $area$ | 1.63 | 1.23 | 1.20 | 1.33 | 1.91 | 1.17 | 1.13 |

Table 5.3: Time–frequency center, time spread and frequency spread of the components obtained from the ERP signals for the ensemble average of the test subjects under MMN and OB-HD paradigms.

The difference in the structure of the time–frequency representations obtained by TFCA with respect to test subjects and paradigms is the most powerful feature of the TFCA based ERP signal analysis.

## 5.4 Variability in a Single Test Subject

Having observed that test subjects produce different time–frequency representations in the TFCA, we want to analyze the averages of different sweeps of the same test subject. Since the sweeps of the ERP signals are very noisy, the number of the artifact–free target sweeps (i.e., 20) is not adequate for this analysis, whereas the number of the nontarget sweeps (i.e., 100) is. For this purpose the TFCA results of the averages of the odd and even numbered nontarget sweeps shown in Fig. 5.17 (a) of the test subject 'YEUN' are compared to each other. As shown in Fig. 5.17 (b) and (c) for the odd and even numbered averages respectively, the time–frequency representations provided by TFCA for the two cases are similar to each other except for the low–frequency first component.

Since the behavior and biological state of the test subject may change during recording, difference in between the low–frequency first components is expected. As the statistical descriptors given in Table 5.4 and the overlaid time–frequency supports shown in Fig. 5.17 (d) indicate, the difference between the stimulus related second component of the two is negligible as expected.

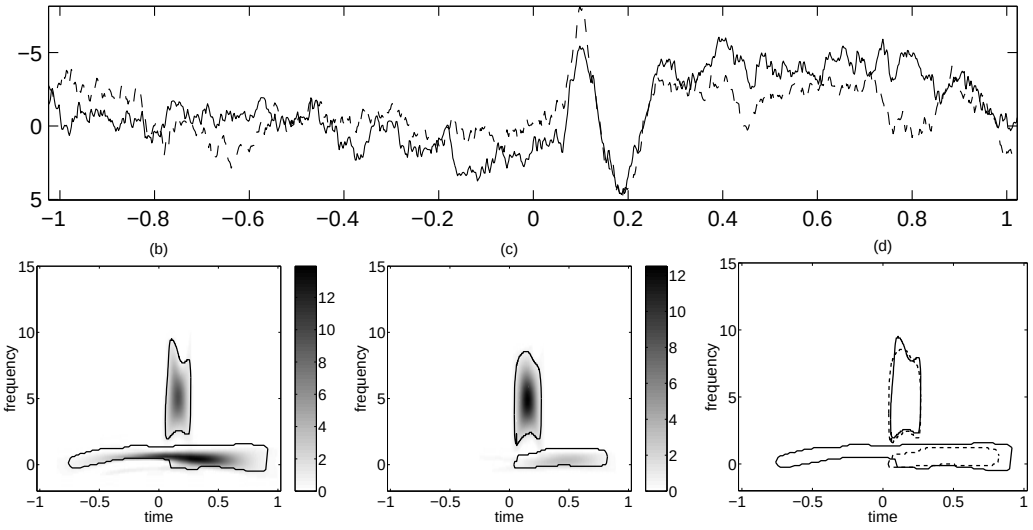


Figure 5.17: TFCA results of the averages of the odd and even numbered sweeps of 'YEUN'. In (a), the dashed line shows the even numbered sweeps' average, and solid line the odd numbered. (b) and (c) contain the time–frequency representations provided by TFCA for the odd and even numbered sweep averages, respectively, while (d) the overlaid time–frequency supports of the two cases.

| | Odd | | Even | |
|---|---|---|---|---|
| Comp # | 1 | 2 | 1 | 2 |
| $t_m$ (msec) | 423.5 | 151.2 | 219.3 | 159.5 |
| $t_v$ (msec) | 247.5 | 54.6 | 355 | 53.6 |
| $f_m$ (Hz) | .36 | 4.9 | .48 | 5.2 |
| $f_v$ (Hz) | .35 | 1.5 | .41 | 1.7 |
| $area$ | .9275 | 1.298 | 2.246 | 1.212 |

Table 5.4: Statistical descriptors for the averages of odd and even numbered nontarget sweeps of 'YEUN'.

# Chapter 6

# CONCLUSIONS

In this thesis, a new ERP analysis technique based on Time–Frequency Component Analyzer (TFCA) [30] is proposed. The TFCA makes use of a novel fractional domain warping concept to provide very high resolution time–frequency representations of the individual ERP components. TFCA not only provides the cross–term free time–frequency distributions of the components but also extracts their highly accurate time–domain estimates from the multi–component ERP signal. Statistical parameters obtained from the time–frequency distributions of the components provide robust, quantative and objective information about the ERP signals, thus the test subjects, which may be used in clinical studies.

Since ERP signals are non–stationary composite signals, conventional analysis techniques which uses only time or frequency domain methods are not suited to their analyses. Unlike the conventional analyses, the TFCA is able to capture the localized time–frequency support of the ERP signals. Whereas,

wavelet and digital filtering based analysis techniques often split the individual components of the ERP signals into two or more oscillatory signals with nonoverlapping frequency supports. Furthermore the TFCA also provides reliable estimates to the individual ERP signal components.

Neither the time–domain description based on the peaks of the ERP signal, nor the frequency–domain description based on the digital filtering can capture the true nature of the existing components of the ERP signals. The TFCA works on the time–frequency domain to capture the non–stationary nature of the ERP components. Unlike the results obtained by using conventional ERP analysis techniques, the poststimulus response obtained in TFCA does not contain a prestimulus activation.

Conventional analysis techniques tries to extract information from the ERP signals based on the amplitudes and latencies of the peaks in the signal. ERP analysis based on the TFCA replaces this kind of analysis scheme with either the visual study of the time–frequency representations provided by TFCA or the quantitative comparison of the statistical descriptors obtained from the extracted individual components of the ERP signals.

Not only the time–frequency representations but also the statistical descriptors obtained by the TFCA differs with respect to test subjects and paradigms which is the most powerful feature of the TFCA based ERP signal analysis. This feature may be used in the evaluation of the brain function, brain-behavior relationships, impairments in cognitive functioning in psychiatric disorders and ERP-drug interaction.

The TFCA provides very similar results for the averages of different sweeps of the same test subject which indicates the conformity of the TFCA based ERP results.

In conclusion, the TFCA does not have a precedent in resolution and extraction of the individual components of the ERP signal components. The TFCA based ERP signal anaylsis technique may thus be regarded as an ideal tool for studying the intricate machinery of the human brain.

Future work on the ERP analysis can be focused on the spatial analysis of the recordings from various sites of the electro–cap system. Automatic identification of the time–frequency support and spine of the signal components in TFCA requires further research as well.

The TFCA can be adapted not only to ERP signal analysis as it is done in this thesis, but also to the analysis of other biomedical signals, especially those where a stimulus is applied to the underlying biological subject, such as myoelectric signals, electrocardiogram (ECG) and magnetoencephalogram (MEG).

# Bibliography


[1] E. Başar, *Brain Function and Oscillations*, vol. 1. Heidelberg: Springer-Verlag, 1998.

[2] S. Grossberg, *The Adaptive Brain.* Amsterdam: North Holland, 1987.

[3] T. H. Bullock, *Induced Rhythms in the Brain*, ch. Introduction to induced rhythms: a widespread, heterogeneous class of oscillations, pp. 1–26. Boston: Birkhauser, 1992.

[4] C. Pantev, B. Ltkenhner, and T. Elbert, eds., *Oscillatory Event Related Brain Dynamics.* New York-London: Plenum Press, 1994.

[5] S. Karakaş, U. O. Erzengin, and E. Başar, "A new strategy involving multiple cognitive paradigms demonstrates that ERP components are determined by the superposition of oscillatory responses," *Clinical Neurophysiology*, vol. 111, pp. 1719–1732, 2000.

[6] S. L. Bressler, "The gamma wave: a cortical information carrier?," *Trends in Neurosciences*, vol. 13, no. 5, pp. 161–162, 1990.

[7] S. Karakaş, U. O. Erzengin, and E. Başar, "The genesis of human event-related responses explained through the theory of oscillatory neural assemblies," *Neuroscience Letters*, vol. 285, pp. 45–48, 2000.

[8] E. Başar, C. Başar-Eroğlu, T. Demiralp, and M. Schürmann, "Oscillatory brain theory: A new trend in neuroscience," *IEEE Eng. in Medicine and Biology*, pp. 56–66, May/June 1999.

[9] E. Başar, C. Başar-Eroğlu, S. Karakaş, and M. Schürmann, "Gamma, alpha, delta, and theta oscillations govern cognitive processes," *International Journal of Psychophysiology*, vol. 39, pp. 241–248, 2001.

[10] E. Başar, C. Başar-Eroğlu, T. Demiralp, and M. Schürmann, "Time and Frequency Analysis of the Brain's Distributed Gamma–Band System," *IEEE Eng. in Medicine and Biology*, Jul/Aug 1995.

[11] J. S. Barlow, ed., *The Electroencephalogram: Its patterns and origins*. Cambridge-London: MIT Press, 1993.

[12] E. Donchin and M. G. H. Coles, "Is the P300 component a manifestation of context updating?," *Brain and Behavioral Sciences*, vol. 11, pp. 357–374, 1988.

[13] R. Johnson, *Advances in psychophysiology: A research annual*, vol. 3, ch. The amplitude of the P300 component of the event-related potentials: A review and synthesis., pp. 244–266. Greenwich: JAI Press, 1988.

[14] H. J. Michalewski and D. K. Prasher, "Latency variability and temporal interrelationship of the auditory event-related potentials (n1,p2,n2, and p3) in normal subjects," *Electroencephalography and Clinical Neurophysiology*, vol. 65, no. 1, pp. 59–71, 1986.

[15] J. Polich and A. Kok, "Cognitive and biological determinants of P300: An integrative review," *Biological Psychology*, vol. 41, pp. 103–146, 1995.

[16] D. G. Childers, N. W. Perry, I. A. Fischler, T. Boaz, and A. A. Arroyo, "Event-related potentials: A critical review of methods for single-trial detection," *Crit. Rev. Biomed. Eng.*, vol. 14, no. 3, pp. 185–200, 1987.

[17] J. Möcks and R. Verleger, "Principal component analysis of event-related potentials: A note on misallocation of variance," *Electroencephalography and Clinical Neurophysiology*, vol. 65, pp. 393–398, 1986.

[18] J. Möcks and R. Verleger, *Digital Biosignal Processing*, ch. Multivariate methods in biosignal analysis: application of principal component analysis to event-related potentials, pp. 399–458. Amsterdam: Elsevier, 1991.

[19] R. L. Horst and E. Donchin, "Beyond averaging. II. Single-trial classification of exogenous event-related potentials using stepwise discriminant analysis," *Electroencephalography and Clinical Neurophysiology*, vol. 48, no. 2, pp. 113–126, 1980.

[20] H. Utku, O. U. Erzengin, E. D. Çakmak, and S. Karakaş, "Discrimination of brain's neuroelectric responses by a decision-making function," *Journal of Neuroscience Methods*, vol. 114, pp. 25–31, 2002.

[21] G. V. Hoey, W. Philips, and I. Lemahieu, "Time–frequency analysis of eeg signals," *Proc. of the ProRISC Workshop on Circuits, Systems and Signal Process.*, pp. 549–553, 1997.

[22] E. Başar, *Brain Function and Oscillations*, vol. 2. Heidelberg: Springer-Verlag, 1998.

[23] V. J. Samar, M. R. Raghuveer, K. P. Swartz, S. Rosenberg, and T. Chaiyaboonthanit, "Wavelet decomposition of event related potentials: toward

the definition of biologically natural components," *IEEE Sixth SP Workshop on Statistical Signal and Array Processing*, pp. 38–41, Oct. 1992.

[24] H. Heinrich, H. Dickhaus, A. Rothenberger, V. Heinrich, and G. H. Moll, "Single-sweep analysis of event-related potentials by wavelet networks-methodological basis and clinical application," *IEEE Trans. Biomed. Eng.*, vol. 46, pp. 867–879, July 1999.

[25] R. E. Herrera, R. J. Sclabassi, S. Mingui, R. E. Dahl, and N. D. Ryan, "Single trial visual event-related potential EEG analysis using the wavelet transform," *Proc. of the 16th Conf. of the IEEE on Eng. in Medicine and Biology Society*, vol. 1, pp. 191–192, Nov. 1994.

[26] R. Q. Quiroga, Q. W. Sakowitz, E. Başar, and M. Schürmann, "Wavelet transform in the analysis of the frequency composition of evoked potentials," *Brain Research Protocols*, vol. 8, pp. 16–24, 2001.

[27] S. Blanco, A. Figliola, R. Q. Quiroga, O. A. Rosso, and E. Serrano, "Time–frequency analysis of electroencephalogram series. III. Wavelet packets and information cost function," *Physical Review E*, vol. 57, no. 1, pp. 932–940, 1998.

[28] C. Dorize and K. Gram-Hansen, *Wavelets and Applications*, ch. Related Positive Time–Frequency Energy Distributions, pp. 77–85. Springer-Verlag and Masson, 1992.

[29] M. E. Tağluk, E. D. Çakmak, and S. Karakaş, "Seyrek uyarıcı paradigması altında elde edilen beyin elektriksel faaliyetinin yüksek çözünürlüklü enerji dağılımı," No. 239 in BIOMUT, (İstanbul), pp. 13–19, Boğaziçi University, May 2002.

[30] A. K. Özdemir and O. Arıkan, "Time–Frequency Component Analyzer." Submitted to *IEEE Trans. Signal Process.*, 2002.

[31] S. Karakaş, E. D. Çakmak, D. İ. Tüfekçi, A. K. Özdemir, and O. Arıkan, "A new time–frequency analysis technique for neuroelectric responses." Submitted to *IEEE Trans. Biomed. Eng.*, 2002.

[32] "http://www.nkusa.com/peeg4400.htm."

[33] W. Ritter, P. Paavilainen, J. Lavikainen, K. Reinikainen, K. Alho, M. Sams, and R. Naatanen, "Event-related potentials to repetition and change of auditory stimuli," *Electroencephalography and Clinical Neurophysiology*, vol. 83, pp. 306–321, 1992.

[34] B. W. Jervis, M. J. Nichols, T. E. Johnson, E. Allen, and N. R. Hudson, "A fundamental investigation of the composition of auditory evoked potentials," *IEEE Trans. Biomed. Eng.*, vol. 30, pp. 43–49, 1983.

[35] R. Naatanen, "The role of attention in auditory information processing as revealed by event-related potentials and other brain measures of cognitive function," *Behavioral and Brain Science*, vol. 13, no. 2, pp. 201–288, 1990.

[36] B. M. A. Sayers, H. A. Beagley, and W. R. Henshall, "The mechanism of auditory evoked EEG responses," *Nature*, vol. 247, pp. 481–483, 1974.

[37] J. Raz, "Wavelet models of event related potentials," *Proc. of the 16th Conf. of the IEEE on Eng. in Medicine and Biology Society*, vol. 1, pp. 191–192, Nov. 1994.

[38] R. Q. Quiroga, "Obtaining single stimulus evoked potentials with wavelet denoising," *Physica D*, vol. 145, pp. 278–292, May 2000.

[39] S. Mallat, "A theory for multiresolution signal decomposition: The wavelet representation," *IEEE Trans. Pattern Analysis, and Machine Intelligence*, vol. 2, no. 7, pp. 674–693, 1989.

[40] G. Strang and T. Nguyen, *Wavelets and Filter Banks*. Wellesley-Cambridge Press, 1996.

[41] A. K. Özdemir, L. Durak, and O. Arıkan, "High resolution time–frequency analysis based on fractional domain warping," *Proc. IEEE Int. Conf. Acoust. Speech Signal Process.*, vol. VI, pp. 3553–3556, May 2001.

[42] T. A. C. M. Claasen and W. F. G. Mecklenbrauker, "The Wigner distribution – A tool for time–time frequency signal analysis, Part I: Continuous–time signals," *Philips J. Res.*, vol. 35, no. 3, pp. 217–250, 1980.

[43] T. A. C. M. Claasen and W. F. G. Mecklenbrauker, "The Wigner distribution – A tool for time–time frequency signal analysis, Part II: Discrete–time signals," *Philips J. Res.*, vol. 35, no. 4/5, pp. 276–350, 1980.

[44] T. A. C. M. Claasen and W. F. G. Mecklenbrauker, "The Wigner distribution – A tool for time–time frequency signal analysis, Part III: Relations with other time–frequency signal transformations," *Philips J. Res.*, vol. 35, no. 6, pp. 372–389, 1980.

[45] L. Cohen, "Time–frequency distributions – A review," *Proc. IEEE*, vol. 77, pp. 941–981, July 1989.

[46] F. Hlawatsch and G. F. Boudreaux-Bartels, "Linear and quadratic time–frequency signal representations," *IEEE Signal Processing Magazine*, vol. 9, pp. 21–67, Apr. 1992.

[47] L. Cohen, *Time–frequency analysis*. Prentice Hall, 1995.

[48] A. K. Özdemir and O. Arıkan, "A high resolution time frequency representation with significantly reduced cross–terms," *Proc. IEEE Int. Conf. Acoust. Speech Signal Process.*, vol. II, pp. 693–696, June 2000.

[49] F. Boashash and P. J. Black, "An Efficient Real–Time Implementation of the Wigner–Ville Distribution," *IEEE Trans. Acoust., Speech, and Signal Process.*, vol. 35, pp. 1611–1618, Nov 1987.

[50] F. Peyrin and R. Prost, "A unified definition for the discrete–time, discrete–frequency, and discrete–time/frequency wigner distributions," *IEEE Trans. Acoust., Speech, and Signal Process.*, vol. 34, pp. 858–866, aug 1986.

[51] A. K. Özdemir and O. Arıkan, "Fast Computation of the Ambiguity Function and the Wigner Distribution on Arbitrary Line Segments," *IEEE Trans. Signal Process.*, vol. 49, pp. 381–393, Feb 2001.

[52] H. M. Özaktaş, Z. Zalevsky, and M. A. Kutay, *The Fractional Fourier Transform with Applications in Optics and Signal Processing*. London: John Wiley & Sons, 2000.

[53] J. C. Wood and D. T. Barry, "Radon transformation of time–frequency distributions for analysis of multicomponent signals," *IEEE Trans. Signal Process.*, vol. 42, pp. 3166–3177, Nov. 1994.

[54] L. B. Almedia, "The Fractional Fourier Transform and Time-Frequency Representations," *IEEESP*, vol. 42, pp. 3084–3091, Nov 1994.

[55] J. R. Parker, *Algorithms for Image Processing and Computer Vision*. New York: John Wiley & Sons, 1997.

[56] M. N. Gürcan, *Computer Aided Diagnosis In Radiology.* PhD thesis, Bilkent University, March 1999.

[57] D. J. Williams and M. Shah, "A fast algorithm for active contours," *IEEE Trans. on PAMI*, vol. 4, pp. 592–595, 1990.

[58] A. A. Amini, S. Tehrani, and T. E. Weymouth, "Using Dynamic Programming for Minimizing the Energy of Active Contours in the Presence of Hard Constraints," *Second International Conference on Computer Vision*, pp. 95–99, 1988.

[59] J. G. Proakis and D. G. Manolakis, *Digital Signal Processing Principles, Algorithms, and Applications.* New Jersey: Prentice Hall, 3 ed., 1996.

# APPENDIX A

# Laboratory Schema

All the brain signals analyzed in this study are recorded from the Cognitive Psychophysiology Research Unit of Hacettepe University whose laboratory schema is given in Fig. A.1. A 'Nihon Kohden EEG 4418K' [32] is used in recording the neuroelectric responses of the brain, which are processed by the commercial system, Brain Data 2.92.

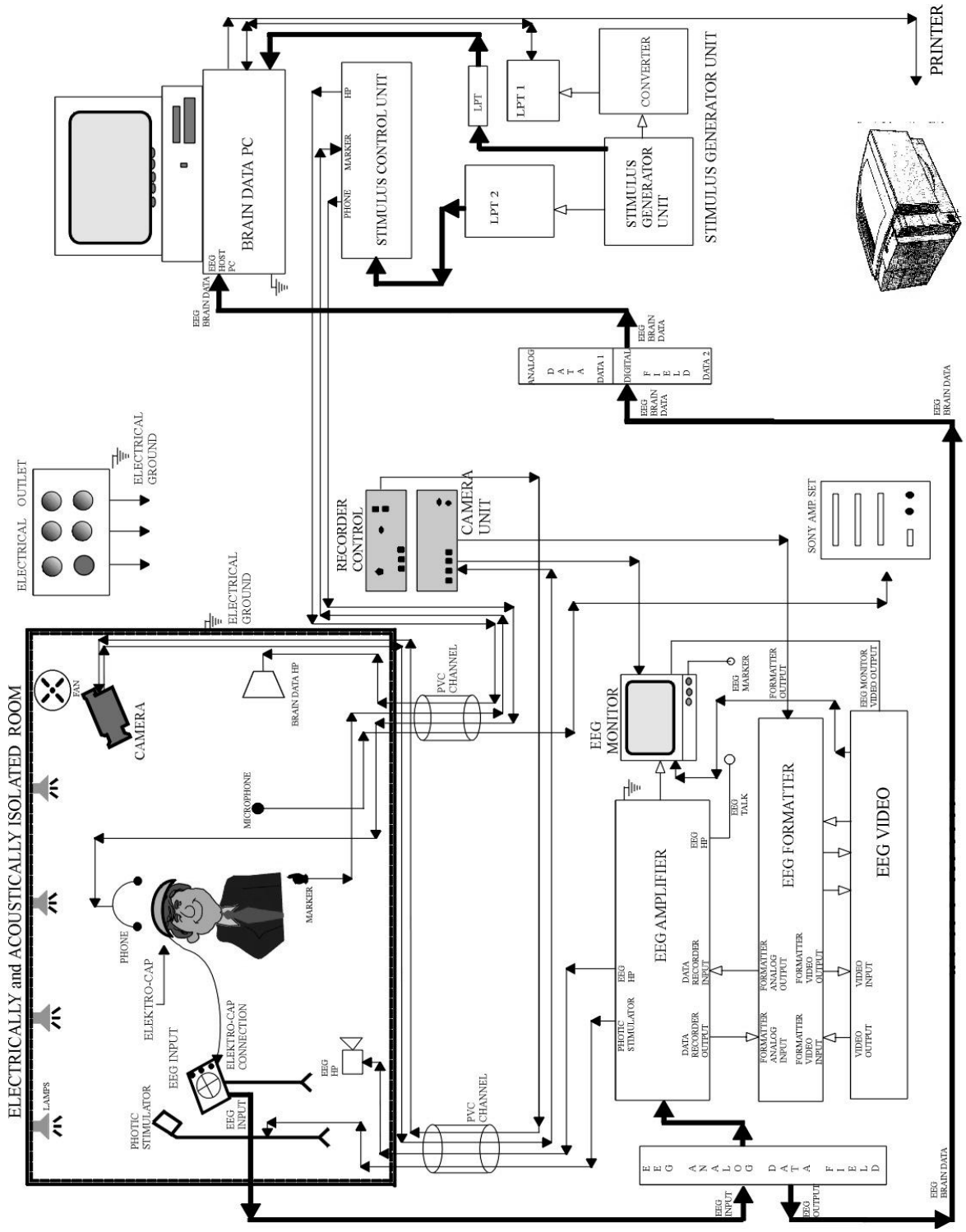


Figure A.1: The Block Diagram of the Cognitive Psychophysiology Research Unit of Hacettepe University.

# APPENDIX B

# Fractional Fourier Transform

Wigner distribution of a signal on a radial slice is the Fourier transform (FT) of the ambiguity function of that signal where the ambiguity function can be related to the $(a-1)^{th}$ order FrFT of the signal. This Appendix first explores the relationship between the Radon transform of the ambiguity function (RAFT) of a signal $x(t)$ and its FrFT. Hence the computation of the WD on a radial slice requires the efficient digital computation of the FrFT whose algorithm [30] is given in Section B.2.

## B.1 Relationship Between RAFT and FrFT

The ambiguity function is the 2-D inverse Fourier Transform of the Wigner distribution:

$$A_x(\nu,\tau) \triangleq \int\int W_x(t,f)e^{j2\pi(\nu t+\tau f)}\,dt\,df \tag{B.1}$$

$$= \int x(t+\tau/2)x^*(t-\tau/2)e^{j2\pi\nu t}\,dt \quad . \tag{B.2}$$

The Radon-ambiguity function transform (RAFT) of a signal $x(t)$ is the Radon transform of its ambiguity function and it can be written as

$$Q_x(r,\phi) = \int A_x(r\cos\phi - s\sin\phi, r\sin\phi + s\cos\phi)\,ds \quad , \tag{B.3}$$

where $(r,\phi)$ are the polar format variables. Substitution of Eq. B.2 into Eq. B.3 gives

$$\begin{aligned} Q_x(r,\phi) &= \int\int x(t+\tau/2)x^*(t-\tau/2)e^{j2\pi\nu t}\Big|_{\nu=r\cos\phi-s\sin\phi,\quad \tau=r\sin\phi+s\cos\phi} dt\,ds \quad , \quad \text{(B.4)} \\ Q_x(r,\phi) &= \int\int x(t+\frac{r\sin\phi+s\cos\phi}{2})x^*(t-\frac{r\sin\phi+s\cos\phi}{2})e^{j2\pi(r\cos\phi-s\sin\phi)t}\,dt\,ds \quad . \end{aligned}$$

Making the following change of variables:

$$\begin{aligned} \begin{bmatrix} t_1 \\ t_2 \end{bmatrix} &= \begin{bmatrix} 1 & +\frac{1}{2}\cos\phi \\ 1 & -\frac{1}{2}\cos\phi \end{bmatrix} \begin{bmatrix} t \\ s \end{bmatrix} + \frac{1}{2}r\sin\phi \begin{bmatrix} 1 \\ -1 \end{bmatrix} \\ dt_1\,dt_2 &= |\cos\phi| dt\,ds \quad , \end{aligned}$$

the equation becomes

$$Q_x(r,\phi) = \int\int x(t_1)x^*(t_2)e^{j\pi[-(t_1^2-t_2^2)\tan\phi+(t_1+t_2)r\sec\phi]}\frac{1}{|\cos\phi|}dt_1\,dt_2 \quad . \tag{B.5}$$

From the definition of $A_\phi$ given in Eq. 4.12,

$$\frac{1}{|\cos\phi|} = |A_{\phi-\pi/2}e^{-j\pi(r/2)^2\tan\phi}|^2 \quad , \tag{B.6}$$

is obtained. By the substitution of Eq. B.6 into Eq. B.5, $Q_x(r,\phi)$ becomes

$$
\begin{aligned}
Q_x(r,\phi) &= \left[\int A_{\phi-\pi/2} e^{j\pi(-(r/2)^2 \tan\phi + rt_1 \sec\phi - t_1^2 \tan\phi)} x(t_1)\ dt_1\right] \\
&\quad \left[\int A_{\phi-\pi/2} e^{-j\pi((r/2)^2 \tan\phi + rt_2 \sec\phi + t_2^2 \tan\phi)} x(t_2)\ dt_2\right]^* \\
&= \left[\{\mathcal{F}^{(a-1)} y\}(r/2)\right] \left[\{\mathcal{F}^{(a-1)} y\}(-r/2)\right]^* \\
&= x_{(a-1)}(r/2)\ x^*_{(a-1)}(-r/2)
\end{aligned}
$$

where $(a-1) = \frac{2\phi}{\pi} - 1$ is the FrFT order.

The previous equation is valid for radial line segments. For the computation of the RAFT on non–radial line segments as shown in Fig. 4.3 and reproduced here for the sake of completeness as Fig. B.1, a new function $y(t) = x(t + t_0)e^{-j2\pi f_0 t}$ is introduced.

As shown in Fig. B.1, the radial slice of $y(t)$ is equivalent to the non–radial slice of $x(t)$. Thus the RAFT of $y(t)$, $Q_y(r,\phi)$, can be written as

$$
Q_y(r,\phi) = y_{(a-1)}(\frac{r}{2})\ y^*_{(a-1)}(-\frac{r}{2}) \quad . \tag{B.7}
$$

To express $Q_y(r,\phi)$ in terms of the original signal $x(t)$, we first relate the FrFT of $y(t)$ to the FrFT of $x(t)$ by using the properties of the FrFT [52, 54]:

$$
y_{(a-1)}(t) = Ce^{j\varphi(t)} x_{(a-1)}(t - t_0 \sin\phi + f_0 \cos\phi) \quad , \tag{B.8}
$$

where unit magnitude complex constant $C$ and linear phase factor $\varphi(t)$ are given as

$$
C = e^{j\pi \cos\phi (f_0^2 \sin\phi + t_0 \cos\phi + f_0 t_0 \sin\phi)} \tag{B.9}
$$

$$
\varphi(t) = 2\pi t(f_0 \sin\phi + t_0 \cos\phi) \quad . \tag{B.10}
$$

$(t_0, f_0)$ can be selected as any point on the $L_w$, to simplify Eq. B.8, $(t_0, f_0) \triangleq (-d\sin\phi, d\cos\phi)$ is chosen to be the closest point on $L_w$ to the origin. In this

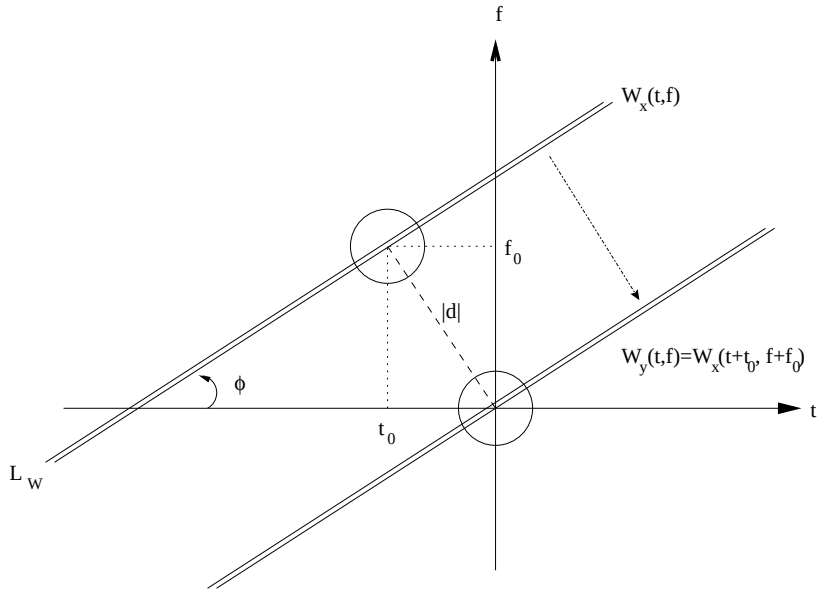


Figure B.1: Illustration of the radial and non–radial slices in the computation of the WD (Same as Fig. 4.3).

case $\varphi(t) = 0$ becomes zero and Eq. B.8 takes the following form

$$y_{(a-1)}(t) = Cx_{(a-1)}(t+d) \quad . \tag{B.11}$$

Finally by substituting this relation into Eq. B.7, we obtain the desired expression for $Q_y(r,\phi)$:

$$Q_y(r,\phi) = x_{(a-1)}(\frac{r}{2}+d)\ x^*_{(a-1)}(-\frac{r}{2}+d) \quad . \tag{B.12}$$

## B.2 Fast Fractional Fourier Transform Algorithm

Given $x(n/\Delta_x)$, $m = -N/2 \leq n \leq N/2$, this algorithm computes $x(m\Delta_x/(2N)+d)$ $, m = -N, -N+1, \ldots, N-1$ [30]. It is assumed that $x(t)$ is scaled before obtaining its samples so that its WD is confined into a

circle with diameter $\Delta_x \leq \sqrt{N}$.

**Steps of the algorithm:**

Interpolate the input samples by 2:

$a^{'} = (a + 2\ mod\ 4) - 2$ % After the modulo operation, $|a^{'}| \in [-2, 2)$

**if** $|a^{'}| \in [0.5, 1.5]$ **then**

$a^{''} = a^{'}$

**else**

$a^{''} = (a^{'} + 1\ mod\ 4) - 2$ % After the modulo operation, $|a^{'}| \in (0.5, 1.5)$

**end if**

$\phi^{''} = \frac{\pi}{2}\ a^{''}$

$\alpha^{''} = cot\ \phi^{''}$

$\beta^{''} = csc\ \phi^{''}$

$A_{\phi^{''}} = \frac{exp(-j\pi sgn(sin\phi^{''})/4 + j\phi^{''}/2)}{|sin\phi^{''}|^{1/2}}$

% Compute the following sequences

$$
\begin{aligned}
c_1[m] &= e^{j\pi[(\frac{\alpha^{''}}{4\Delta_x^2} - \frac{\beta^{''}}{4N})m^2 - \frac{\beta^{''} d}{\Delta_x} m]} && m = -N, -N+1, \ldots, N-1 \\
c_2[m] &= e^{j\pi \frac{\beta^{''}}{4N} m^2} && m = -2N, -2N+1, \ldots, 2N-1 \\
c_3[m] &= e^{j\pi[\alpha^{''}(\frac{\Delta_x}{2N} m + d)^2 - \frac{\beta^{''}}{4N} m^2]} && m = -N, -N+1, \ldots, N-1 \\
g[m] &= c_1[m] x(m/2\Delta_x) && m = -N, -N+1, \ldots, N-1 \\
h_{a^{''}}(m\Delta_x/(2N)) &= \frac{A_{\phi^{''}}}{2\Delta_x} c_3[m](c_2 \star g)[m] && m = -N, -N+1, \ldots, N-1
\end{aligned}
$$

**if** $|a^{'}| \in [0.5, 1.5]$ **then**

$x_a(m\Delta_x/(2N) + d) = h_{a^{''}}(m\Delta_x/(2N))$

**else**

% Compute samples of the ordinary FT using FFT.

$x_a(m\Delta_x/(2N) + d) = \{\mathcal{F}^1 h_{a^{''}}\}(m\Delta_x/(2N) + d)$

**end if**

# APPENDIX C

# Chirp Transform Algorithm

The radial slice of the WD at an angle $\phi$ can be written as the FT of the Radon ambiguity function transform (RAFT) $Q_x(r,\phi)$ with respect to the radial variable r

$$W_x(\lambda,\phi) = \int Q_x(r,\phi) e^{-j2\pi r\lambda}\, dr \quad , \tag{C.1}$$

where RAFT is related to the $(a-1)^{th}$ order FrFT of the signal $x(t)$ as

$$Q_x(r,\phi) = x_{(a-1)}(r/2)\; x^*_{(a-1)}(-r/2) \quad , \tag{C.2}$$

as shown in Appendix B.1. The computation of the radial slice of the WD requires the digital computation of the FT given in Eq. C.1.

Prior to obtaining the samples of the WD, $x(t)$ is scaled so that its WD support is approximately confined into a circle with radius $\Delta_x/2$ centered at the origin. Assuming $x(t)$ has approximate time and bandwidth $\Delta_t$ and $\Delta_f$ respectively, the required scaling is $x(t/s)$ where $s = \sqrt{\Delta_f/\Delta_t}$. After the scaling, double–sided bandwidth of $Q_x(r,\phi)$ becomes $2\Delta_x$. Denoting the $n^{th}$ sample of the RAFT given in Eq. C.2 as $q[n] \triangleq x_{(a-1)}(n/2\Delta_x)\; x^*_{(a-1)}(-n/2\Delta_x)$,

and writing the integral in Eq. C.1 as its uniform Riemann summation, we obtain

$$W_x(\lambda,\phi) = \frac{1}{2\Delta_x}\sum_{n=-N}^{N-1} q[n]e^{-j\frac{\pi\lambda n}{\Delta_x}} \quad , \quad -\Delta_x \leq \lambda < \Delta_x \quad , \tag{C.3}$$

where the ambiguity function is sampled at a rate $1/2\Delta_x$. To obtain the M uniformly spaced samples of $W_x(\lambda,\phi)$ on an arbitrarily positioned segment of a radial slice $[\lambda_i,\lambda_f]$, we substitute $\lambda = \lambda_i + k\Delta_\lambda, k = 0,1,\ldots,M-1$ in Eq. C.3

$$W_x(\lambda_i + k\Delta_\lambda,\phi) = \frac{1}{2\Delta_x}\sum_{n=-N}^{N-1} q[n]e^{-j\frac{\pi n}{\Delta_x}\lambda_i + k\Delta_\lambda} \quad , \tag{C.4}$$

where $\Delta_\lambda = \frac{\lambda_f-\lambda_i}{M-1}$ is the sampling interval of the frequency variable $\lambda$. Rearranging the terms in Eq. C.4 gives

$$W_x(\lambda_i + k\Delta_\lambda,\phi) = \frac{1}{2\Delta_x}\sum_{n=-N}^{N-1} (q[n]e^{-j\pi\frac{\lambda_i}{\Delta_x}n})e^{-j\pi\frac{\Delta_\lambda}{\Delta_x}kn} \quad . \tag{C.5}$$

Defining two new sequences $g[n]$ and $W$ as

$$g[n] = \frac{1}{2\Delta_x}\, q[n]e^{-j\pi\frac{\lambda_i}{\Delta_x}n} \tag{C.6}$$

$$W = e^{-j\pi\frac{\Delta_\lambda}{\Delta_x}} \quad , \tag{C.7}$$

we obtain

$$W_x(\lambda_i + k\Delta_\lambda,\phi) = \sum_{n=-N}^{N-1} g[n]W^{kn} \quad , \quad k = 0,1,\ldots,M-1 \quad . \tag{C.8}$$

Using the identity $kn = \frac{1}{2}[n^2+k^2-(k-n)^2]$ in Eq. C.8, we obtain an alternative expression for $W_x(\lambda_i + k\Delta_\lambda,\phi)$:

$$W_x(\lambda_i+k\Delta_\lambda,\phi) = W^{k^2/2}\sum_{n=-N}^{N-1} W^{-(k-n)^2/2}(g[n]W^{n^2/2}) \quad , \quad k = 0,1,\ldots,M-1 \quad . \tag{C.9}$$

This expression can be computed from the chirp z-Transform algorithm whose details can be found at [59].